DYNAMIC HOLOGRAMS FOR WAVELENGTH DIVISION MULTIPLEXING

A dissertation submitted for the degree of
Doctor of Philosophy
at the University of Cambridge

Michael Charles Parker
Sidney Sussex College

November 1996

Declaration

This dissertation contains the results of research undertaken by the Author between January 1993 and August 1996 at the Department of Engineering, University of Cambridge. Except for the experiment described in §4.3 which is the result of a collaboration between the Author and S.T. Warr, no part of this dissertation is the result of work done in collaboration with others. The contents have not been submitted, in whole or in part, for any other University Degree or Diploma.

M.C. Parker

Michael Charles Parker
Cambridge, November 1996

Summary

This dissertation consists of six sections, summarised below:

Introduction: This chapter provides an overview of the major concepts and technologies in current optical telecommunications research, such as wavelength division multiplexing (WDM), optical time domain multiplexing (OTDM), and erbium-doped fibre amplifiers (EDFAs), the support and development of which has acted as the major motivation behind this Ph.D. The current competing technologies for tunable filters and lasers are reviewed, followed by an introduction to the use of holography in optical telecommunications.

Ferroelectric Liquid Crystal Spatial Light Modulators: An introduction to spatial light modulators (SLMs) is given, followed by an analysis of how the ferroelectric liquid crystal (FLC) material properties, such as the switching angle, affect the diffraction efficiency of a FLC SLM. Original analysis of the phase modulation properties of FLC with respect to circularly polarised light is given, followed by a method to double the allowable phase modulation using a quarter-wave plate and mirror, while maintaining polarisation insensitivity. A characterisation of the FLC SLM used in the experiments within this dissertation is also presented.

Binary-Phase Hologram Analysis: Original theoretical analysis of the performance of large 1-dimensional binary-phase holograms is presented. Expressions are derived for the expected diffraction efficiency ($\sim$36.5%) and minimum signal-to-noise ratios ($>N/2p$) for binary-phase holograms with N pixels, fanning out to p uniform spots of light. These results can be used for system design, since they allow the expected power budget and noise performance of the system to be calculated. The results are equally applicable to binary-phase holograms used in beam-steering and spatial fanning out of monochromatic light.

Tunable Wavelength Filter: Results from a polarisation-insensitive, high resolution and digital holographic filter are presented. The filter was tunable over 82.4nm in steps of 1.3nm, with the filter 3dB passband being 2nm. The filter exhibited an insertion loss of 22.8dB. Simultaneous multiple wavelength filtering is also demonstrated. The design of low loss and high resolution holographic tunable wavelength filters is discussed, and minimum system sizes calculated for a filter resolution of 0.8nm. A filter insertion loss of 6.5dB should also be possible. An analysis of the chirp imparted onto a signal passing through a holographic wavelength filter is given.

Tunable Fibre Laser: Results are presented of a tunable erbium-doped fibre laser, tuned using the holographic wavelength filter. Tuning over 38.5nm in steps of 1.3nm with output powers of up to -13dBm has been achieved. The inherent laser linewidth was measured to be of the order of 3kHz, and the wavelength stability was of the order of 0.1nm. Multiwavelength lasing action has also been demonstrated.

Conclusions: Conclusions are drawn from the results of the experimental holographic wavelength filter described in this dissertation, and the requirements for improved tunable filters discussed. The use of holographic wavelength filtering for *dynamic EDFA gain equalisation* is proposed (with preliminary results presented in Appendix B.) Future work and ideas are presented as to how a compact, low-loss, polarisation-insensitive and high speed ($\sim$nanosecond switching time) wavelength filter and *space-wavelength switch* for WDM might be realised.

Keywords: Ferroelectric liquid crystal (FLC), spatial light modulator (SLM), WDM, computer generated hologram (CGH), digital holographic wavelength filter, phase modulation, tunable laser, EDFA gain equalisation

Acknowledgements

I would foremost like to thank my supervisor Robert Mears who has been the main source of inspiration and motivation behind my Ph.D. His advice, suggestions, help, open-mindedness and light-handed approach to my work, has given me the freedom to explore, experiment and discover, so ensuring that my Ph.D. was the enjoyable, fulfilling and stimulating opportunity for research in a first-class environment, which was everything I had hoped for.

Many thanks to my friends in Cambridge who have made the past four years so enjoyable, exciting, stressful and fun, and who have left me with so many memories, notably Brendan, Kent, Barry, Ian, Freddy and Rachel, Charlanne, as well as Irene, Eileen, Fiona and Geeta at Addenbrookes! Likewise, thanks to the other ex-'Basement Boys' Steve, Tim and Adam for help, useful discussion and argument through the years. I'd also like to thank Dave 'Kozza' Kozlowski for mad humour, advice, borrowing of kit and help in the clean room, and Bill Crossland for his generous support.

A Ph.D. cannot be undertaken without the technical and practical background support of many people, so thanks also go to the workshop: Russell, Mick, Steve and Adrian (the Doom Brothers) for their technical assistance and help, to Caryn for her unfailing cheerfulness and help, and to Anthea Ansell at Sidney Sussex College, who greatly helped me with funding and accommodation when I most needed it.

Finally, and most importantly, I would also like to thank my Parents for the encouragement, support and love they have shown me throughout my time at Cambridge.

to my
family

Contents

List of Figures

List of Figures

Chapter 1

Introduction

$\mathbf{W}$e are presently experiencing the dawn of a new age in our society - the Age of Information. The ability of people to have easy access to huge quantities of information and data has never been greater. The advent of the Information Superhighway mostly in the form of the World Wide Web and the Internet has even occurred during the relatively short period of this Ph.D. Digitalisation, a global fibre-optical network incorporating all optical amplifiers, ever faster and more powerful personal computers have underpinned this transformation in the way we live. A whole host of technologies have been brought together to make this revolution possible. But human nature dictates that the technology must always be improved. The Internet is all ready too slow; people want to receive on-line photographic quality pictures, CD quality sound and real-time high definition video into their PCs, others want to perform intensive distributed computing over the Net and still others are using it for real-time virtual reality applications. If the revolution is not to falter, then ever higher data bandwidths must be made available to individual users. New technologies, concepts and ideas need to be discovered and developed so as to support these demands. This dissertation describes a new technology, holographic wavelength filtering, which may be a contributing factor to the continued advance and success of optical telecommunications.

1.1 Wavelength Division Multiplexing

Telecommunications is currently undergoing yet another revolution. From the middle of the last century, when the digital electrical telegraph could send transatlantic messages at a data rate of about 1b/s (10^0 b/s), to the analogue Mb/s (10^6 b/s) links of a century later, through to the digital optical links, capable of transmitting Tb/s (10^{12} b/s) by the turn of the millennium, telecommunications has developed at an exponential rate. The major telecommunications technological advance in recent years, enabling Tb/s data rates, has been the erbium-doped fibre amplifier (EDFA) [1] for passive broadband optical amplification. This development has opened up the possibility of almost limitless

bandwidth data pipes, and enabled the use of wavelength division multiplexing (WDM) to supply that bandwidth[2], or to allow new optically transparent network architectures such as wavelength-routed networks[3]. The huge impact of this new technology on all levels of optical telecommunications was immediately apparent[4], and has been rapidly developed, so that within 10 years EDFAs are already to be found in significant commercial telecommunications systems, such as the 2.5Gb/s optically amplified submarine transatlantic network TAT-12/13 [5]. A single-mode (SM) optical fibre, due to the material properties of glass, has a number of wavelength 'windows' where low attenuation and dispersion at those wavelengths make them suitable for telecommunications use. The window at the 1.3μm wavelength is currently widely used, since it has zero dispersion and an attenuation of 0.35dB/km. However, another window at a central wavelength of 1.55μm is becoming increasingly popular, since although it has a dispersion of about 12ps $nm^{-1}km^{-1}$ with an attenuation of only 0.2dB/km, it has a useful bandwidth of about 40nm at which the optical gain of the EDFA can compensate the fibre attenuation. This corresponds in the frequency domain to an available bandwidth of about 5THz. No single source can be currently, or is expected to be data-modulated much faster than 100Gb/s [6], so that most of the bandwidth is currently unused. At present there are two competing technologies being developed to enable that available bandwidth to be used most effectively. The first one, as mentioned before, is WDM which uses multiple carrier wavelengths on which to modulate the data in parallel. The second technology is optical time division multiplexing (OTDM) where very short (often less than 1ps) soliton pulses are produced by a source with a relatively 'low' repetition frequency (typically 40GHz). The outputs from multiple soliton sources, each temporally slightly out of phase with respect to the other, can then be interleaved onto a single fibre to give a very high bit rate. The OTDM technology is less well developed than WDM, and the highest data rate using OTDM is currently still only 40Gb/s over 560km of SM fibre[7]. The first WDM Terabit/second data transmissions down a single SM optical fibre have recently been reported[8][9] where 1.1Tb/s (55 wavelengths $\times$ 20Gb/s) was transmitted over 150km of standard single-mode fibre. It can be expected that hybrid WDM/OTDM systems will form the basis of future long-haul high-capacity optical telecommunications networks.

1.2 Technologies for WDM

The main thrust of this Ph.D. has been the development of a new generic technology, which can serve to underpin many of the diverse functional components required in a WDM telecommunications network. These WDM components, all of whose functionality requires a tunable wavelength filter in some form, include tunable sources and receivers, reconfigurable optical amplifiers, space-wavelength switches and routers, as well as wavelength

converters. An ideal tunable wavelength filter would have a rectangular passband of width 0.8nm with greater than 35dB sideband suppression[10], a continuous and large tunable range across the erbium window, multiple wavelength tuning capability, fast tuning speed (measured in nanoseconds), low loss, optical transparency with polarisation insensitivity, low power consumption, compactness and reliability. Many competing technologies have been developed to provide tunable filters fulfilling some, but not all, of these requirements. It is hoped that dynamic holographic filtering will ultimately satisfy these demands. The most significant of the current technologies are outlined below.

1.2.1 Acousto-optic Tunable Filter

The technology which has aroused the greatest interest to date has been the acousto-optic tunable filter. Its distinguishing feature (like that of holographic filtering) is multiple wavelength operation[11]. The first polarisation sensitive wavelength filter using polarisation-mode-coupling to enable tuning was an electro-optic device[12], quickly followed by the acousto-optic equivalent[13]. The acousto-optic version was developed in favour of the electro-optic filter, since only it had the capability of multiple wavelength operation. Polarisation-insensitive wavelength filters soon appeared[14][15][16][17]. Typical filter 3dB passbands of between 1nm to 3nm have been achieved over a couple of hundred nanometres tuning range[18][19]. Insertion losses of the order of 3dB have also been achieved[20]. Acousto-optic filters with near rectangular passbands have also been demonstrated[21][22]. Acousto-optic filters have been used to flatten the gain spectrum of an EDFA [23], while a combined wavelength filter with gain using Er-doped $LiNbO_3$ has also been reported[24]. Actual multiple wavelength operation of an acousto-optic filter has also been demonstrated[25] using 4 wavelengths spaced by 4nm, as has multiwavelength add-drop multiplexing[26], but this is where the limits of the technology begin to become apparent. Acousto-optic filters suffer from high levels of crosstalk[27] and noise from a large variety of inherent sources:

- imperfect polarisation splitting

- interaction between the different RF surface acoustic waves (SAWs)

- frequency shift of signal and time-dependent signal modulation due to RF wave

- high sidelobes outside the passband

The typical inter channel crosstalk is about -15dB, which is increased to -9dB when multiple (*e.g.* four) wavelengths are being filtered[28]. The high sidelobes of the AOTF are due to the $sinc^2$ shape of the passband. A technique using tapered acoustic directional couplers has been developed to reduce the sidelobes, but the suppression is still only at best 15.5dB [20]. Other problems are the minimum 11dBm of power required for each RF SAW to

switch a channel[25], which limits the number of wavelengths which can be simultaneously tuned, before the device overheats. The LiNbO$_3$ substrate, which must be of a high purity, also requires very highly controlled fabrication, so that the birefringence tolerance is of the order of 10^{-5} over its entire length[27]. The passband width is inversely proportional to the device length, and achieving sufficient birefringence control over a length greater than 20mm is difficult, so limiting the resolution to between 1-2nm. Indeed very recent work suggests that AOTFs for use in wavelength routing switches will only work with channel separations 2-4nm [29][30]. This could be reduced down to 1.6nm by space and wavelength dilation[31][32], but at the expense of greater component count and multi-stage switch architectures. Dilated switching architectures have achieved crosstalks of about -30dB [28]. The switching speed of these devices is limited by the velocity of the acoustic wave across the surface of the LiNbO$_3$ substrate to about $10\mu s$ [33].

1.2.2 Fibre Fabry-Perot Etalon

Fibre Fabry-Perot (FFP) etalons are attractive since they offer very high resolution wavelength filtering over relatively large ranges, in a low loss, low power, compact and cheap device. They can only filter one wavelength at a time. Early devices used the piezoelectric effect to mechanically alter the cavity width and achieve tuning[34]. However, piezoelectrically controlled FFPs tend to have a slow switching time, measured in milliseconds. Rather than physically move apart the reflecting faces of the etalon to achieve tuning, the preferred option now is to use birefringent liquid crystal (LC) to electro-optically change the optical cavity width[35][36]. Unfortunately LC in the cavity tends to make the filter polarisation sensitive, although various schemes have been adopted to attain polarisation diversity[37][38]. These polarisation insensitive LC-FFP filters have a 3dB passband of 0.4-0.6nm and a tuning range of 50-70nm, so completely covering the erbium window, and insertion losses of about 3dB. Tuning speeds of LC-FFPs are generally also in the millisecond range, but less than $10\mu s$ has been achieved[39], although at the expense of tuning range and with polarisation sensitivity. A compound wavelength filter consisting of a FFP in series with an AOTF has also been reported with a tuning range of 130nm, and a 3dB passband of only 0.5Å [40].

1.2.3 Semiconductor Filters

Semiconductor wavelength filters can be compactly integrated with a photodiode or used to couple the filtered signal directly into a SM fibre. They have the advantages of small size, low power and compatibility with other optoelectronic devices, but tend to be polarisation sensitive and will only filter one wavelength at a time. A grating assisted vertical coupling filter fabricated out of InGaAsP/InP tunable over 37nm and with a 3dB passband of 5.5nm has been reported[41]. A filter with reduced polarisation sensitivity has also been reported,

with a theoretical tuning range of 110nm and 3dB passband of 1.25nm [42].

1.2.4 Mechanical Systems

High resolution wavelength filtering by means of a diffraction grating and a spatial filter is a standard technique. Tuning is achieved by mechanically rotating the grating, but this tends to be relatively slow and is also more prone to failure. However, high quality filtering is attained (one wavelength at a time), with low crosstalk. A space and wavelength switch has been demonstrated using a rotatable grating with 2 axes of rotation[43]. It has a 3dB passband of 2.5nm, crosstalk of better than -30dB, less than 3dB insertion loss and a tuning time of 4ms. A tunable wavelength ~~wavelength~~ filter employing a rotating interference filter has been demonstrated[44]. It has a bandwidth of 0.5nm, a tuning range of 30nm, switching time of 2.5ms and less than -30dB crosstalk. It has an insertion loss of 2.5dB, but is polarisation sensitive.

1.2.5 Emerging Technologies

Lithium niobate is best known in AOTFs to achieve wavelength switching, but another technique has been developed using it to achieve switching. Switching between the cross and bar branches of a $LiNbO_3$ directional coupler can be made to depend on the input intensity of the incoming light. A switching ratio of 1:5 and throughput of 80% has been reported[45]. Wavelength filtering using passive antiresonant reflecting optical waveguide (ARROW) couplers has been reported with a 3dB bandpass of 4nm [46] and an arrayed waveguide grating has achieved a 3dB passband of 0.3nm [47]. A combination of the two techniques in the future may allow passive self-routing or self-wavelength filtering.

1.3 Tunable Lasers for WDM

Tunable lasers find uses in many areas, apart from telecommunications, such as sensing, spectroscopy and general scientific research. A good tunable laser will have a large tuning range, fine tunability, stable lasing wavelength and perhaps has the flexibility of simultaneous multiple wavelength lasing. Other important attributes of a tunable laser are its output power, linewidth, sidemode suppression, modulation capability, speed of tuning, reliability, size and cost. All of these characteristics when taken together ultimately decide the type of tunable laser best suited to a particular task. As in the case of the tunable wavelength filters, there are many competing tunable laser technologies, all offering an optimum combination of these features. Semiconductor lasers currently form the main technology offering tunable sources for telecommunications, but rare-earth-doped fibre lasers are now also emerging as strong competitors in this important area.

1.3.1 Tunable Fibre Lasers

The main features of fibre lasers are their very narrow linewidths and very closely-spaced longitudinal cavity modes, enabling almost continuous tuning, which is due to their relatively long cavity lengths. High output powers and a broad tuning range are also possible with fibre lasers. This makes them ideal for many applications in WDM systems, such as stable tunable sources, modelocked sources for solitons and local oscillators in coherent detection schemes. Fibre lasers have the additional advantages that they can be pumped with efficient and compact laser diodes, and are compatible with fibre optic components, leading to low coupling losses within telecommunications systems.

1.3.2 External Cavity Tunable Fibre Lasers

There are a many different schemes to make tunable fibre lasers, but they can be basically divided up into external cavity free-space architectures and intra-cavity mechanisms. The intra-cavity fibre lasers have the slight advantage of a greater intrinsic mechanical stability. The first tunable fibre lasers and erbium-doped fibre lasers (EDFLs) employed external rotatable gratings in a Littrow configuration[48][49]. Early EDFLs had a bidirectional architecture, with the light passing up and down the erbium-doped fibre, but this caused standing waves and spatial hole burning with resulting multi longitudinal-moded behaviour. Most EDFLs now adopt a unidirectional ring structure which avoids the problem and ensures only one lasing longitudinal-mode. Continuous tuning ranges of 43nm have been achieved, with very narrow linewidths of less than 7kHz [50][51]. Further developments using an external grating have resulted in tunable polarised lasers[52] and a tunable praesidium-doped fibre laser centred on 1048nm and tunable over 86nm [53]. Tunable EDFLs using a rotating optical bandpass filter have also been demonstrated[54] and used to yield a 47nm tunable modelocked EDFL giving pulses of 20-30ps duration[55]. A mechanical solution for tuning an EDFL is however undesirable since it is likely to be less reliable, so further schemes have been developed which use electro-optic, piezoelectric or acousto-optic properties to effect tuning. Acousto-optic modulators (AOMs) operate in a similar manner to gratings by using radio frequency (RF) acoustic waves to set up a standing wave in $LiNbO_3$ to diffract the light through an angle. They are attractive since they are potentially low loss, electrically controlled, high speed and also offer the possibility of multi-wavelength operation. But they are prone to polarisation sensitivity, high cross-talk and are expensive. The first AOM tuned EDFLs were polarisation dependent, suffered from high cross-talk (causing multimoded behaviour), high loss which caused discontinuous tuning across the erbium gain spectrum and experienced linewidth broadening due to the action of the AOM [56]. Subsequent developments have reduced the losses to achieve 40nm continuous tuning, narrow line widths of less than 10kHz, single moded behaviour but still with polarisation

sensitivity[57]. A polarisation diverse AOM tuned EDFL has been reported[58] employing a linear architecture (causing multiple modes to appear), as has one with tuning speeds of $20\mu s$ [59]. A tunable modelocked EDFL giving 30ps pulses has also been demonstrated using an AOM tunable filter[60]. Other bulk device tuning elements such as piezoelectric polarisation-insensitive Fabry-Perot etalons have been employed within a fibre ring cavity to achieve lasing over a range of 61nm [61] and 44nm [62]. Birefringent liquid-crystal etalons which are polarisation-sensitive have also been used within an EDFL, to provide tuning over a range of 45nm [63], and with lasing over 17nm reported in a neodymium-doped fibre laser[64].

1.3.3 Internal Cavity Tunable Fibre Lasers

Intracavity tuning solutions have also been widely investigated, using distributed Bragg reflector (DBR) gratings holographically written into the fibre core with ultra-violet (UV) light[65] to tune the EDFL to a particular wavelength. Mechanically stressing the fibre grating changes its spatial period and tunes the EDFL to another wavelength. The first DBR fibre laser used neodymium-doped fibre[66], closely followed by a non-tunable DBR EDFL employing a fibre grating to define the lasing wavelength which successfully achieved single moded behaviour[67]. Stretching the fibre grating achieved tuning over the limited range of 0.7nm [68] while compressing the grating has allowed lasing over a range of 32nm [69]. Mismatched sampled fibre gratings have allowed discontinuous tuning over 16.7nm [70]. A modelocked (using a semiconductor active filter) tunable DBR EDFL has also been reported giving 6nm tuning and 38ps pulses[71]. Intracavity fibre gratings can also be designed to select multiple wavelengths such that a dual frequency EDFL lasing at two wavelengths separated by 0.56nm and tunable over 1.3nm has been reported[72]. Single-frequency distributed feedback (DFB) erbium-doped fibres have also been developed for use as very stable reference sources[73][74].

Other techniques include the use of a 2-segment EDFL employing 2 dissimilar and separately pumped EDFAs, while keeping the total pump power constant. The pump power in each EDFA is independently adjusted to change the position of the gain profile maximum and hence the lasing wavelength to tune over 8nm [75]. A tuning range of 4nm has also been achieved by simply varying the pump power to a single-amplifier EDFL [76]. However, this suffers the obvious drawback of non-uniform output powers with changing wavelength.

Another optical-fibre property such as the fibre birefringence has also been exploited to tune an EDFL by up to 33nm [77]. An electro-optic reflection Mach-Zehnder interferometer has been inserted into the cavity of an EDFL and successfully tuned over a range of 39nm [78]. This method has the potential for high speed tuning. A $LiNbO_3$ overlay fibre bandpass filter has been used to tune an EDFL over 25nm [79], but it is multimoded and relies on

index-matching oils of different refractive indices and so cannot be described as an electrical system, although electro-optic index changing is a possibility.

Simultaneous co-lasing of an EDFL has been investigated and several results reported. A six channel co-lasing EDFL with channel spacing 4.8nm using a bulk grating WDM multiplexer has been demonstrated[80]. As already mentioned, a dual frequency DBR EDFL has been developed[72]. Spatial mode beating via the insertion of a section of multimode-fibre into the fibre ring has resulted in multiwavelength operation of an EDFL [81].

1.3.4   Semiconductor Tunable Lasers

The main technology to supply tunable lasers for telecommunications applications is currently semiconductor laser diodes. Semiconductor lasers have the chief advantages over fibre lasers of size, direct modulation capability and tuning speed. They can also be easily integrated into photonic (optoelectronic) integrated circuits, OEICs. Their disadvantages are their relatively large linewidths and lower output powers. The two main tuning mechanisms use thermal and electronic effects. Lasers using thermal tuning typically have a tuning speed measured in microseconds, and tunability of about 0.1nm/°C. This provides a fairly limited continuous tuning range, with 7nm being a typical range[82].

Semiconductor lasers which use electronic tuning offer a much greater tuning range, albeit often discontinuous, and tuning speeds measured in nanoseconds. They operate by injecting charge carriers (electrons) into the semiconductor which changes the refractive index of the material, and hence the optical path length. The simplest type of tunable laser is the uninterrupted-grating distributed Bragg reflector (DBR) which has a tuning range of only about 10nm [83]. More complicated devices such as the sampled grating DBR laser[84] have been tuned over 62nm, in discontinuous steps of ∼10nm intervals[85]. A development of the sampled grating DBR is the superstructure grating (SSG) DBR laser which has a discontinuous tuning range of up to 86nm, in steps of again ∼10nm [86]. Quasi-continuous tuning using a super-structure grating (SSG) DBR laser over 34nm has also been demonstrated[87]. A three-section sampled grating DBR laser has been designed and tuned over a range of 30nm [83]. Even more complicated devices such as the monolithic interferometric Y laser with a continuous tuning range of 51nm has been demonstrated[88], while the forward-reverse coupled laser has the potential of discontinuous tuning over as much as 100nm [89]. With all these semiconductor devices, there is the trade off between complexity and tuning range.

1.4   Holography in Telecommunications

Holography for use in telecommunications to facilitate optical fibre-to-fibre switching and interconnection is still a relatively recent development, but is increasingly attracting at-

tention because of the features it has to offer: optical transparency, low crosstalk[90], polarisation insensitivity[91], efficient use of available light and potential low loss, good wavelength insensitivity, and potential switching speeds of down to $2\mu s$ [92]. Fixed computer generated holograms (CGHs) were initially used for static array generation[93] as well as arbitrarily weighted interconnects[94]. However, dynamic holographic interconnection using a ferroelectric liquid crystal (FLC) spatial light modulator (SLM) to act as a reconfigurable CGH was subsequently suggested[95] and successfully demonstrated by various groups[96][97][98][99]. Up to now, the wavelength-dispersion of CGHs has been viewed as a problem, a form of chromatic aberration, to be minimised[100], but also too small to be usefully exploited. As mentioned above, the wavelength-dispersion is still sufficiently small for the FLC SLMs used in optical switching, for them to be considered effectively wavelength-insensitive. Hence, the use of FLC SLMs for wavelength switching in WDM has generally been considered impractical, due to the large SLM pixel sizes and their relatively few number, as well as the general wavelength insensitivity of the FLC cell. However, the combination of a fixed high-spatial-frequency phase-grating with a FLC SLM has amplified the wavelength dispersion sufficiently to allow the advantages of holographic switching to be used for wavelength switching in WDM. This concept forms the basis of a new generic technology for wavelength filtering, which may find particular application in WDM telecommunications systems. During the course of this Ph.D., a holographic wavelength filter has been developed and used to perform WDM demultiplexing[101][102], to act as the tuning element of a tunable erbium-doped fibre laser[102] and to demonstrate active gain equalisation and channel management of a WDM telecommunications system[103].

1.5 Summary of Thesis Chapters

This dissertation is divided into six chapters which are briefly outlined below:

- **Introduction:** This chapter provides an overview of the major concepts and technologies in current optical telecommunications, such as WDM, OTDM, and EDFAs, the support and development of which has acted as the major motivation behind this Ph.D. The current competing technologies for tunable filters and lasers are reviewed, followed by an introduction to holography for use in optical telecommunications.

- **Ferroelectric Liquid Crystal Spatial Light Modulators:** An introduction to spatial light modulators (SLMs) is given, followed by an analysis of how the ferroelectric liquid crystal (FLC) material properties, such as the switching angle, affect the diffraction efficiency of a FLC SLM. Original analysis of the phase modulation properties of FLC with respect to circularly polarised light is given, followed by a method to double the allowable phase modulation using a quarter-wave plate and mirror. A

characterisation of the FLC SLM used in the experiments within this dissertation is also presented.

- **Binary-Phase Hologram Analysis:** Original theoretical analysis of the performance of binary-phase holograms is presented. Expressions are derived for the expected diffraction efficiency ($\sim 36.5\%$) and signal-to-noise ratios ($> \frac{N}{2p}$) for binary-phase holograms with N pixels, fanning out to p uniform spots of light. These results are important for system design, and are equally applicable to binary-phase holograms used in beam-steering and spatial fanning out of monochromatic light.

- **Tunable Wavelength Filter:** Results from the first proof-of-principle experimental holographic filter are presented, followed by the results from an improved, polarisation-insensitive, higher resolution and relatively low loss holographic filter. The design of holographic tunable wavelength filters is discussed, and minimum system sizes calculated for a given filter resolution of 0.8nm. An analysis of the chirp imparted onto a signal passing through a holographic wavelength filter is given.

- **Tunable Fibre Laser:** Results are presented of a tunable erbium-doped fibre laser, tuned using the holographic wavelength filter. Tuning over 38.5nm in steps of 1.3nm with output powers of up to -13dBm has been achieved.

- **Conclusions:** Conclusions are drawn from the results of the experimental holographic wavelength filter described in this dissertation, and the requirements for improved tunable filters discussed. Future work, ideas and concepts are presented to indicate how further progress is to be made in the use of dynamic holograms for WDM.

Chapter 2

Ferroelectric Liquid Crystal Spatial Light Modulators

2.1 Introduction to Spatial Light Modulators

Spatial light modulators (SLMs) are used to control and dynamically change the properties of light, such as its phase or amplitude, over a 1-dimensional or 2-dimensional area of space. The simplest SLMs are static devices which only change the amplitude of the light, such as a black and white photographic slide, a photograph or a fixed diffractive optical element (which modulates the phase of the incident light.) However, it is often desirable to have a dynamic modulation capability, such as is required for video. Hence, the most common dynamic SLMs can be thought of as the displays in laptop PCs and portable liquid crystal (LC) TVs[1]. Another increasingly important use for dynamic SLMs is in astronomical telescopes, where the SLM acts as an active optical element, correcting the abberations due to optical path differences through the atmosphere. These are the main commercial applications which have driven the rapid development of liquid crystal SLMs.

However, since SLMs can display pictures or patterns of data, they are also ideal devices to display computer generated holograms (CGHs). When they are phase-modulating light, they are acting as efficient programmable diffractive optical elements. In this dissertation, a dynamic phase-modulating SLM has been used to act as a programmable diffraction grating by displaying different holograms. It forms the basis of a tunable wavelength filter, which has been used as a WDM demultiplexer and as the tuning element within the cavity of a tunable fibre ring laser. Thus, in addition to their use as a means to enable dynamic holographic optical interconnects[95], SLMs may also become an important commercial

---

[1]A cathode ray tube TV is not an SLM, since the phosphor screen emitting the image is passive, with the image determined by the intensity of the electron beam as it is rastered. The luminescent light from the phosphor screen is neither intensity nor phase modulated - it is merely emitted according to the level of electronic excitation.
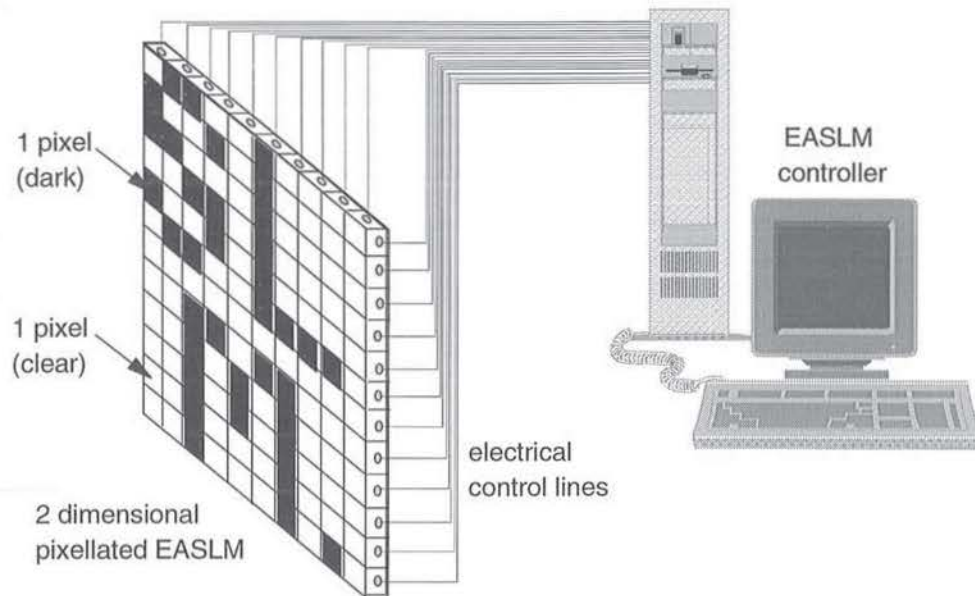
Figure 2.1: Generic electrically addressed spatial light modulator (EASLM)

technology for optical telecommunications because of their potential application in WDM systems.

2.1.1 Spatial Light Modulator Technologies

The dynamic SLM examples given above are all pixellated, with the picture area divided up into many small finite-sized pixels. Each pixel can be individually controlled to create the required spatial image, and hence modulate the light passing through in the desired manner. Materials are thus required, whose optical properties can be electrically, acoustically or magnetically changed, to enable modulation of the light passing through. Pixellated, electrically addressed SLMs (EASLMs) are favoured, since they tend to be the most robust and reliable. Figure (2.1) shows a generic pixellated EASLM displaying an image by amplitude-modulating the light. The large electrooptic properties of modern liquid crystals have made them currently the most developed technology for use in SLMs. There are two main types of liquid crystal for use in SLMs: twisted nematic LC [104] which allows continuous gray-scale modulation of the light, but which is relatively slow, requiring milliseconds in which to change state; and ferroelectric liquid crystal (FLC) [105] which switches state in times measured in microseconds, but normally only allows bistable modulation. Liquid crystal SLMs can be used to either intensity-modulate[106] or phase-modulate[107] the incident light. The LC SLM technology also has the benefits of cheapness and ease of manufacture.

Other technologies exist which can be used to spatially modulate light, although they
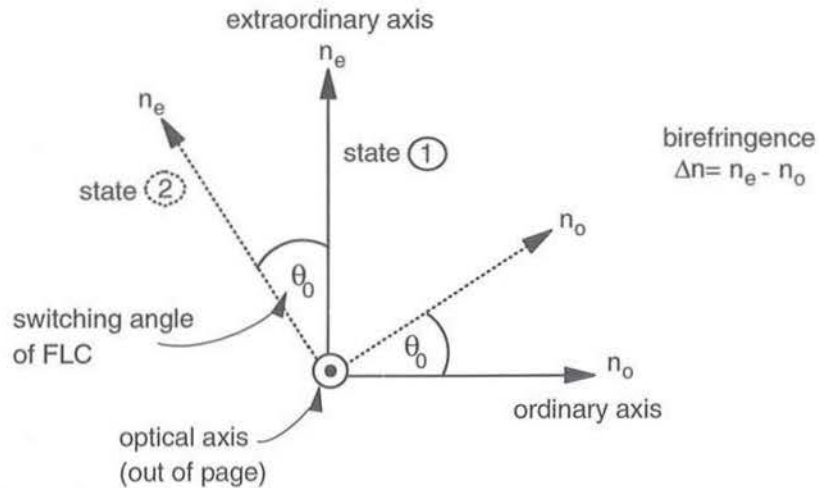
Figure 2.2: Birefringent axes of FLC in 2 states separated by θ_0

tend to be more difficult to manufacture, expensive, polarisation sensitive, low pixel number, but fast. The magneto-optic SLM (MOSLM) [108] uses magnetic and electrical effects to address the pixels. The acousto-optic SLM (AOSLM) [109] uses acousto-optic modulators to create a phase-grating to diffract the incident light. Deformable-mirror SLMs [110] have also been developed, but accurate phase modulation is likely to be difficult. Non-pixellated SLMs also exist, such as the optically addressed SLM (OASLM) [111], which has the advantage of being able to display very high resolution images, and can be used for incoherent-to-coherent light conversion, as well as wavelength conversion. However, it is difficult to implement, since the image needs to be optically written onto the SLM with light at one wavelength, with the light to be modulated at the same or another wavelength. The writing-light, whose intensity distribution determines the image formed on the OASLM, must also have sufficient intensity to cause the optically-active material to change, so that light at the read-wavelength is modulated.

2.2 Experimental FLC SLM Characterisation

Ferroelectric liquid crystals have become an important electrooptic material in recent years, due to their interesting optical properties: high birefringence, large switching angle, fast switching speed and bistability. The switching angle is the angle through which the optical-axis of the FLC turns, as a suitable voltage is applied to switch the optical-axis between its two bistable states. The geometry of this is illustrated in figure (2.2), with the birefringent axes in the plane of the incident light wavefront. The switching angle is equal to twice the cone angle, a material property of the FLC. The time taken for the FLC to rotate its

optical axis determines the switching speed. In fact, FLCs can be either bistable optical materials (such as smectic C* FLCs) with the optical axis existing in only two possible states angularly separated by θ_0, or they can have the optical axis continuously rotating through any angle, within a particular range set by the material, such as smectic A* FLCs. Birefringences of up to $\Delta n = 0.2$ are possible, and switching angles approaching 90° [92], with relatively fast response times $\sim 2\mu s$ [92] have also been measured. Their low cost, ease of manufacture, integration onto silicon VLSI and polarisation-insensitive operation[91] have made FLC SLMs increasingly attractive.

The electrically addressed FLC SLM[2], used in all the experiments described in §4 and §5, was one specially optimised for use in the near infrared wavelengths of about $\lambda_o = 1.55\mu m$, and used a bistable smectic C* FLC[3]. For phase modulation to occur, each pixel (*i.e.* an FLC cell) within the SLM is designed to act as a rotatable half-wave plate. This requires the cell thickness t to be given by $t = \lambda_o/2\Delta n$, where $\Delta n \approx 0.155$ is the FLC birefringence at infrared wavelengths and λ_o is the wavelength of operation. The required cell thickness is therefore $t = 5\mu m$, although in practice the device had a thickness closer to $4.5\mu m$. This is still larger than is generally optimum for a FLC cell, making it difficult to align the liquid crystal correctly with respect to the cell walls, and also making the FLC switching time slower. The FLC switching angle was calculated by measuring the change in transmission through a pair of crossed polarisers with the SLM placed between, when the FLC cells were all switched from one bistable state to the other. The switching angle was found to be $\theta_0 = 2\theta = 28°$, where θ is the FLC cone angle. The SLM was a 2-dimensional pixellated device with 128×128 pixels, each on a $165\mu m$ pitch, with $5\mu m$ dead space. A 1-dimensional pixellated SLM would have been sufficient for the experiments described in this dissertation, with the added advantages of being simpler to manufacture and probably having a faster write-time.

The SLM was controlled by a PC via the printer port. Unfortunately due either to bad handshaking at the PC/SLM interface, or electro-magnetic (EM) interference, the SLM rarely displayed the desired hologram exactly. A random selection of between 5 and 15 pixels did not switch correctly. This is illustrated in figure (2.3) where a desired hologram, and the actual displayed SLM hologram[4] are shown. The SLM was placed between crossed visible-wavelength polarisers, so as to give a viewable amplitude-modulated display. The 12 incorrectly switched pixels are readily seen. Although their presence is expected to slightly impair the hologram performance, the quality of the experimental results gained testifies to the robustness of the holographic wavelength-filtering technique, even when there are pixel failures.

---

[2]EASLM 2DX128 manufactured by CRL, Thorn EMI.

[3]An approximate equal mixture of 744/744r, manufactured by BDH/Merck.

[4]This hologram was the one used to produce the passband transmission curve #5 of figure (4.14).

Desired Hologram:

128 Pixels
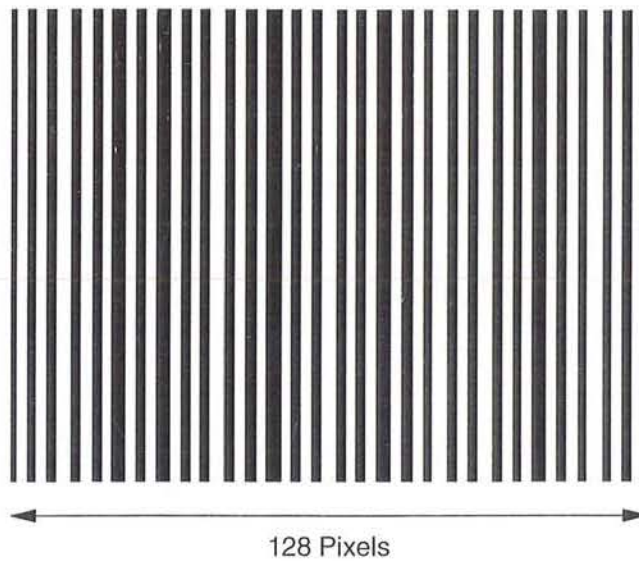
Hologram Displayed on SLM:
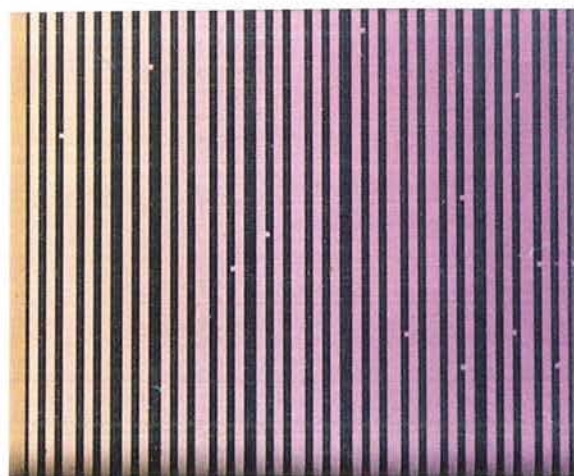
Figure 2.3: Desired hologram and actual hologram displayed on SLM
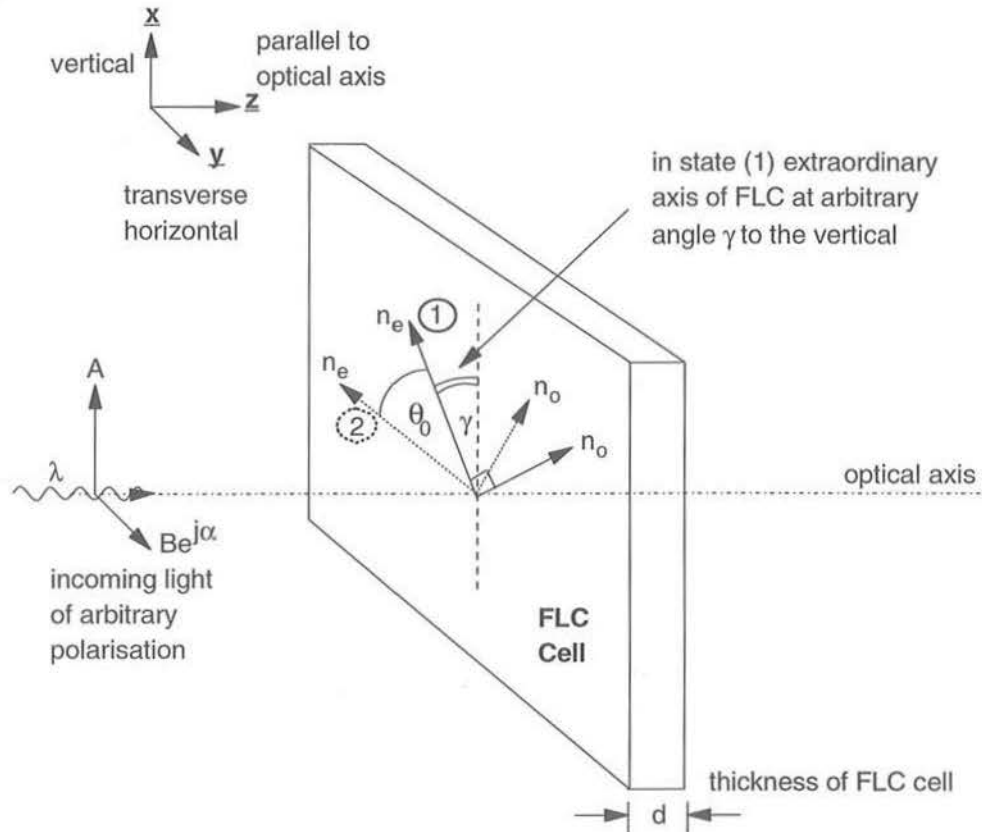
Figure 2.4: Unpolarised light incident on a FLC cell at arbitrary orientation

2.3 Properties of FLC SLMs

2.3.1 Phase Modulation

The pure phase modulation of circularly polarised light by FLC has been recognised for some years[112]. Ferroelectric liquid crystals (FLC) are birefringent materials with the useful property that the optical axis can be rotated through an angle by applying a suitable electric field. By choosing a suitable thickness of FLC and selectively using polarisers, the FLC can be used to modulate either the phase or the amplitude of light passing through along its optical axis. In this analysis we are only interested in the phase modulation capabilities of FLCs which do not require polarisers. Figure (2.2) shows an FLC in one state with its birefringent axes horizontal and vertical, and then with the optical axis rotated through an angle θ_0 into another state (2). The birefringence of the material is expressed as the difference between the refractive indices along the extraordinary axis n_e and ordinary axis n_o. The optical axis comes out of the plane of the page. Jones matrices may be used to analyse what happens to light of wavelength λ and arbitrary polarisation which passes

through the FLC along its optical axis. Figure (2.4) shows light of a random polarisation incident on a FLC cell of thickness d and arbitrarily orientated so that the extraordinary axis is at an angle γ to the vertical in its 'relaxed' state (1). The unit coordinate vectors are: $\hat{x}$ = vertical, $\hat{y}$ = transverse horizontal and $\hat{z}$ = longitudinal horizontal, and the Jones matrices are defined relative to the $\hat{x}$ and $\hat{y}$ coordinate axes. The input state of polarisation $\underline{P}_{in}$ of the light is given by:

$$\underline{P}_{in} = \begin{pmatrix} A \\ Be^{j\alpha} \end{pmatrix} \tag{2.1}$$

where A is the amplitude of the light resolved along the $\hat{x}$ direction, B is the amplitude resolved along the $\hat{y}$ direction and α is the phase difference between the two amplitudes. The state of polarisation $\underline{P}_{out}$ of the light exiting from the FLC cell is given by:

$$\underline{P}_{out} = \underline{J}\,\underline{P}_{in} \tag{2.2}$$

The 2×2 Jones matrix $\underline{J}$ for the FLC cell of thickness d is given by:

$$\underline{J} = \begin{pmatrix} \sin^2(\gamma + \theta_0)e^{jdn_o\frac{2\pi}{\lambda}} & \cos(\gamma + \theta_0)\sin(\gamma + \theta_0)e^{jdn_o\frac{2\pi}{\lambda}} \\ +\cos^2(\gamma + \theta_0)e^{jdn_e\frac{2\pi}{\lambda}} & -\cos(\gamma + \theta_0)\sin(\gamma + \theta_0)e^{jdn_e\frac{2\pi}{\lambda}} \\ \\ \cos(\gamma + \theta_0)\sin(\gamma + \theta_0)e^{jdn_o\frac{2\pi}{\lambda}} & \sin^2(\gamma + \theta_0)e^{jdn_e\frac{2\pi}{\lambda}} \\ -\cos(\gamma + \theta_0)\sin(\gamma + \theta_0)e^{jdn_e\frac{2\pi}{\lambda}} & +\cos^2(\gamma + \theta_0)e^{jdn_o\frac{2\pi}{\lambda}} \end{pmatrix}$$

The FLC cell is normally in a half-wave plate configuration so that the retardances along the two birefringent axes are out of phase by $180°$. This means that $e^{jd(n_e - n_o)\frac{2\pi}{\lambda}} = -1$, requiring the thickness of the FLC material to be $d = \frac{\lambda}{2\Delta n}$, where the birefringence $\Delta n = n_e - n_o$. If we assume this to be the case, then the Jones matrix $\underline{J}$ for the FLC cell can be greatly simplified to yield:

$$\underline{J} = e^{jdn_o\frac{2\pi}{\lambda}} \begin{pmatrix} -\cos(2\gamma + 2\theta_0) & \sin(2\gamma + 2\theta_0) \\ \sin(2\gamma + 2\theta_0) & \cos(2\gamma + 2\theta_0) \end{pmatrix} \tag{2.3}$$

The angle θ_0 is equal to zero when the FLC cell is in its state (1).

It is not obvious in what manner the FLC is modulating the input light, since Jones matrices essentially describe the polarisation of the light in terms of plane polarisations, by resolving the polarisation of the light into cartesian coordinate axes. If on the other hand we describe the light in terms of circular polarisation, it immediately becomes apparent what the FLC is doing to the light. Circularly polarised light can be expressed as the sum of two orthogonal linear polarisations of equal amplitudes but separated in phase by $90°$. If our input polarisation $\underline{P}_{in}$ were clockwise circularly polarised, then with reference to equation (2.1), $A = B$ and $\alpha = -\pi/2$. The other orthogonal circular polarisation is anticlockwise, in which case $\alpha = +\pi/2$. The two unit circular polarisations $\hat{c}_+$ and $\hat{c}_-$ can be described as:

$$\hat{c}_+ = \frac{1}{\sqrt{2}} \begin{pmatrix} 1 \\ -j \end{pmatrix} \quad , \quad \hat{c}_- = \frac{1}{\sqrt{2}} \begin{pmatrix} 1 \\ j \end{pmatrix}$$

The clockwise and anticlockwise circular polarisations are orthogonal to each other, so all possible polarisation states can be described as a weighted summation of them, with a phase difference β, such that:

$$\underline{P}_{in} = \begin{pmatrix} A \\ Be^{j\alpha} \end{pmatrix} \equiv C\hat{\underline{c}}_+ + e^{j\beta}D\hat{\underline{c}}_-$$

If clockwise circularly polarised light is incident on the FLC cell such that:

$$\underline{P}_{in} = \frac{C}{\sqrt{2}} \begin{pmatrix} 1 \\ -j \end{pmatrix}$$

then using equations (2.2) and (2.3) the output state is given by:

$$\underline{P}_{out} = e^{jdn_o \frac{2\pi}{\lambda}} \begin{pmatrix} -\cos(2\gamma + 2\theta_0) & \sin(2\gamma + 2\theta_0) \\ \sin(2\gamma + 2\theta_0) & \cos(2\gamma + 2\theta_0) \end{pmatrix} \frac{C}{\sqrt{2}} \begin{pmatrix} 1 \\ -j \end{pmatrix}$$

$$= e^{jdn_o \frac{2\pi}{\lambda} + \pi + 2\gamma + 2\theta_0} \frac{C}{\sqrt{2}} \begin{pmatrix} 1 \\ j \end{pmatrix}$$

It can be seen that the light coming out is now anticlockwise circularly polarised, and has also been phase modulated. Varying the switching angle θ_0 of the FLC causes a phase modulation of $+2\theta_0$. The additional phase modulation of $\pi + 2\gamma$ is a constant and does not change as θ_0 is varied. Similarly, if the input polarisation were anticlockwise circularly polarised then the output polarisation state would be:

$$\underline{P}_{out} = e^{jdn_o \frac{2\pi}{\lambda} - \pi - 2\gamma - 2\theta_0} \frac{C}{\sqrt{2}} \begin{pmatrix} 1 \\ -j \end{pmatrix}$$

such that the handedness of polarisation has again been reversed, but now the phase change is $-2\theta_0$. The two circular polarisations are in fact *phase-conjugate* modulated. For a phase hologram using FLC, one circular polarisation 'sees' the hologram as expected, while the other orthogonal circular polarisation sees the phase-conjugate of the hologram. This may have useful applications[5]. On the other hand, if we want uniform phase modulation of a plane wavefront, the light needs to be circularly polarised - the handedness does not matter. The orientation of the FLC cell (expressed by the variable γ) is also unimportant, since the additional phase modulation due to γ is a constant for each of the two circular polarisations, while the useful phase modulation due to the switching angle θ_0 is independent of it. There is a crucial difference between a phase hologram based on FLCs and a simple phase hologram made by changing optical path lengths to cause phase changes. A simple phase hologram will give the same phase modulation to both circular polarisations, whereas a FLC hologram will give the phase modulation to one of the circular polarisations, but the conjugate-phase modulation to the other circular polarisation.

---

[5] *e.g.* image and signal processing often requires conjugate filters.
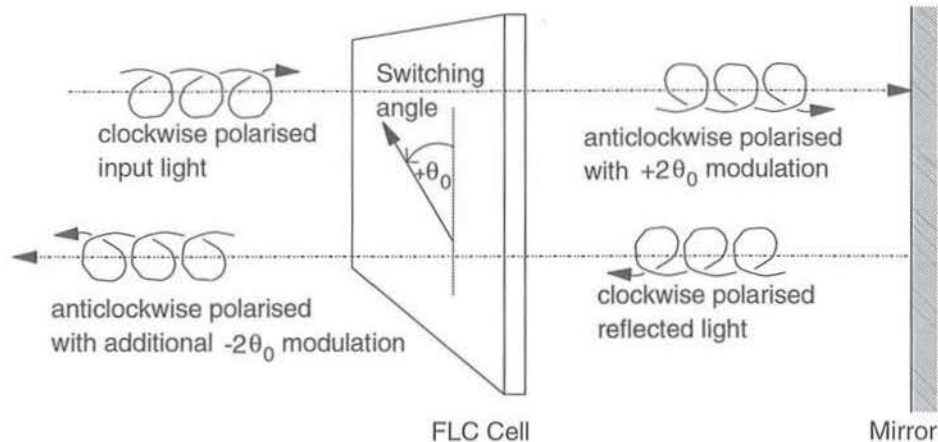
Figure 2.5: FLC cell and mirror together give no phase modulation

2.3.2   Doubling The FLC Phase Modulation

A deep FLC phase modulation capability is desirable since the diffraction efficiency of binary-phase FLC holograms is increased, and a greater range of phase modulation is made possible for continuous phase holograms. The optimum for binary-phase holograms using bistable FLCs is a phase modulation of $0°$ or $180°$, while for continuous phase holograms, we want the phase modulation to range from $0°$ to $360°$. Unfortunately, most FLCs have a limited switching angle which compromises the ability to display optimum holograms on the spatial light modulator. One obvious solution to increase the total phase modulation capability is to cascade FLC SLMs, but this is expensive in terms of hardware and increases the complexity and alignment of the elements in the architecture. A fold-back architecture which reflects the light back through the FLC SLM may appear to be a simple and effective method of increasing the phase modulation depth. However, an architecture like that on its own does not work, because the 2 phase modulations experienced by the light during its 2 passes through the FLC cancel each other out. This is best explained with reference to figure (2.5), where circularly polarised light is passed through a FLC cell. If clockwise circularly polarised light is passed through the FLC it experiences a phase modulation of $+2\theta_0$ and a reversal of polarisation. It is then reflected back by the mirror which also turns the state of polarisation of the light back again to its original clockwise state. The light approaches the FLC again, but now from the opposite side, which means that the switching angle has now 'swapped' to the other side of the vertical axis and in effect has become $-\theta_0$. This causes the additional phase change experienced by the light to be $-2\theta_0$, so that the total phase modulation is now zero. The converse is also true for input light with anticlockwise polarisation. To get useful phase modulation, the polarisation of the
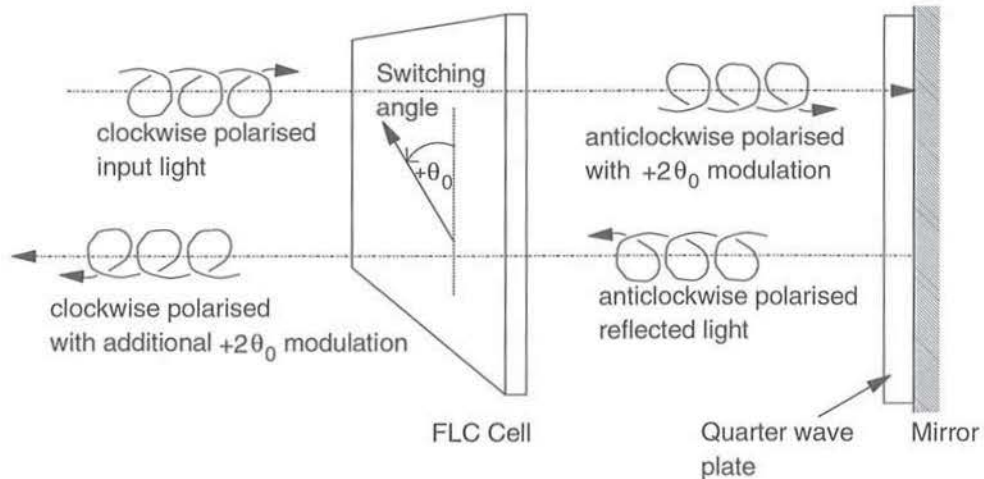
Figure 2.6: FLC cell, quarter-wave plate and mirror doubles phase modulation

light needs to be anticlockwise as it passes back through the FLC cell. The phase change during the second pass would then be $+2\theta_0$, giving rise to a total phase modulation of $+4\theta_0$. The handedness of circularly polarised light can easily be reversed by passing it through a half-wave plate. This can also be achieved by introducing a quarter-wave plate between the FLC cell and mirror, so that the light passes through the quarter-wave plate twice, which effectively then acts as a half-wave plate, so reversing the state of polarisation. This is illustrated in figure (2.6). A polarisation-sensitive architecture using this configuration of FLC, quarter-wave plate and mirror has already been proposed and experimentally verified[113]. Due to its polarisation sensitivity, it was thought that the quarter-wave plate had to be accurately aligned within the system. But for the same reasons as given previously for the orientation insensitivity of the FLC cell (which is a half-wave plate), it follows that the configuration of FLC cell, quarter-wave plate and mirror (as shown in figure 2.6) is also orientation insensitive, such that the relative orientation of the quarter-wave plate is arbitrary. In addition, the two orthogonal circular polarisations of light are still phase-conjugate modulated, which makes this configuration to double the phase modulation of a bistable FLC SLM also polarisation-insensitive, using the argument as given in §2.3.4. Hence the above architecture which doubles the phase modulation of a FLC SLM is made much more attractive, practical and efficient, since it is both polarisation and orientation insensitive. This new polarisation-insensitive architecture was independently conceived by the Author during the course of his Ph.D., but not experimentally tested. However, this configuration to double the phase modulation was experimentally verified using circularly polarised light by another independent group in Boulder, Colorado[114], although they did not recognise
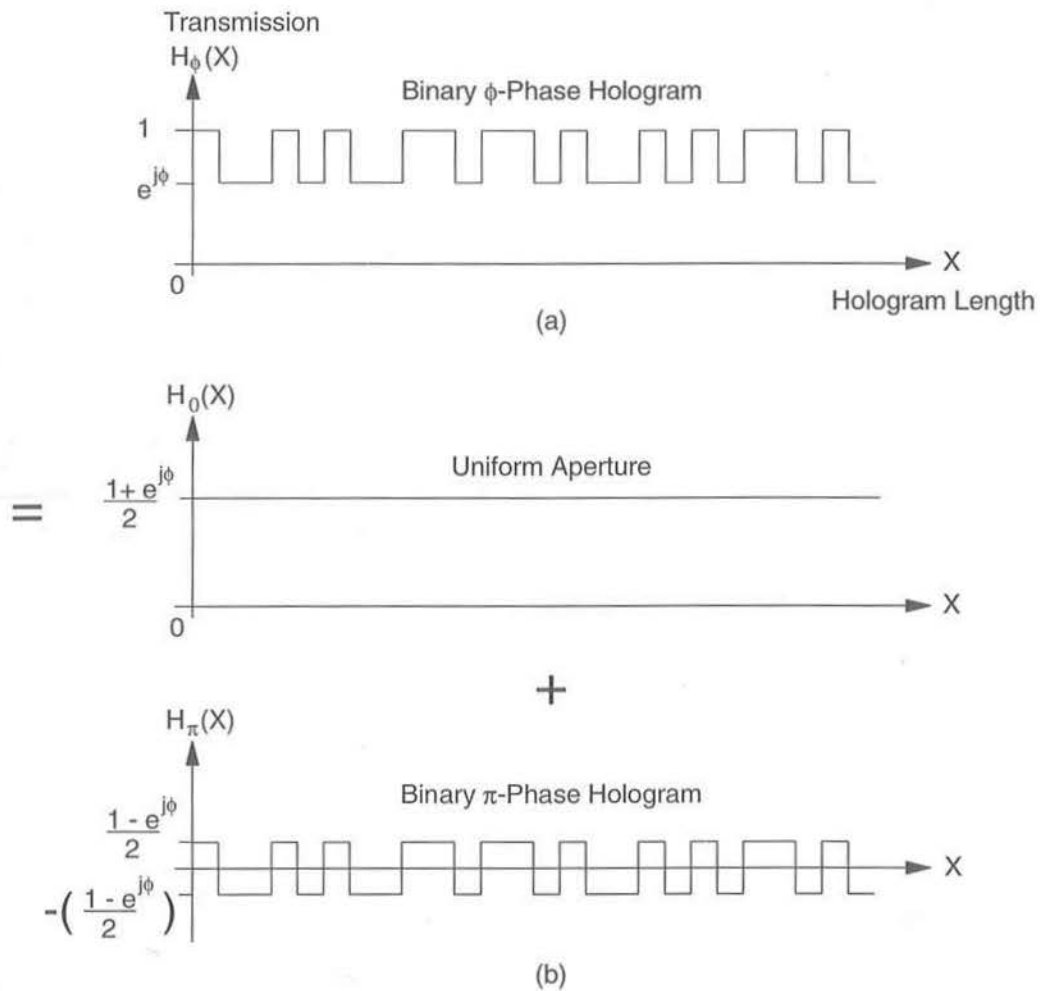
Figure 2.7: Arbitrary binary-phase hologram $H_\phi(X)$ with ϕ phase modulation

its polarisation-insensitive properties when used in a FLC SLM. They also suggest using a polymer cholesteric liquid crystal (PCLC) mirror in place of the quarter-wave plate/mirror combination, to act as a polarisation-preserving mirror, but this makes the architecture polarisation-sensitive. A similar concept using nematic liquid crystal, which has slightly different properties to FLC, has also been published[115].

2.3.3 Diffraction Efficiency

Ferroelectric liquid crystals can be used in a pixellated matrix array or SLM to yield a dynamic hologram, where each SLM pixel can be individually controlled to give a different phase modulation of the light. Since most FLC switching angles have a limited dynamic range, the degree to which light can be phase modulated is compromised. This causes the dynamic hologram to become less efficient at generating the desired diffraction pattern and

a proportion of the light remains undiffracted. For the most part, we want the undiffracted proportion of light to be as low as possible. For a binary-phase hologram, which uses bistable FLC to give 2 possible phase modulations, there is a simple relationship between the diffraction efficiency and the FLC switching angle. An arbitrary binary-phase hologram $H_\phi(X)$ is shown in figure (2.7a). We assume that there is a relative phase modulation ϕ between the two bistable states. We can consider the hologram $H_\phi(X)$ to be the sum of a non-varying uniform aperture $H_0(X)$ (as if the phase modulation depth $\phi = 0$) and a spatially varying hologram which contains the main phase profile information of $H_\phi(X)$. The transmission of the uniform aperture is the average of the 2 bistable states, $(1+e^{j\phi})/2$. The varying hologram can be considered as the desired binary π-phase hologram $H_\pi(X)$ (the optimum hologram when the phase modulation depth is $\phi = 180°$ or π), but with its transmission reduced by a factor $(1 - e^{j\phi})/2$. This is shown in figure (2.7b). Thus we can write:

$$H_\phi(X) = \frac{1 + e^{j\phi}}{2} H_0(X) + \frac{1 - e^{j\phi}}{2} H_\pi(X) \tag{2.4}$$

The resulting diffraction pattern $h_\phi(x)$ due to the hologram $H_\phi(X)$ can then be similarly written as:

$$\begin{aligned}
h_\phi(x) &= \frac{1 + e^{j\phi}}{2} h_0(x) + \frac{1 - e^{j\phi}}{2} h_\pi(x) \\
h_\phi(x) &= \left\{ \cos\frac{\phi}{2} h_0(x) - j \sin\frac{\phi}{2} h_\pi(x) \right\} e^{j\phi/2}
\end{aligned} \tag{2.5}$$

This tells us that any arbitrary diffraction pattern $h_\phi(x)$ is made up of the redundant undiffracted pattern $h_0(x)$ due to the uniform aperture, and the desired π-phase modulation diffraction pattern $h_\pi(x)$. Equation (2.5) is the amplitude distribution of the diffraction pattern, from which we can deduce by multiplying by the complex conjugate:

- $\cos^2\frac{\phi}{2}$ of power is undiffracted

- $\sin^2\frac{\phi}{2}$ of power is usefully diffracted

For a binary-phase hologram using a bistable FLC, the phase modulation between pixels is $\phi = 2\theta_0$ where θ_0 is the switching angle of the liquid crystal. This means that we can only diffract the proportion $\sin^2\theta_0$ of the light and this is maximised when the switching angle $\theta_0 = 90°$. The proportion of diffracted light $\sin^2\theta_0$ is equivalent to the transmission of a FLC cell placed between crossed polarisers, in order to attain π binary-phase modulation[97].

2.3.4   Polarisation Insensitivity of Binary-Phase FLC Holograms

Ferroelectric liquid crystal holograms are in general polarisation-sensitive, since the two orthogonal circular polarisations are phase-conjugate modulated. It is easy to show, however, that binary-phase FLC holograms are in fact polarisation-*insensitive*, because they produce mirrored, symmetric diffraction patterns. This can be done using fourier transform theory.

If we have a binary-phase hologram $H(X)$, then its fourier transform (equivalent to the diffracted output field) can be defined as $h(x)$, where:

$$H(X) \rightleftharpoons h(x)$$

One circular polarisation of light will experience the hologram $H(X)$, but the orthogonal circular polarisation will 'see' the phase-conjugate hologram $H^*(X)$. However, fourier transform theory gives us the identity:

$$H^*(X) \rightleftharpoons h^*(-x)$$

Thus the orthogonal polarised light will be diffracted to give an output field of $h^*(-x)$. But, as already noted above, binary-phase holograms automatically produce a symmetrical output field $h(x)$, such that:

$$h^*(-x) = h(x)$$

This being the case, the two output fields due to the two orthogonal circular polarisations are thus totally identical, which therefore makes the binary-phase FLC hologram polarisation-insensitive, as has been already reported[91]. The two output fields due to the two polarisations will thus have exactly the same amplitude and phase distributions. However, since they are orthogonal to each other, they will form their own identical intensity diffraction patterns, but *not* interfere with each other. This is an interesting property, which may find useful application.

2.3.5 Polarisation-Insensitive Multi-Phase FLC Holograms

In general, multi-phase FLC holograms are polarisation-sensitive, since the two orthogonal circular polarisations are phase-conjugate modulated, so that their diffraction patterns are mirror images of each other. In the case of binary-phase holograms, this effect is obscured by the intrinsic symmetry of the output field, so that the holograms appear polarisation-insensitive. However, this principle can also be extended to any multi-level phase hologram which produces a symmetrical output field: *a multi-level hologram designed to produce a symmetrical output field, will appear to be (and in effect is!) polarisation-insensitive.* All we require is that the output field obeys:

$$|h(-x)| = |h(x)|$$

such that the phase distribution of $h(x)$ does not matter. The output fields due to the two circular polarisations may have totally different phase distributions, but they will still form the same intensity diffraction patterns, while also not interfering with each other. Although most holograms are not designed to produce symmetrical output diffraction patterns, many holograms are specifically designed to have that property. The most common example of this is a Fresnel lens. Thus multi-level phase FLC SLMs can be used within optical systems to provide polarisation-insensitive programmable Fresnel lenses.

Chapter 3

Binary-Phase Hologram Analysis

3.1 Introduction

In this chapter we present a new analysis of the diffraction efficiency and signal-to-noise ratio (SNR) of binary-phase holograms, which is particularly suited to scaling considerations of dynamic monochromatic holographic beam-steering and also wavelength filtering devices. The limited number of pixels in a FLC SLM restricts the performance of the holograms, so increasing the importance of knowing the SNRs and diffraction efficiencies that we can expect in a real holographic system. The analysis which gives theoretical predictions of hologram performance is only of practical use when used in conjunction with an analysis of additional losses and sources of crosstalk to be found in a real holographic system[90]. The analysis is equally applicable to systems employing optical replication of the dynamic hologram to improve performance, which is equivalent to increasing the pixel number. Good agreement between the results of the analysis and the performance of dynamic holograms designed by a number of algorithms (predominantly simulated annealing) has been achieved. The results throw some interesting light on the stochastic holographic design process and should be of interest to those designing dynamic binary holograms for a variety of applications.

3.2 Definitions and Assumptions

In the analysis which follows, the diffraction efficiency is defined to be the proportion of the total optical power passing through the hologram which is successfully directed to the desired fan-out intensity spots in the positive first (+1) order. Since binary-phase holograms always produce a symmetric output field, it follows that half the power is automatically lost, and the diffraction efficiency must be less than 50%. Consider an example holographic image consisting of a single spot of light in the positive first order. The intensity profile $|h(x)|^2$ of the image is shown in figure (3.1). The diffraction efficiency η is defined as:

Figure 3.1: Intensity profile of arbitrary holographic image

$$\eta \;=\; \frac{\int\limits_{x_p-\frac{\Delta x}{2}}^{x_p+\frac{\Delta x}{2}} |h(x)|^2 dx}{\int\limits_{-\infty}^{\infty} |h(x)|^2 dx}$$

The SNR characteristic is defined to be the ratio of maximum intensity of the spots $I_p = |h(x_p)|^2$ with the average intensity of the light between the spots, which is undesired and acts as noise. Using the same image $|h(x)|^2$ above, the average noise intensity I_n is given by:

$$I_n \;=\; \frac{\int\limits_{0}^{x_p-\frac{\Delta x}{2}} |h(x)|^2 dx + \int\limits_{x_p+\frac{\Delta x}{2}}^{X_{+1}} |h(x)|^2 dx}{X_{+1} - \Delta x}$$

The SNR is then given by:

$$SNR \;=\; \frac{I_p}{I_n}$$

In a real system, the illumination of the hologram is likely to be gaussian. It is assumed that the effect of this gaussian illumination in the output plane (mathematically speaking, a convolution) has very little effect on the diffraction efficiency, merely broadening the spots slightly and causing a 'blurring' of the total image.

The underlying assumptions to the following analysis are:

- the holographic image contains p spots of uniform intensity light in the positive first (+1) order

- the number of pixels N in the hologram is much greater than p and can be considered high

25

- the number of pixels N in the hologram is an even number

- the hologram is uniformly illuminated

3.3 Analysis of 1-D Binary-Phase Holograms

The analysis can be split up into a number of consecutive steps. We first take pairs of pixels, symmetrically either side of the centre of the hologram, with each pair fourier-transforming to produce a unit cosine (if the pair has even symmetry) or a unit sine (if it is odd) in the output field. If we assume that the hologram as a whole has even symmetry, then the output field is given solely by the summation of unit cosines of ever increasing spatial frequency. (The generalisation for a non-symmetrical hologram is given in Appendix A.3.) The second step is to assume that the hologram is steering the light to just one arbitrary position in the output plane. We then determine how well we can expect the unit cosines, which are forming the output field, to add up constructively at that arbitrary position so as to give us the maximum possible amplitude of the light at that single point. We can then calculate the average or expected value of a single unit cosine at that point in the output field. The third step is to investigate how the expected value of a single unit cosine at a fan-out position reduces as the hologram has to fan-out to multiple positions in the output field. Finally, we use the expected value of the unit cosine to calculate the expected amplitudes of the fan-out peaks, and hence the diffraction efficiency and SNR.

3.3.1 Definition of Hologram and Output Field

Consider a 1-D hologram consisting of N pixels of dimension W with no dead space between the pixels. An example hologram consisting of 12 pixels is shown in figure (3.2). Light of total power P_{in} is uniformly incident upon the hologram so that each pixel is illuminated with a one-dimensional intensity $I = \frac{P_{in}}{NW}$[1]. The associated electric field amplitude E incident on each pixel is then $E = \sqrt{\frac{P_{in}2Z}{NW}}$, where the intensity I is given by $I = \frac{E^2}{2Z}$, and Z is the impedance of our two-dimensional free space. We can model the binary-phase hologram as a series of N Dirac delta functions, spaced W apart, with weights of $\pm W\sqrt{\frac{P_{in}2Z}{NW}}$, depending on the transmission of each pixel. A more accurate model would convolve the delta functions with a rectangular pixel aperture of width W, which would result in the output plane image being multiplied by a slowly varying sinc function. This does not alter the results of the following analysis, and the affect of the additional sinc envelope in the output plane is detailed in §3.3.5. Thus we can write $H(X)$ analytically as

---

[1]Although such a one-dimensional intensity has no physical meaning, it simplifies and avoids unnecessary over-complication if we employ the concept of such an intensity illuminating our strip hologram, since the analysis is fundamentally 1-D in nature.
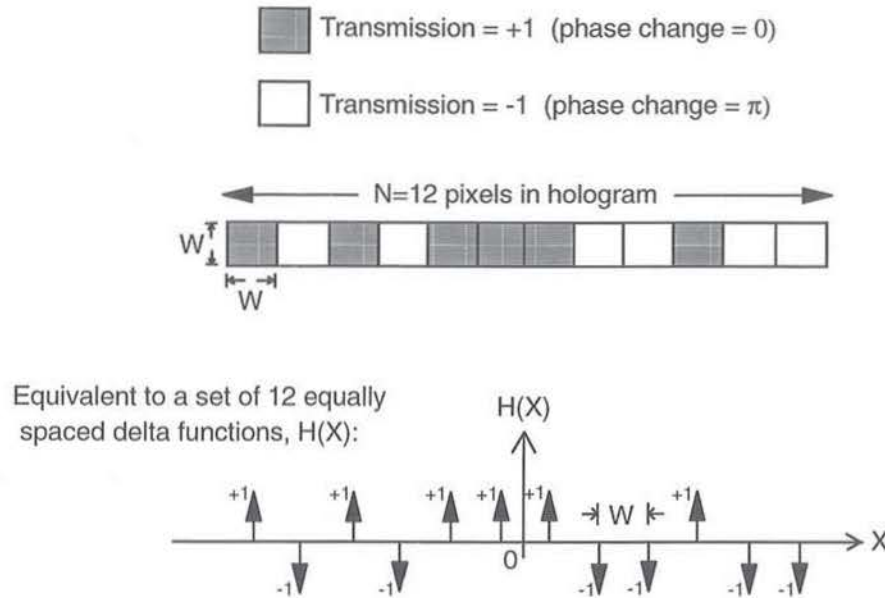
Figure 3.2: Arbitrary 1-D binary-phase hologram consisting of 12 pixels

a series of delta functions:

$$H(X) \;=\; W\sqrt{\frac{P_{in}2Z}{NW}}\sum_{k=0}^{N-1}S_k\delta\left(X-(k-\frac{N}{2}-\frac{1}{2})W\right)$$

The binary-phase modulation of the kth pixel is represented by S_k which is either $+1$ or -1. From fourier theory, a pair of delta functions transform to a cosine expression when they are of the same sign, and to a sine expression when they are of opposite signs. This is illustrated in figure (3.3). By pairing the delta functions which are equally positioned either side of the mid-point of the hologram and taking the fourier transform of each pair, we get a series of sinusoids of ever increasing spatial frequency. The output image $h(x)$ is therefore built up by a series of sinusoids of equal amplitude:

$$h(x) \;\rightleftharpoons\; H(X)$$

$$h(x) \;=\; \sqrt{\frac{2\pi}{f\lambda}}\int_{-\infty}^{\infty}H(X)e^{-j\frac{2\pi x}{f\lambda}X}dX$$

$$h(x) \;=\; \sqrt{\frac{2\pi}{f\lambda}}W\sqrt{\frac{P_{in}2Z}{NW}}2\sum_{k=0}^{\frac{N}{2}-1}a_k\cos\left(\frac{(2k+1)\pi Wx}{f\lambda}\right)+jb_k\sin\left(\frac{(2k+1)\pi Wx}{f\lambda}\right)$$

$$(3.1)$$

The optical fourier transform is performed by a lens of focal length f, and the incident light is assumed to be of wavelength λ. The expression $\sqrt{\frac{2\pi}{f\lambda}}W\sqrt{\frac{P_{in}2Z}{NW}}2$, which is an electric

Even-symmetrical pair of delta functions $h(x)= 2\cos\left(\dfrac{(2k+1)\pi Wx}{f\lambda}\right)$

(a)

Odd-symmetrical pair of delta functions $h(x)= 2j\sin\left(\dfrac{(2k+1)\pi Wx}{f\lambda}\right)$

(b)
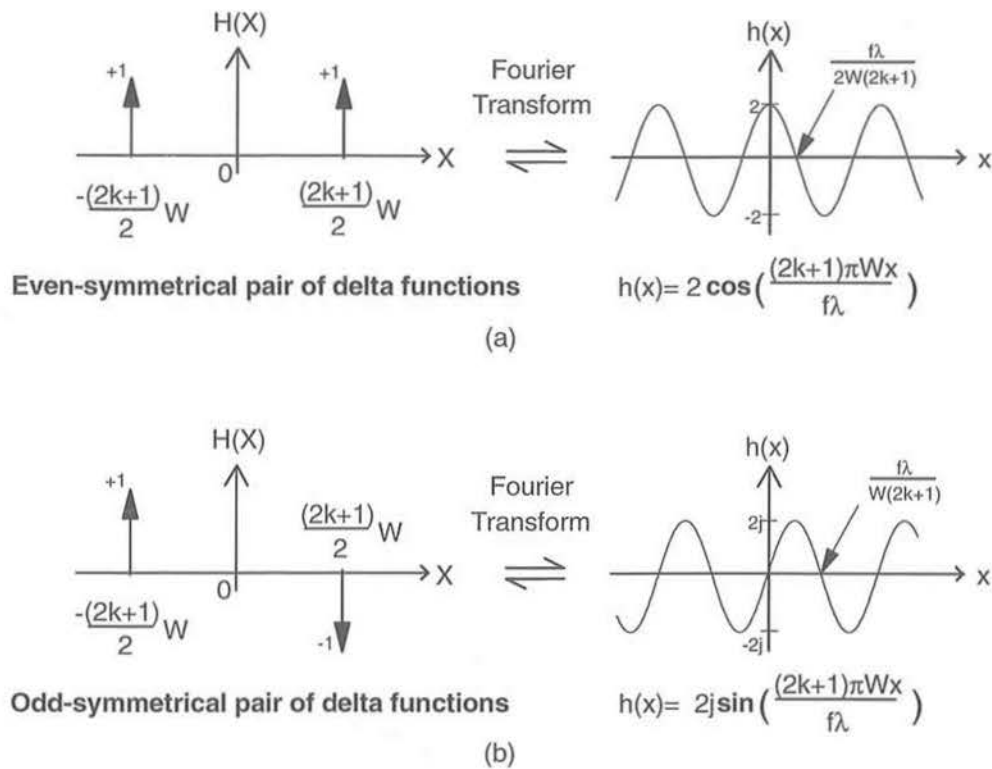
Figure 3.3: A pair of delta functions fourier-transforms to a sinusoid

field amplitude, is represented by the symbol A_0 in order to make the algebra clearer. The coefficients a_k and b_k are orthogonal to each other. If the hologram $H(X)$ has an even symmetry about its mid-point, then we find that the set of elements $\{b_k\} = 0$, whereas if it has an odd symmetry then $\{a_k\} = 0$. Most holograms do not have perfectly odd or even symmetry so the sets of coefficients $\{a_k\}$ and $\{b_k\}$ each contain the elements $-1, 0$ and 1. This is shown in figure (3.4), where the small arbitrary hologram of figure (3.2) is transformed to produce an output image given by the summation of 6 sinusoids of ever increasing spatial frequency. For the sake of simplicity, we shall assume henceforth that the hologram $H(X)$ has an even symmetry. Appendix A.3 shows that the results of the analysis are the same for the case of a non-symmetrical hologram.

Hence we can consider the output image $h(x)$ to be given by a summation of cosines of unit amplitude, and ever increasing spatial frequency - a type of fourier series:

$$h(x) \;=\; A_0 \sum_{k=0}^{\frac{N}{2}-1} a_k \cos\left(\frac{(2k+1)\pi Wx}{f\lambda}\right) \tag{3.2}$$

$$H(X) \rightleftharpoons h(x) = 2.\cos\left(\frac{\pi W x}{f\lambda}\right) + 2j.\sin\left(\frac{3\pi W x}{f\lambda}\right) - 2.\cos\left(\frac{5\pi W x}{f\lambda}\right)$$

$$+ 2.\cos\left(\frac{7\pi W x}{f\lambda}\right) - 2.\cos\left(\frac{9\pi W x}{f\lambda}\right) + 2j.\sin\left(\frac{11\pi W x}{f\lambda}\right)$$

$$\{a_k\} = [\,1\ \ 0\ \ \text{-}1\ \ 1\ \ \text{-}1\ \ 0\,] \qquad \{b_k\} = [\,0\ \ 1\ \ 0\ \ 0\ \ 0\ \ 1\,]$$
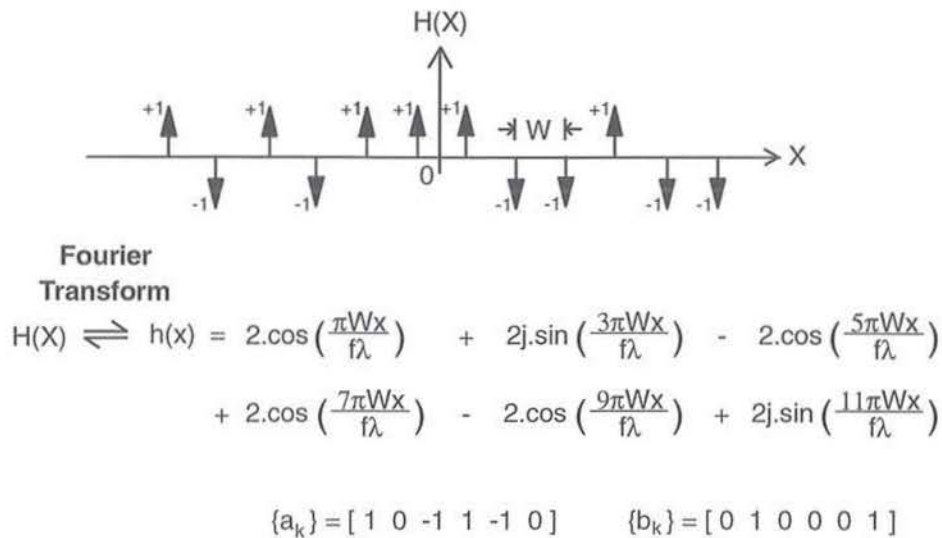
Figure 3.4: Arbitrary 1-D binary-phase hologram and its fourier transform

3.3.2 Steering Light to a Single Spot

Using algorithms such as simulated annealing, the values of the coefficients $\{a_k\}$ are ultimately determined so as to maximise the intensities of the p spots of light at positions $(x_1, x_2, ..., x_p)$, while keeping them of uniform intensity, avoiding spurious light concentrations and minimising noise. To begin with though, as with most holograms, we assume that the hologram is only directing the light to a single spot at a position x_p. The intensity of that single spot of light is given by $I_p = |h(x_p)|^2$, where the amplitude $h(x_p)$ of the light is given from equation (3.2) by:

$$h(x_p) = A_0 \sum_{k=0}^{\frac{N}{2}-1} a_k \cos\left(\frac{(2k+1)\pi W x_p}{f\lambda}\right)$$

Since binary-phase holograms are digital and discrete in nature, we find that the same is true for x_p. We can only direct the light to certain discrete positions in the output plane given by $x_p = \frac{nf\lambda}{NW}$, where n is an integer ranging from 0 to $N/2$. Given that the variables k,n and N can all take on fairly arbitrary integer values, then the product $\frac{(2k+1)\pi n}{N}$ will yield an arbitrary result as well. Once we take the cosine of that product, all we can predict about the result of that cosine operation is that it will lie somewhere between -1 and $+1$. Although we could explicitly calculate that value, the result is still to all intents and purposes *random*. Hence by assuming that the term $\cos\left(\frac{(2k+1)\pi W x_p}{f\lambda}\right)$ is a *random variable*, we can use stochastic analysis to get an insight into how bright we can expect to make the spot of light at x_p. We define the *expected* amplitude of the spot of light A_p as equal to the

expected value of $h(x_p)$, so that:

$$
\begin{aligned}
A_p &= E\{h(x_p)\} \\
&= E\left\{A_0 \sum_{k=0}^{\frac{N}{2}-1} a_k \cos\left(\frac{(2k+1)\pi W x_p}{f\lambda}\right)\right\} \\
&= A_0 \sum_{k=0}^{\frac{N}{2}-1} E\left\{a_k \cos\left(\frac{(2k+1)\pi W x_p}{f\lambda}\right)\right\}
\end{aligned} \tag{3.3}
$$

We are now interested in calculating the expected value of the kth component in the summation of equation (3.3):

$$
E\left\{a_k \cos\left(\frac{(2k+1)\pi W x_p}{f\lambda}\right)\right\}
$$

The coefficients $\{a_k\}$ are determined so as to maximise the above expectation, and hence the possible spot intensity. This can be done by choosing the value of a_k for a particular k to equal the sign of $\cos\left(\frac{(2k+1)\pi W x_p}{f\lambda}\right)$. By doing this, we are ensuring that all the components of the summation at the spot position x_p are positive, and so add up constructively to get the maximum possible amplitude of the light. We can calculate analytically the value of the expectation from such an algorithm by substituting the variable $\mathcal{X} = \frac{(2k+1)\pi W x_p}{f\lambda}$ and finding $E\{|\cos(\mathcal{X})|\}$ for $-\pi < \mathcal{X} \leq \pi$. By making $\mathcal{X}$ a continuous variable, the average value of $|\cos(\mathcal{X})|$ is given by:

$$
\begin{aligned}
E\{|\cos(\mathcal{X})|\} &= \frac{\int_{-\frac{\pi}{2}}^{\frac{\pi}{2}} \cos(\mathcal{X})d\mathcal{X}}{\pi} \\
&= \frac{1}{\pi}[\sin(\mathcal{X})]_{-\frac{\pi}{2}}^{\frac{\pi}{2}} \\
&= \frac{2}{\pi}
\end{aligned}
$$

This is demonstrated in numerical simulation where we use kY instead of $\mathcal{X}$, and let Y take on values from 0 to $\pi/2$ in discrete steps of π/N, as in the case for a binary-phase hologram. For each value of Y, we let k increment from 1 to $N/2$, and for each increment we calculate the result of $|\cos(kY)|$. Thus for each value of Y we have $N/2$ results or 'samples', from which we can calculate the average. We then plot the average result of $|\cos(kY)|$ as a function of Y. For a hologram of $N = 240$ pixels, the plot shown in figure (3.5) demonstrates that the average or expected value of $|\cos(kY)|$ is indeed very close to $2/\pi = 0.6366$ for the most part. What is interesting to note is that for $Y = \pi/2R$, where R is an integer, then the expected value is higher than $2/\pi$, and is actually equal to $1/R \sin \frac{\pi}{2R}$. The value of Y in this case corresponds to the output spot position when the hologram is a regular binary-phase grating of period $2R$ pixels. A regular grating can be thought of as a special type of hologram with enhanced properties, such as the ability to steer light to a particular position more efficiently.

Average $= \frac{2}{\pi}$, except for $Y = \frac{\pi}{2R}$ when Average $= \dfrac{1}{R \sin\left(\frac{\pi}{2R}\right)}$
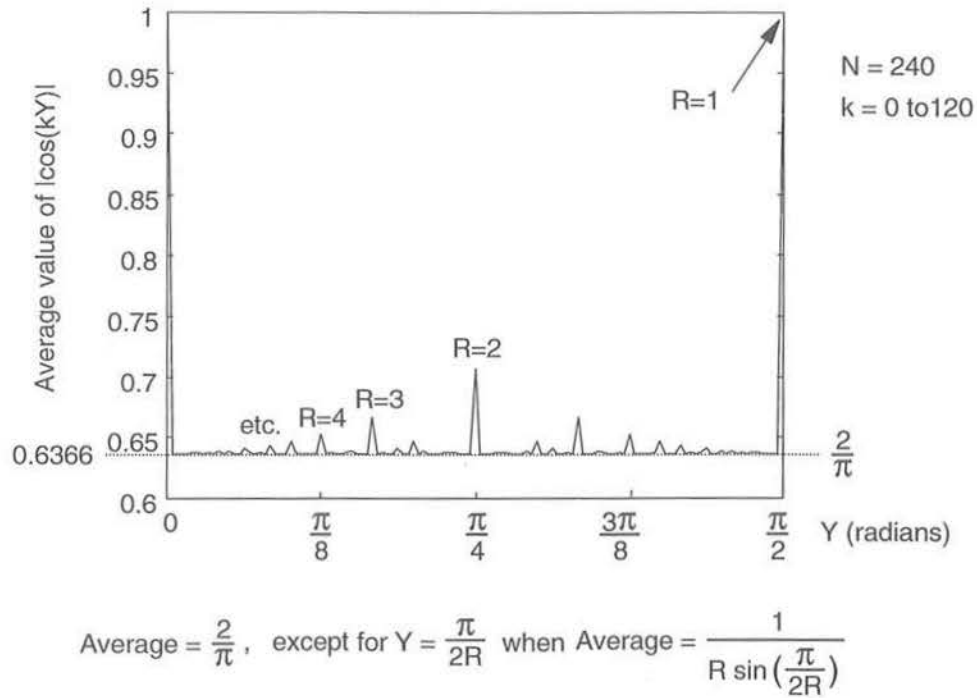
Figure 3.5: Expected values of $|\cos(kY)|$

Thus if we are steering the light to just a single output spot, we know that:

$$E\left\{ a_k \cos\left(\frac{(2k+1)\pi W x_p}{f\lambda}\right)\right\} = \frac{2}{\pi} \quad \text{for a hologram}$$

$$= \frac{1}{R\sin\frac{\pi}{2R}} \quad \text{for a grating of period } 2R \quad (3.4)$$

The resulting expected amplitude A_p of the spot of light, due to a hologram of N pixels steering light to an output position at x_p, is independent of that position, and is given by substituting equation (3.4a) into (3.3):

$$A_p = A_0 \frac{N}{\pi} \quad (3.5)$$

This tells us that the amplitude A_p of the spot of light increases linearly with the number of pixels in the hologram. This is what we would intuitively expect: larger holograms with more pixels produce more intense and better defined spots of light. The expected peak amplitude for a binary-grating of N pixels, regular period $2R$ pixels (which directs light to a single output spot positioned at $x_p = \frac{f\lambda}{2RW}$), is given using equation (3.4b) substituted into (3.3):

$$A_p = A_0 \frac{N}{2R\sin\left(\frac{\pi}{2R}\right)} \quad (3.6)$$

31

It can be seen that as R becomes large, the amplitude of the spot of light given by equation (3.6) tends towards the same as the amplitude for a spot of light due to a hologram of the same number of pixels, given by equation (3.5).

3.3.3 Fanning Out to Multiple Spots

We now want to find the expected value of the kth component of the summation, given that the hologram has to fan out to p spots of light, at positions $(x_1, x_2, ..., x_p)$ in the $+1$ order. As is the case for the huge majority of holograms, we assume that the hologram is not a regular grating (which can only direct the light to one position anyway), so that the expected value of $\left|\cos\left(\frac{(2k+1)\pi W x_p}{f\lambda}\right)\right|$ is $2/\pi$. In addition, we now assume that we have p *independent* random variables in the set $\left\{\cos\left(\frac{(2k+1)\pi W x_p}{f\lambda}\right)\right\}$, with an element corresponding to each value of x_p, and each element having the same stochastic properties. We also assume that each random variable has an equal chance of being positive or negative, such that:

$$prob\left\{\cos\left(\frac{(2k+1)\pi W x_p}{f\lambda}\right) > 0\right\} = 1/2.$$

This implies that the probability that the random variable $\cos\left(\frac{(2k+1)\pi W x_p}{f\lambda}\right)$ associated with each position $(x_1, x_2, ..., x_p)$ is positive at all those p positions of the spots of light, is $\left(\frac{1}{2}\right)^p$. Given that they are all positive, then the average expected value for each random variable, or the average k^{th} component value, is $\frac{2}{\pi}$.

The probability that only $(p-1)$ of the random variables are positive but that one is negative, for the kth component $\cos\left(\frac{(2k+1)\pi W x_p}{f\lambda}\right)$, must be $\left(\frac{1}{2}\right)^{p-1}\left(\frac{1}{2}\right)p$ (using basic combination theory.) Given that we have this case of $(p-1)$ of the kth components being positive and one being negative, then the average expected value of the kth component across the p spots of light is:

$$\frac{\frac{2}{\pi}(p-1) + \left(-\frac{2}{\pi}\right).1}{p} = \frac{2(p-2)}{\pi p}$$

This procedure can be continued for the general case where out of the p positions of the spots of light, $(p-q)$ of the kth components are positive and q are negative. The probability of $(p-q)$ random variables being positive, and q being negative is given by:

$$\left(\frac{1}{2}\right)^{p-q}\left(\frac{1}{2}\right)^q \frac{p!}{q!(p-q)!} = \left(\frac{1}{2}\right)^p \frac{p!}{q!(p-q)!}$$

The average expected value of $\cos\left(\frac{(2k+1)\pi W x_p}{f\lambda}\right)$ for each of those p spots is given by:

$$\frac{2}{\pi}\left(\frac{p-2q}{p}\right)$$

For the case when the majority of the values of $\cos\left(\frac{(2k+1)\pi W x_p}{f\lambda}\right)$ at the p spot positions are positive, we let $a_k = +1$. Conversely, when the opposite is true, and the majority of the

values are negative at the p spot positions, then we let $a_k = -1$; otherwise we allow a_k to be randomly $+1$ or -1. In this way, we are maximising the amplitudes of the spots of light whilst also minimising the noise.

We can write an expression for the expected value of $a_k \cos\left(\frac{(2k+1)\pi W x_p}{f\lambda}\right)$ as a summation of all the expected values of $a_k \cos\left(\frac{(2k+1)\pi W x_p}{f\lambda}\right)$ multiplied by their probability of occurrence, with the assumption that p is even:

$$E\left\{a_k \cos\left(\frac{(2k+1)\pi W x_p}{f\lambda}\right)\right\} = \left\{\left(\frac{1}{2}\right)^p \frac{2}{\pi} + \left(\frac{1}{2}\right)^p p\left(\frac{p-2}{p}\right)\frac{2}{\pi} + \ldots \right.$$
$$+ \left(\frac{1}{2}\right)^p \frac{p!}{\frac{p}{2}!\frac{p}{2}!}\left(\frac{p-2\frac{p}{2}}{p}\right)\frac{2}{\pi} + \ldots$$
$$\left. + \left(\frac{1}{2}\right)^p p\left(\frac{p-2}{p}\right)\frac{2}{\pi} + \left(\frac{1}{2}\right)^p \frac{2}{\pi}\right\}$$

The first half of the series is positive since $a_k = +1$ and the second half of the series is also positive because the expected value of the elements is negative but now $a_k = -1$. Since the series is symmetric about the middle element we can write:

$$E\left\{a_k \cos\left(\frac{(2k+1)\pi W x_p}{f\lambda}\right)\right\} = 2\frac{2}{2^p\pi}\sum_{q=0}^{\frac{p}{2}-1}\frac{p!}{q!(p-q)!}\left(\frac{p-2q}{p}\right)$$
$$+ \frac{1}{2^p}\frac{p!}{\frac{p}{2}!\frac{p}{2}!}\cdot 0$$
$$= \frac{4}{\pi 2^p}\left\{\sum_{q=0}^{\frac{p}{2}-1}\frac{p!}{q!(p-q)!} - 2\sum_{q=0}^{\frac{p}{2}-1}\frac{(p-1)!}{(q-1)!(p-q)!}\right\} \tag{3.7}$$

From consideration of the binomial expansion[2] of 2^p, for $p =$ even number, we can assume:

$$\sum_{q=0}^{\frac{p}{2}-1}\frac{p!}{q!(p-q)!} = \frac{1}{2}\left(2^p - \frac{p!}{\frac{p}{2}!\frac{p}{2}!}\right) \tag{3.8}$$

and that:

$$\sum_{q=0}^{\frac{p}{2}-1}\frac{(p-1)!}{(q-1)!(p-q)!} = \frac{2^p}{4} \tag{3.9}$$

Substituting equations (3.8) and (3.9) into equation (3.7) we get:

$$E\left\{a_k \cos\left(\frac{(2k+1)\pi W x_p}{f\lambda}\right)\right\} = \frac{4}{\pi 2^p}\left(\frac{2^p}{2} - \frac{p!}{2\frac{p}{2}!\frac{p}{2}!} - \frac{2^p}{2}\right)$$
$$= \frac{2}{\pi}\frac{p!}{2^p\frac{p}{2}!\frac{p}{2}!}$$
$$= \frac{2}{\pi}F(p) \tag{3.10}$$

---

[2]see Appendix A.2 and equations (A.3) and (A.4)

Thus the expectation is now reduced by a factor $\frac{p!}{2^p\frac{p}{2}!\frac{p}{2}!}$, which we represent by the function $F(p)$ such that for the case when p is an even number:

$$F(p) = \frac{p!}{2^p\frac{p}{2}!\frac{p}{2}!} \tag{3.11}$$

In Appendix A.4, figure (A.5) plots the solution to $F(p)$ as p varies from 1 to 20. For the case when the fanout p is an odd number, then a similar analysis to the above yields the result that:

$$F_{odd}(p) = \frac{(p-1)!}{2^{(p-1)}\frac{(p-1)}{2}!\frac{(p-1)}{2}!} = F(p-1) \tag{3.12}$$

For $p = 1$ this gives the result that $F(1) = 1$, (assuming $0! = 1$.) Thus equation (3.10) agrees with the results derived for the hologram steering the light to just one position, and expressed in equation (3.4a). Appendix A.4 gives a useful approximation for $F(p)$ which becomes accurate with high p, such that $F(p) \rightarrow \sqrt{\frac{2}{\pi p}}$. Using equation (3.3) in conjunction with equation (3.10), the expected amplitude of *one* of the fanned-out spots of light is given by:

$$
\begin{aligned}
A_p &= A_0 \sum_{k=0}^{\frac{N}{2}-1} E\left\{ a_k \cos\left(\frac{(2k+1)\pi W x_p}{f\lambda} \right) \right\} \\
&= A_0 \sum_{k=0}^{\frac{N}{2}-1} \frac{2}{\pi} F(p) \\
&= A_0 \frac{N}{\pi} F(p) \tag{3.13}
\end{aligned}
$$

Thus the amplitude of each spot of light is still proportional to the number of pixels in the hologram, but reduces with the number of spots the hologram has to fan out to. This is what we would intuitively expect to happen.

3.3.4 Calculation of Diffraction Efficiency and SNR

The shape of the finest detail (*e.g.* the intensity profile of a spot of light) in a holographic image is governed by the shape of the illuminating aperture on the other side of the fourier lens. They form a fourier transform pair. Since the illuminating aperture is rectangular in shape, it follows that the intensity profile is close to a *sinc* function in shape. When we are steering light to one spot or many spots, we are concentrating as much power as possible into the smallest possible area. But the smallest area into which we can concentrate that power is limited by the fourier resolution of the hologram. The smallest width Δx into which we can concentrate light is given by[116]:

$$\Delta x = \frac{2f\lambda}{NW} \tag{3.14}$$

This is the width of the spot of light, which is inversely proportional to the hologram aperture NW. The power in the spot P_p is given by integrating the intensity profile over
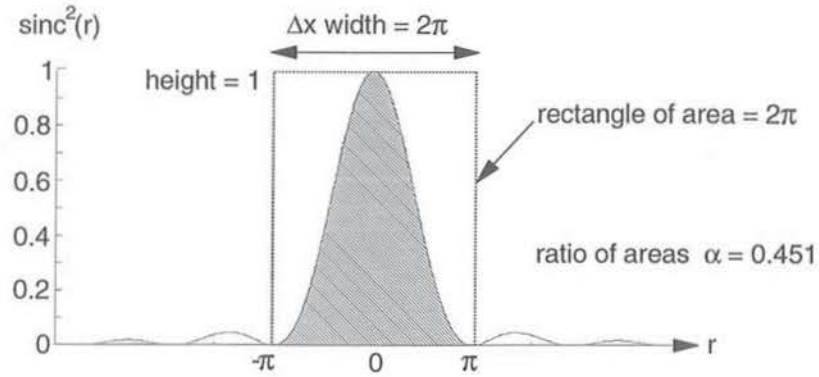
Figure 3.6: Normalised intensity profile of a spot of light

the spot width. Since we know the shape of the intensity profile, its width and its maximum intensity, we can calculate the total power within the spot. This is given by the product of the spot width and the square of the spot amplitude (A_p^2), multiplied by a 'shape factor' α to take into account the fact that the spot has a $\text{sinc}^2(x)$ shape, rather than a rectangular profile. The shape factor α is defined as the ratio of the area in the main lobe of a $\text{sinc}^2(x)$ function to the rectangle enclosing it. This is illustrated in figure (3.6).

$$\begin{aligned} \alpha &= \frac{1}{2\pi} \int_{-\pi}^{\pi} \text{sinc}^2(r)\,dr \\ &= 0.451 \end{aligned} \tag{3.15}$$

Using equation (3.13) for the expected spot amplitude, equation (3.14) for its width, Parseval's Theorem for power conservation (which requires an additional factor of $\frac{1}{2\pi}$), and substituting back for A_0, we find that the power P_p in a single spot of light is:

$$\begin{aligned} P_p &= \frac{1}{2\pi} \int_{x_p - \frac{\Delta x}{2}}^{x_p + \frac{\Delta x}{2}} \frac{|h(x)|^2}{2Z}\,dx \\ &= \frac{1}{2\pi} \left\{ \frac{1}{2Z} \alpha A_p^2 \Delta x \right\} \\ &= \frac{1}{2\pi} \frac{1}{2Z} \alpha \frac{8\pi W P_{in} 2Z}{Nf\lambda} \frac{N^2 F^2(p)}{\pi^2} \frac{2f\lambda}{NW} \end{aligned} \tag{3.16}$$

$$P_p = \frac{8\alpha F^2(p)}{\pi^2} P_{in} \tag{3.17}$$

If the hologram is fanning out the light to p spots of light, and the total input power through the hologram is P_{in}, then the efficiency η of the hologram is given by:

$$\eta = \frac{p.P_p}{P_{in}}$$
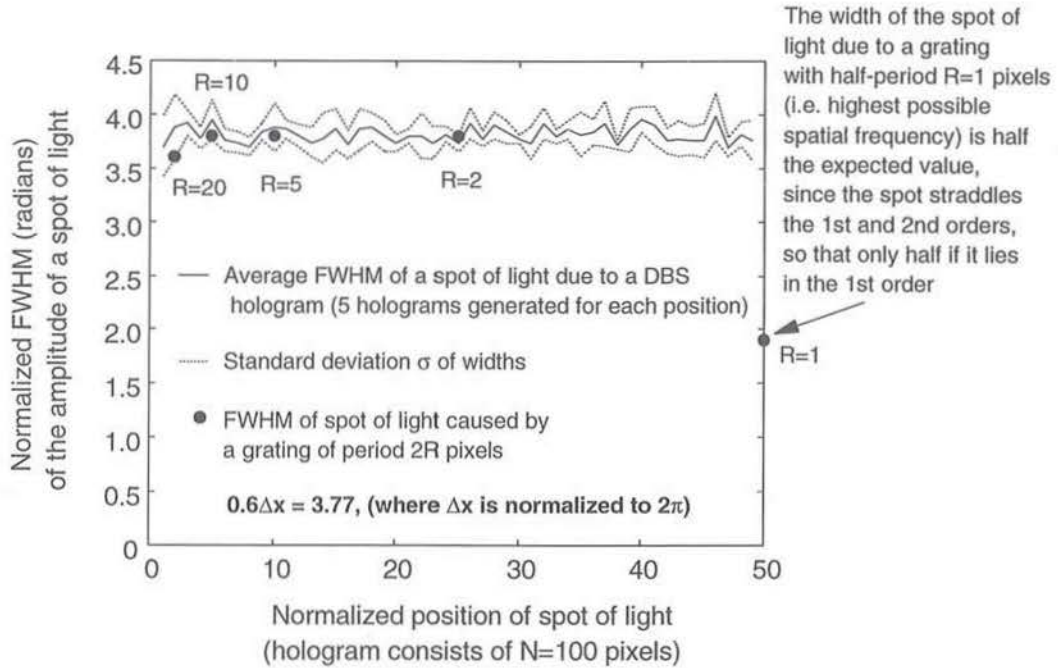
Figure 3.7: FWHM of holographic peak, normalised so that $\Delta x = 2\pi$

$$= \left\{ p \frac{8\alpha F^2(p)}{\pi^2} P_{in} \right\} / P_{in}$$

$$= \frac{8\alpha}{\pi^2} p F^2(p) \tag{3.18}$$

A hologram which steers light to just one position, *i.e.* $p = 1$, should have a diffraction efficiency given by $\eta = \frac{8\alpha}{\pi^2} = 36.5\%$, since $pF^2(p) = 1$. But for a large fanout where $p \gg 1$, then from Appendix A.4 we find that $pF^2(p) \to \frac{2}{\pi}$, so that the diffraction efficiency becomes $\eta \to \frac{16\alpha}{\pi^3} = 23.3\%$. This means that we should expect the diffraction efficiency of a hologram to reduce down towards 23.3% as the light is fanned out to multiple positions in the output plane.

The shape factor α is assumed to be the same for a spot of light formed by a regular grating, since the spot still has the same width as for one due to a hologram, and the fourier resolution limit implies that the shape of the intensity profile within this width cannot vary significantly. Figure (3.7) shows that the full-width at half-maximum-amplitude of a spot ($\sim 0.6\Delta x$) is virtually the same for spots produced either by a grating or by a direct binary-search (DBS) hologram. We can use this result to support our assumption that the shape factor $\alpha = 0.451$ for all spots of light, including those produced by a grating. The power in the spot of light produced by a grating is calculated using equation (3.16) but substituting

equation (3.6) to give:

$$P_p = \frac{2\alpha}{R^2 \sin^2\left(\frac{\pi}{2R}\right)} P_{in} \tag{3.19}$$

This means that the efficiency of a grating is given by:

$$\eta = \frac{P_p}{P_{in}}$$

$$= \frac{2\alpha}{R^2 \sin^2 \frac{\pi}{2R}} \tag{3.20}$$

For a grating with a half-period $R = 1$ pixel (which is the highest possible spatial frequency), the diffraction efficiency η is equal to α ($= 45.1\%$), rather than 2α or 90.2%, since the spot of light produced by the grating is now 'straddling' the first and second orders. This means that only half of the spot of light technically lies in the area of interest, the first order, and this is illustrated in figure (3.7). As such, the diffraction efficiency, as earlier defined, remains below 50%. As the number of pixels per period $2R$ gets large, so the grating contains fewer periods, and the diffraction efficiency reduces:

$$\eta \rightarrow \frac{8\alpha}{\pi^2}$$

$$\eta = 36.5\%$$

This lower efficiency is the same diffraction efficiency as one would expect from a hologram which is steering the light to a single position at an arbitrary position in the output field. It should be noted that these are the diffraction efficiencies as calculated without taking the sinc envelope into account. This is done in §3.3.5.

Using conservation of power within the -1,0,+1 orders, which extend over a distance $f\lambda/W$, as shown in figure (3.1), we can estimate the average noise-amplitude A_n. The total power in those orders equals the total input power P_{in}, such that the total power in the desired spots of light plus all the integrated noise power which lies between the desired spots of light must equal the total input power P_{in}. If we assume that the hologram has a diffraction efficiency η, then the total power of the spots of light in those orders will be $2\eta P_{in}$. The total integrated noise power is calculated in a similar way as was used with equation (3.16) to calculate the power in a spot of light. Thus from conservation of power we have:

$$P_{in} = 2\eta P_{in} + \frac{1}{2\pi} \frac{(A_n)^2}{2Z} \frac{f\lambda}{W}$$

Rearranging this expression gives us the average noise-amplitude:

$$A_n = \sqrt{\frac{2\pi W P_{in}(1 - 2\eta)2Z}{f\lambda}} \tag{3.21}$$

Given that we now have expressions for the expected spot-amplitude A_p and the average noise-amplitude A_n, we can find an expression for the expected SNR. For an arbitrary fan-out hologram this is given by additionally using equations (3.13) and (3.18), and substituting back for A_0:

$$
\begin{aligned}
SNR &= \left(\frac{A_p}{A_n}\right)^2 \\
&= \frac{F^2(p)N^2}{\pi^2}\frac{8ZP_{in}}{NW^2}\frac{W^2}{2ZP_{in}(1-2\eta)} \\
&= \frac{4F^2(p)N}{\pi^2(1-2\eta)} \\
&= \frac{4F^2(p)N}{\pi^2\left(1-\frac{16\alpha pF^2(p)}{\pi^2}\right)} \\
&= \frac{4F^2(p)N}{\pi^2-16\alpha pF^2(p)} \\
&\approx \frac{N}{2p} \quad \text{for large } p
\end{aligned}
\tag{3.22}
$$

The SNR for a grating is calculated using equations (3.6), (3.20) and (3.21) to give us:

$$
\begin{aligned}
SNR &= \left(\frac{A_p}{A_n}\right)^2 \\
&= \frac{N}{R^2\sin^2\frac{\pi}{2R}(1-2\eta)} \\
&= \frac{N}{R^2\sin^2\frac{\pi}{2R}-4\alpha}
\end{aligned}
\tag{3.23}
$$

Thus for 1-D holograms we find that the SNR is proportional to the number of pixels N and for a large fanout is inversely proportional to the fanout p. Both these results are intuitively reasonable.

Some may question the lowness of the expected efficiency (36.5%) since the figure of about 45%[117][118] is often presented as being the efficiency of a 1-D binary-phase hologram. The discrepancy is due to the fact that only for a grating of maximum spatial frequency do we get an efficiency of 45.1%. If we use a grating with the same number of pixels but a lower spatial frequency (or fewer periods) then this efficiency is reduced towards 36.5%. Having said that, when the sinc envelope is included in the analysis, as in §3.3.5, we find that the efficiency of a binary grating is always 36.5%, whatever its spatial frequency. It is in fact impossible for a fanout binary hologram (or a binary grating) to have a diffraction efficiency greater than this figure of 36.5%.

3.3.5 Sinc Envelope

The analysis has used ideal delta-functions as a representation of the pixels in a hologram. In reality the pixels are of a finite width W which causes the output image to be multiplied
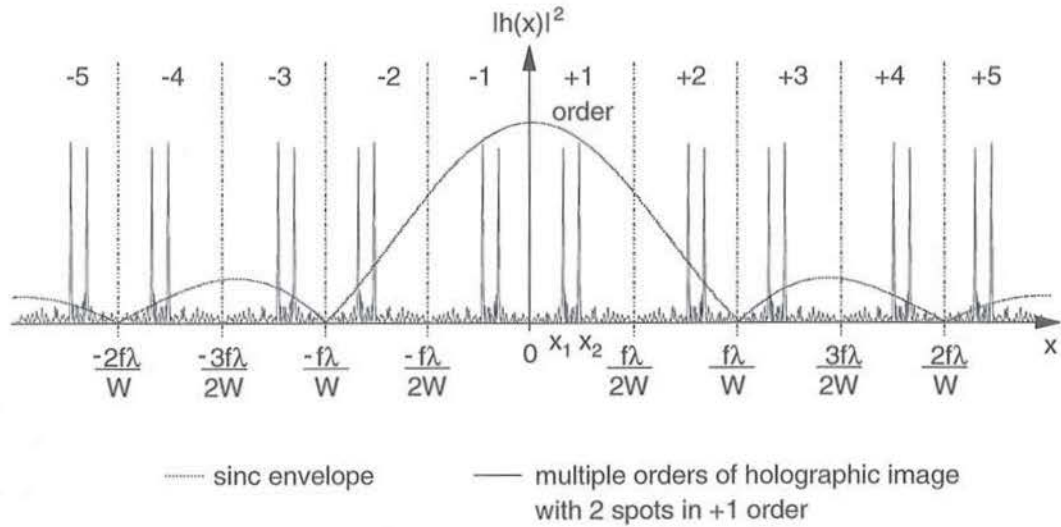
Figure 3.8: The *sinc* envelope due to the finite pixel width W

by an overall sinc envelope. If we assume that all the pixels in the hologram are of width W and are adjacent to each other such that there is no dead space, then the equation of the amplitude of the resulting sinc envelope is:

$$\frac{\sin \frac{W \pi x}{f \lambda}}{\frac{W \pi x}{f \lambda}} = \text{sinc}\left(\frac{W \pi x}{f \lambda}\right) \tag{3.24}$$

The image in the output plane is then given by $\text{sinc}\left(\frac{W \pi x}{f \lambda}\right) h(x)$. Figure (3.8) depicts an arbitrary holographic image consisting of 2 spots of light in the positive first order, with its associated sinc envelope. The figure demonstrates that most of the power of the holographic image is confined to the first order, and that the higher orders become progressively weaker. We redefine the amplitude of a spot of light to be $\text{sinc}\left(\frac{W \pi x_p}{f \lambda}\right) A_p$. For large N, the width $\Delta x = \frac{2 f \lambda}{N W}$ of a spot (see equation 3.14) is much smaller than the width of the lobe of the sinc function, which is simply $\frac{2 f \lambda}{W}$. This means that over the width of a spot, the slowly varying sinc envelope is almost constant. Thus modifying equation (3.17) gives us to a good approximation the power in one spot:

$$P_p = \frac{8 \alpha F^2(p)}{\pi^2} \text{sinc}^2\left(\frac{W \pi x_p}{f \lambda}\right) P_{in}$$

The overall efficiency is then defined as:

$$\eta = \frac{8 \alpha F^2(p)}{\pi^2} \sum_{n=1}^{p} \text{sinc}^2\left(\frac{W \pi x_n}{f \lambda}\right)$$

When all the peaks are close to the zero order, then the diffraction efficiency $\eta \to \frac{8 \alpha F^2(p)}{\pi^2}$, as before. As the peak positions $\{x_p\} \to \frac{f \lambda}{2W}$, *i.e.* are situated to the far side of the first order,

close towards the second order, then the diffraction efficiency $\eta \to \frac{8\alpha F^2(p)}{\pi^2} \frac{4}{\pi^2} = \frac{32\alpha F^2(p)}{\pi^4}$. It is obvious that the best diffraction efficiency is achieved for spots of light directed close to the zero order, or the optical axis of the system.

For a grating we can assume (using equation 3.19) that the power in the spot is given by:

$$P_p = \frac{2\alpha}{R^2 \sin^2\left(\frac{\pi}{2R}\right)} \mathrm{sinc}^2\left(\frac{W\pi x_p}{f\lambda}\right) P_{in}$$

But this expression can be simplified, since we know that the spot position is given by $x_p = \frac{f\lambda}{2RW}$, which means that the power in the spot is given by:

$$P_p = \frac{8\alpha}{\pi^2} P_{in}$$

The overall diffraction efficiency of a grating is then given by:

$$\eta = \frac{8\alpha}{\pi^2}$$
$$= 36.5\%$$

This overall diffraction efficiency is essentially independent of the position of the spot or the periodicity of the grating, which is intuitively to be expected.

Since the sinc envelope is very slow moving compared to the intensity distribution around the peaks, we can assume that the SNR in the vicinity of the peaks stays the same, independent of the presence or absence of the sinc envelope.

3.3.6 Experimental Validation of Theory

In the preceding sections we have developed theoretical expressions for the expected diffraction efficiency η and SNR of holograms designed to steer light to one or more fanout positions. In this section, we attempt to demonstrate the validity of these derived expressions[3]. Unfortunately this is quite difficult to do, since binary-phase holograms have to be generated using non-deterministic optimisation algorithms, such as simulated annealing. For a good comparison between the theoretically derived expressions and the measured diffraction efficiencies and SNRs of actual calculated holograms, we have to be sure that the generated holograms are as optimal as possible. To generate the holograms, a two-stage direct binary search simulated annealing algorithm[119] was used. Holograms were generated to fanout and steer the light to either $p = 1,3,5,7,9$ or 11 random positions in the output plane. For each fanout number p, hundreds of holograms were calculated, and the parameters of the algorithm optimised to ensure that the best possible hologram was generated. A 'good' measurand hologram was ultimately selected to represent each fanout p on the basis of:

- uniformity of the output spots

---

[3]The effect of the overlaying sinc envelope is not required for the comparisons made in this section.

(a)   (b)
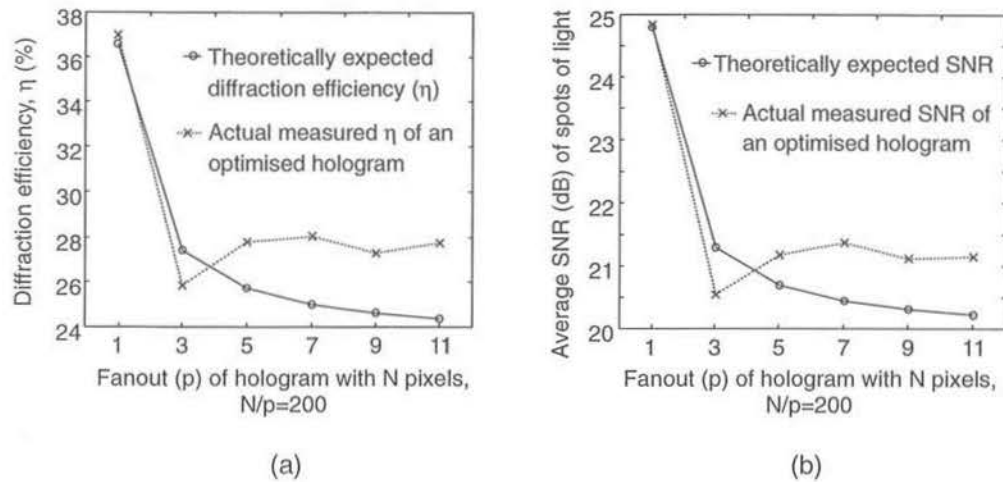
Figure 3.9: Comparison of measured and predicted 1-D hologram performance

- high diffraction efficiency

- low noise

Graphs plotting the theoretical expected diffraction efficiencies and SNRs compared with measured diffraction efficiencies and SNRs of the optimised actual generated holograms are shown in figure (3.9). To ensure a valid comparison between the various fanout holograms, the ratio of the number of pixels N to the fanout p was kept a constant, $N/p = 200$. We could always then assume with confidence that $N \gg p$. Table (3.1) shows the optimised parameters of the two-stage simulated annealing algorithm, which were use to generate the best hologram for each fanout number. The initial 'temperature' is T_0, while the 'rate of cooling' per iteration is T_{rate}. It was never possible to generate a hologram which produced

p	N	T_0	T_{rate}	No. of iterations
1	200	8.5×10^{-3}	0.7	10
3	600	30×10^{-3}	0.25	14
5	1000	35×10^{-3}	0.35	16
7	1400	35×10^{-3}	0.2	17
9	1800	40×10^{-3}	0.35	15
11	2200	40×10^{-3}	0.25	13

Table 3.1: Optimum algorithm parameters for hologram generation

totally uniform spots in the output plane, which is the main reason for the slight differences between the theoretical and the measured results. As the fanout increases, it becomes
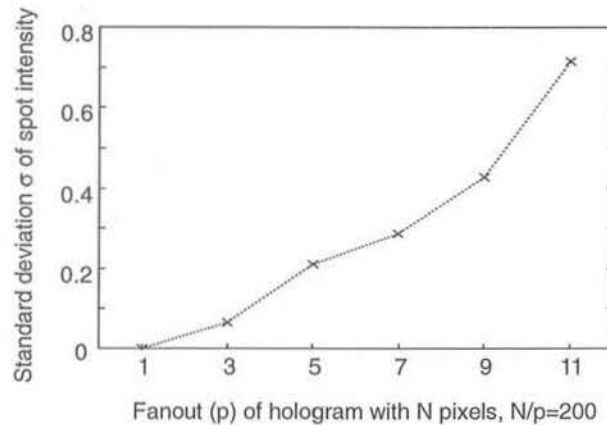
Figure 3.10: Increase of spot intensity non-uniformity with fanout p

more difficult to ensure the uniformity of the spot intensities, so that the departure from theoretical performance increases. The uniformity of the spot intensities was measured by calculating the normalised standard deviation σ of the spot SNRs. The almost linear increase in normalised standard deviation σ with fanout p is shown in figure (3.10). The simulated annealing algorithm generally finds a hologram solution which has a high diffraction efficiency, but compromises slightly on the uniformity of the spot intensities. This is probably preferable to a solution which has very uniform spot intensities, but a low diffraction efficiency.

The SNRs and relative diffraction efficiencies for various diffraction gratings and holograms have also been experimentally measured using an FLC SLM in a $4f$ free-space experimental setup, described in §4.4. The measured SNRs and relative diffraction efficiencies, described in §4.4.3, §4.4.4 and §4.4.6, are in broad agreement with the theoretically derived values. The values of the actual experimentally determined SNRs and diffraction efficiencies, as well as their theoretical values, are given and compared in those sections.

3.3.7 Conclusions and Summary

We have derived theoretical expressions for the diffraction efficiencies and SNRs of holograms optimised for fanning out input light into single or multiple spots of uniform intensity. The derived theoretical expressions generally give the 'worst case' values for the diffraction efficiency and SNR, typically 2% lower diffraction efficiency and 1dB lower SNR than we get in practice. Thus they can be used as a close but slightly pessimistic guide to hologram performance. This is still useful for engineering design, since we can always assume that the hologram will perform better than theoretically expected. They also show that the diffrac-

tion efficiency of holograms is generally reduced for larger fanouts. The analysis also gives us a reference to ensure that the hologram generation algorithm is genuinely calculating optimal holograms. Thus for a hologram of N pixels, fanning out the light to p arbitrary positions, we can assume that the diffraction efficiency lies between $36.5\% \geq \eta > 23.3\%$ and is given by:

$$\eta \quad > \quad \frac{8\alpha p F^2(p)}{\pi^2} \tag{3.25}$$

We can also assume that the SNR of the hologram is better than:

$$SNR \quad \gtrsim \quad \frac{4F^2(p)N}{\pi^2 - 16\alpha p F^2(p)}$$
$$> \quad \frac{N}{2p} \tag{3.26}$$

These equations will be useful in the analysis and design of holographic interconnects and any fanout holograms used in telecommunications, where considerations of the power budget and cross-talk are important. Other physical effects such as unwanted reflections will tend to lower the SNR and efficiency. A good discussion of this is to be found in reference[90].

3.4   Deterministic Algorithm to Generate Large Holograms

3.4.1   Introduction

The analysis of §3.3 and also Appendix A.1 demonstrates the stochastic nature of binary-phase holograms. This may be one of the underlying reasons why non-deterministic algorithms, such as simulated annealing, are most efficient at generating optimum holograms. On the other hand, for very large holograms non-deterministic algorithms become unsuitable. This is because they are computationally very intensive, taking a long time to generate large holograms, and their multitude of algorithm parameters such as 'temperature' and 'rate of cooling' make it difficult to assess whether the optimum hologram is being found. However, the *Law of Large Numbers*[120] can be applied to the stochastic statistics of large binary-phase holograms. This law simply states that any fluctuations from an average in the long run will tend to be damped out. Applied to holograms, this means that the average component $E\left\{a_k \cos\left(\frac{(2k+1)\pi W x_p}{f\lambda}\right)\right\}$ from equation (3.10) for an optimised hologram should become ever closer to $2F(p)/\pi$ as the hologram gets larger. This means it becomes ever less likely for an optimum hologram solution to exist which is better than the theoretical best.

If we assume this to be the case, then a new fast and deterministic hologram generation algorithm becomes possible, which works with the Law of Large Numbers to give us optimum large holograms. It operates on an 'aperturing' principle, in a manner similar to (but the converse of) the analysis given in §3.3.3. We start by merely considering the two pixels at the centre of the hologram, and calculate their required values, as if they were the only pixels of
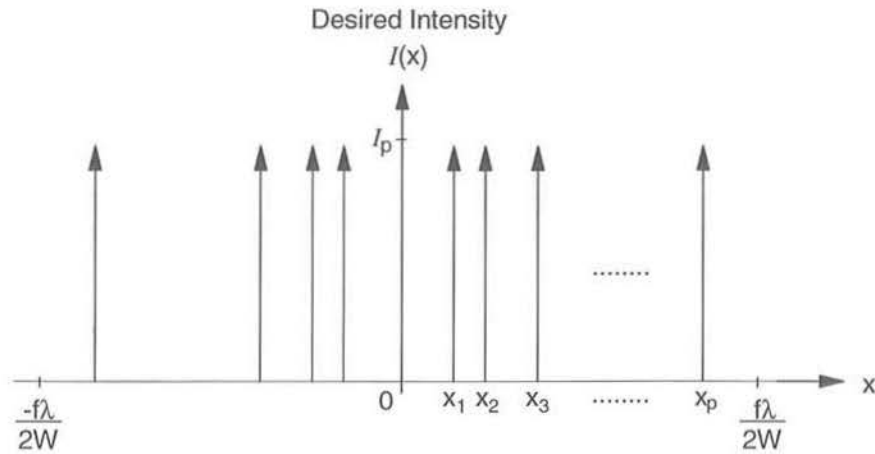
Figure 3.11: Arbitrary holographic image $\mathcal{I}(x)$ with a fanout of p spots

the hologram. We then chose the two pixels either side of the central two, and calculate what values they should take on to contribute positively to the performance of the hologram, *but independently of the values of any previous pixels calculated*. The process is continued with successive pairs of pixels either side of the existing hologram being analysed. In such a way, the aperture of the hologram is steadily increased, until its full size is achieved. We assume that all the independent contributions from the individual pixel pairs to the holographic image may either act positively to improve it greatly or even act to degrade it slightly, but that over all, the final result will be an average holographic image, corresponding to the theoretical best.

3.4.2   The Hologram Generation Algorithm

In Appendix A.3 we show that large symmetrical holograms should be just as good as large non-symmetrical holograms. As such, we will assume that our large hologram has an even symmetry. That means that the holographic image $h(x)$ from equation (3.2) is given by a summation of unit cosines:

$$h(x) = \sum_{k=0}^{\frac{N}{2}-1} a_k \cos\left(\frac{(2k+1)\pi W x}{f\lambda}\right)$$

In this case, the coefficients $\{b_k\}$ are all *zero* and it is the coefficients $\{a_k\}$ which need to be determined; being either $+1$ or -1. Let us consider an arbitrary desired image $\mathcal{I}(x)$ with p fanout spots located at the set of positions $\{x_1, x_2, ..., x_p\}$ as depicted in figure (3.11). Each position x in the image plane is made up of the sum of $N/2$ random samples of values between $+1$ and -1. It is apparent that the only parameter which can be manipulated to give the *actual* image $|h(x)|^2$ its desired form $\mathcal{I}(x)$, is the *sign* of the kth set of 'random samples'. Hence 'rules' for an algorithm can be formulated as follows:

44

- Choose a_k so that the *majority* of the elements in the kth set of p spots
  $$\left\{ a_k \cos\left(\frac{(2k+1)W}{2} x_1 \right), a_k \cos\left(\frac{(2k+1)W}{2} x_2 \right), ..., a_k \cos\left(\frac{(2k+1)W}{2} x_p \right) \right\}$$
  are *positive*.

- If the elements in the kth set $\left\{ a_k \cos\left(\frac{(2k+1)W}{2} x_1 \right), a_k \cos\left(\frac{(2k+1)W}{2} x_2 \right), \right.$
  $\left. ...., a_k \cos\left(\frac{(2k+1)W}{2} x_p \right) \right\}$ are equally positive and negative, then let a_k be chosen *randomly* to be $+1$ or -1.

Using these two rules, it can be seen that spots are favoured at the positions $\{x_1, x_2, ..., x_p\}$ since the algorithm always tries to cause the values of the kth sinusoid to be positive at those spot positions and randomly positive or negative elsewhere. As $N \longmapsto \infty$, then the spot intensities should tend to equalise as the *Law of Large Numbers* takes effect and makes the probability density functions (PDFs) of the spot positions become similar, and also since the spot intensities are also all equally (*i.e.* blindly) preferentially increased. Likewise, the regions between the spots should tend towards zero, since they are not 'favoured' and the expected value $E\{a_k \cos\left(\frac{(2k+1)Wx}{2} \right)\}$ is then close to zero. Given the constraints of equal spot intensity, and the essentially 'random nature' of the values of the component sinusoids, this algorithm causes the spot intensities to be maximised and all the conditions outlined above for a 'good' hologram[4] to be satisfied.

3.4.3 Final Word about Stability of Holograms

In the previous section, a distinction was made between the *desired* holographic image $\mathcal{I}(x)$ and the *actual* holographic image obtained $|h(x)|^2$ from a hologram $H(X)$. The holographic image $h(x)$ is made up as a series summation of sinusoids, such that from equation (3.1) we have:

$$h(x) = A_0 \sum_{k=0}^{\frac{N}{2}-1} a_k \cos\left(\frac{(2k+1)\pi W x}{f\lambda} \right) + j\, b_k \sin\left(\frac{(2k+1)\pi W x}{f\lambda} \right)$$

This is similar to a fourier series, but with the crucial difference that the fourier coefficients are usually continuous and both real and imaginary, whereas the coefficients of this series for $h(x)$, a_k and b_k, are limited to either ± 1 or 0. For a fourier series, the fourier coefficients generally tend towards zero as k tends towards infinity, so that the series converges to the required function. But the coefficients for the above series do not tend towards zero as k tends towards $N/2$ ($\to \infty$ for very large holograms.) Instead, the finite coefficients always have a modulus of unity. Thus all we can say about the series is that it lies on the boundary between convergence and divergence; stability and instability[5]. This means that despite any optimum hologram generation algorithm, the series for $h(x)$ will not converge to the desired

---

[4]See §3.3.6 for the qualities required of a 'good' hologram.

[5]This is essentially a property of 'chaotic' systems, where a quasi-stochastic situation arises, despite the deterministic nature of the system equations[121]. See Appendix A.1 for characteristic bifurcations in this system, which act as further evidence for chaotic behaviour in this function.

image $\mathcal{I}(x)$, but nor will it necessarily diverge[122]. Rather, the actual holographic image $|h(x)|^2$ can only be a close approximation to the desired image $\mathcal{I}(x)$, which is why it is always necessarily 'noisy' with a diffraction efficiency that is always less than ideal.

Chapter 4

Holographic Wavelength Filter

4.1 Introduction

As described in §1.2, the main thrust of this Ph.D. has been the development of digital holographic wavelength filtering as a new generic technology for WDM, although it has applications in other fields requiring tunable components. Holographic wavelength filtering is optically transparent, polarisation-insensitive, potentially low loss and allows multiple wavelength filtering with controllable relative transmission of each filtered wavelength. In addition, the technology offers high resolution over a large range, fast switching, low power consumption and reliability. All of these qualities make it suitable for application in WDM telecommunication systems, which require tunable sources and receivers, reconfigurable optical amplifiers, space-wavelength switches and routers. An overview of current wavelength filtering technologies for WDM is given in §1.2. In this chapter, the results of two experimental holographic filters are presented. The first one employing a reflective, folded-back architecture was the proof-of-principal demonstration of holographic wavelength filtering. It was polarisation-sensitive, very high loss (~ 57.7dB), and had a resolution of 2.5nm[101]. The second, improved experimental holographic wavelength filter employing a transmissive, linear $4f$ architecture was polarisation-insensitive, reduced loss (~ 22.8dB) and had a resolution of 1.3nm[102].

4.2 Principle of Operation

The principle of operation of the tunable holographic wavelength filter is based on the wavelength-dispersive nature of gratings. Polychromatic light is angularly dispersed by a grating, since the different wavelengths are diffracted through different angles. The basic equation[123] describing the angle of diffraction is:

$$\sin \alpha - \sin \beta = \frac{m\lambda}{d} \tag{4.1}$$
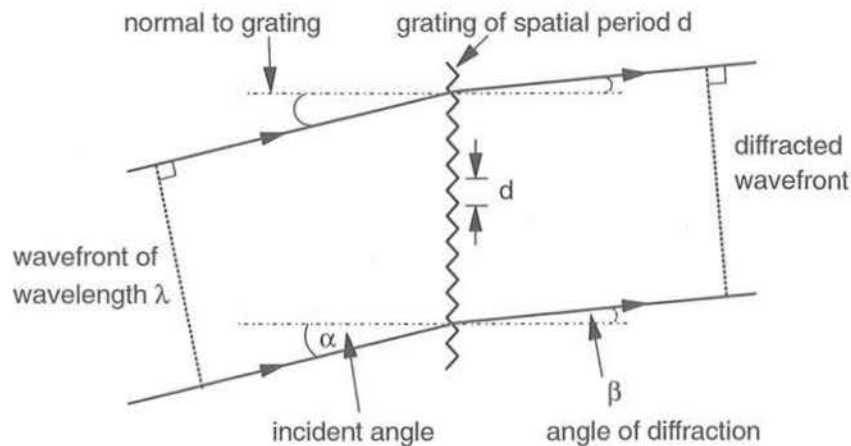
Figure 4.1: Diffraction of light due to a regular grating

where α is the angle of incidence of the collimated light, β is the angle with which the diffracted light emerges from the grating, λ is the wavelength, m (an integer) is the diffraction order and d is the spatial period of the grating. This is illustrated in figure (4.1). In practice, we are only interested in the positive first diffraction order, such that $m = +1$. Changing the spatial period d of the grating causes the angle of diffraction β of light of wavelength λ to change. This is the method to effect tuning of the filter. Using a spatial light modulator (SLM) instead of a grating enables us to have a programmable hologram (*i.e.* grating), whose spatial period d can be altered at will. A lens placed after the SLM converts the angular-separation of wavelengths to a spatial-separation. A spatial filter can then be used to arbitrarily select the desired wavelengths. Changing the spatial period of the hologram displayed on the SLM causes a different angular dispersion of wavelengths, which is then converted into a different spatial separation. Using the same spatial filter, different wavelengths can thus be selected, and ultimately tuned to. In the experimental holographic wavelength filter, a single-moded (SM) optical fibre acts as the spatial filter, since it only accepts a range of wavelengths which are incident across its core. In addition, a fixed diffraction grating is used in conjunction with the SLM. On its own, the SLM pixel pitch is too large for useful tuning to be obtained. For 1.55μm telecommunications WDM use, a wavelength filter needs to discriminate between different wavelengths separated by about 0.8nm. This would require a pixel pitch of about 5μm, which is to small for current SLM technology. However, by introducing a fixed grating of that order of spatial periodicity, then the light is sufficiently angularly spread to allow a tuning resolution of about 0.8nm. The SLM operates now only to slightly change the angle of diffraction of the light, so allowing fine tuning. Figure (4.2) shows the concept of using a relatively coarse SLM in conjunction with a highly dispersive fixed grating to achieve high resolution tuning. The
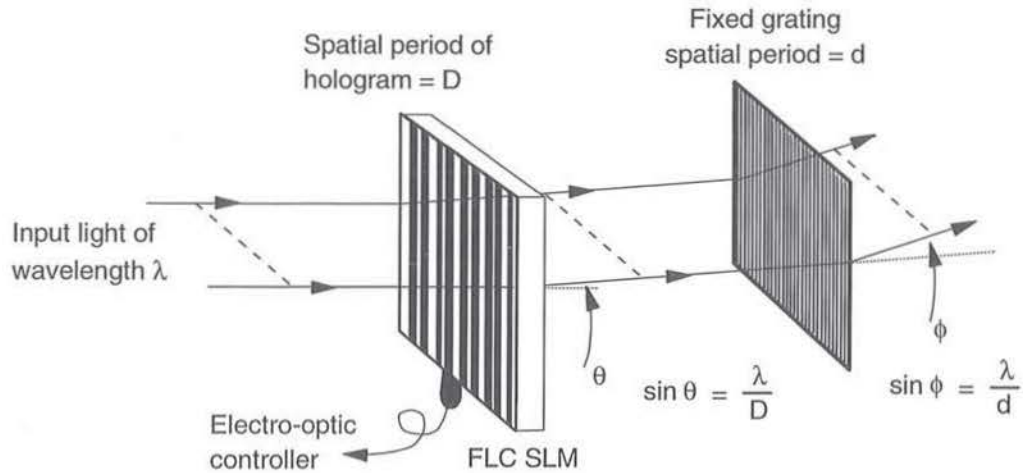
Figure 4.2: High resolution tunable wavelength filter using SLM and a fixed grating

light is diffracted through a total angle of $\theta + \phi$, where the first angle θ is variable and allows the fine tuning. The angle $\phi \gg \theta$ due to the fixed grating is a constant. The physical order of the two diffractive elements can also be reversed.

4.3 Proof-of-Principle Experiment

4.3.1 Experimental Architecture

The first proof-of-principle demonstration of the holographic optically transparent digitally tunable wavelength filter was performed using a reflective, folded back architecture[101]. The filter is shown in figure (4.3). This is a similar architecture to the Littrow configuration, except that the input and output fibres are in different spatial positions. Light from a single-moded telecommunication fibre (core diameter $\phi_{core} \approx 9\mu m$) was collimated by a lens (focal length $f = 76.2mm$) placed on-axis to the fibre. The collimated light was passed through a polarisation-sensitive SLM[1] displaying a suitable hologram. Since the SLM was a binary device using bistable FLC[2], the resulting binary-phase hologram diffracted the light in a symmetrical manner, so that symmetric negative orders always accompanied the positive diffracted orders. This meant that more than half the light was automatically lost, since the light was diffracted though two angles $\pm\theta$. Using the grating equation (4.1), the angle θ is closely given by:

$$\theta \approx \frac{n\lambda}{ND} \qquad (4.2)$$

---

[1]Crossed polarisers were placed either side of the SLM to give π binary-phase operation, and to cut out the zero-order, undiffracted light. This made the SLM polarisation-sensitive.

[2]See §2.2 for a description of its characterisation.
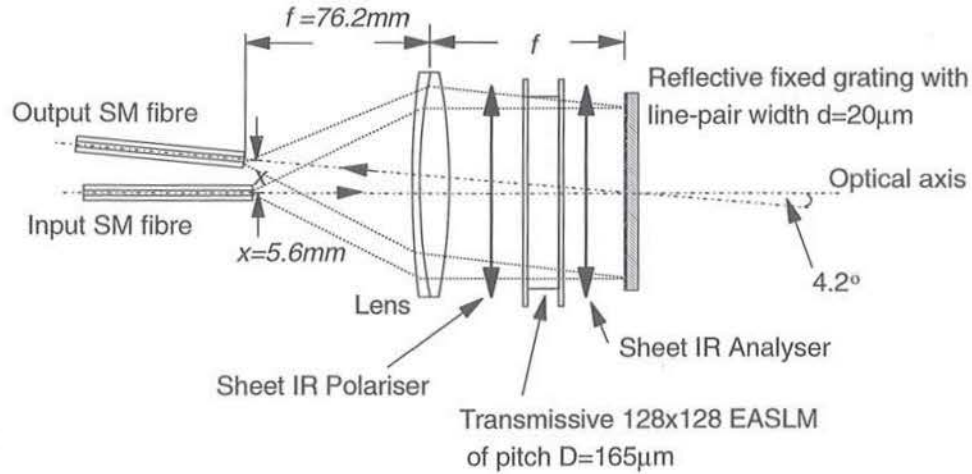
Figure 4.3: Polarisation-sensitive 2.5nm resolution wavelength filter

where $N = 128$ is the number of pixels along one side of the SLM, $D = 165\mu$m is the pixel pitch and n is an integer in the range $0 \rightarrow \frac{N}{2}$. The quantity $\frac{n}{ND}$ can be considered as the effective spatial frequency of the hologram displayed on the SLM. The diffracted light continued onto the reflective fixed binary grating which further diffracted the light by angles $\pm\phi$, where $\phi = \lambda/d$ and $d = 20\mu$m was the spatial period of the fixed grating. The reflected light passed once more through the SLM which diffracted it once again by angles $\pm\theta$. Thus the total angular deviation Φ of the light was given by $\Phi = \pm\theta \pm \phi \pm \theta$. The light passed through the lens once again which focused and coupled the light into the output SM fibre, a distance $x = 5.6$mm from the optical axis. The output angle β of the light coming out of the SLM is simply given by $\tan\beta = x/f$, so that for small β we can use the approximation $\beta \approx x/f$. But the output angle β is given by the input angle with all the angular deviations through the system added, so that $\beta = \Phi$. This yields the expression $x/f \approx \pm\theta \pm \phi \pm \theta$, which we can then rewrite as:

$$\lambda \approx \frac{x}{f\left\{\frac{1}{d} \pm \frac{n}{ND} \pm \frac{n}{ND}\right\}} \tag{4.3}$$

The two plus/minus signs in the equation tells us that there are multiple wavelengths we can couple into the output fibre. But most of them are redundant, since they lie outside the wavelength area of interest. We are just interested in those wavelengths corresponding to the positive angles, such that:

$$\lambda \approx \frac{x}{f\left\{\frac{1}{d} + \frac{2n}{ND}\right\}} \tag{4.4}$$

This corresponds to a tuning range of $\lambda_{n=64} = 1.311\mu$m to $\lambda_{n=0} = 1.470\mu$m in 64 average steps of 2.5nm.
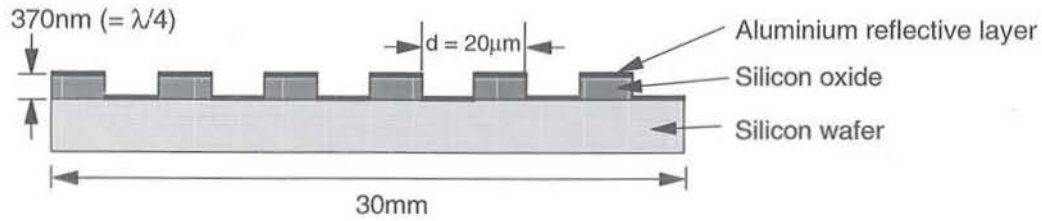
Figure 4.4: Cross-section of reflective binary-phase fixed grating

The fixed grating was made by oxidising a silicon wafer to a depth of ~ 500nm. Photoresist was spun onto the oxidised wafer and a mask used to photolithographically etch the 20μm line-pair width grating. This left a photoresist grating on top of the oxidised layer. The wafer was dipped into HF acid which etched away the exposed oxide layer to the silicon base. Acetone was used was used to wash off the photoresist, leaving a grating etched into the oxide. The grating required a depth of $\lambda_0/4 \approx 370$nm so as to be binary-phase at a wavelength of about 1480nm. This was attained by placing the whole wafer into an HF bath which continued etching the oxide grating at an estimated rate of 66.6nm/min to the required depth. The grating depth was periodically measured using a Dektak. Finally, a thin aluminium layer was vapour deposited onto the grating to give it a high reflectivity. A schematic of the grating cross-section is shown in figure (4.4).

4.3.2 Results

The digitally tunable wavelength filter was successfully used to isolate the three main lasing modes of a pump laser diode, lying between 1.446μm and 1.466μm. These modes lay conveniently within the tuning range of the filter. Figure (4.5) shows the spectrum of the laser diode overlaid with the passbands of four holographic filters, while figure (4.6) shows the three modes being successfully filtered and isolated using three of the holograms. The individual losses experienced by the three modes using holograms (a), (c) and (d) were respectively 59.0dB, 61.8dB and 57.7dB . The FWHM of the filter passband ($\approx \frac{\phi_{cored} d}{f}$) is also found to be 2.5nm, and the actual passband is assumed gaussian in shape.

4.3.3 Discussion

The holographic wavelength filter was a successful proof-of-principle demonstration of using an SLM and fixed grating to achieve high resolution tuning. Unfortunately it was polarisation-sensitive and exhibited an extremely high loss of at best 57.7dB. The high losses are accounted for in the following table:
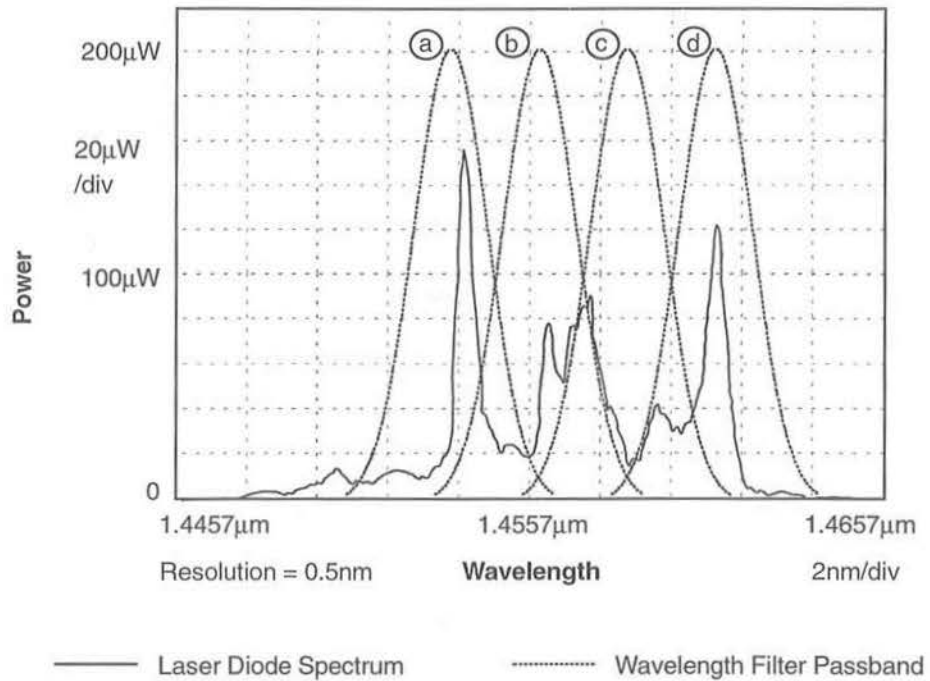
Figure 4.5: Pump laser-diode power spectrum
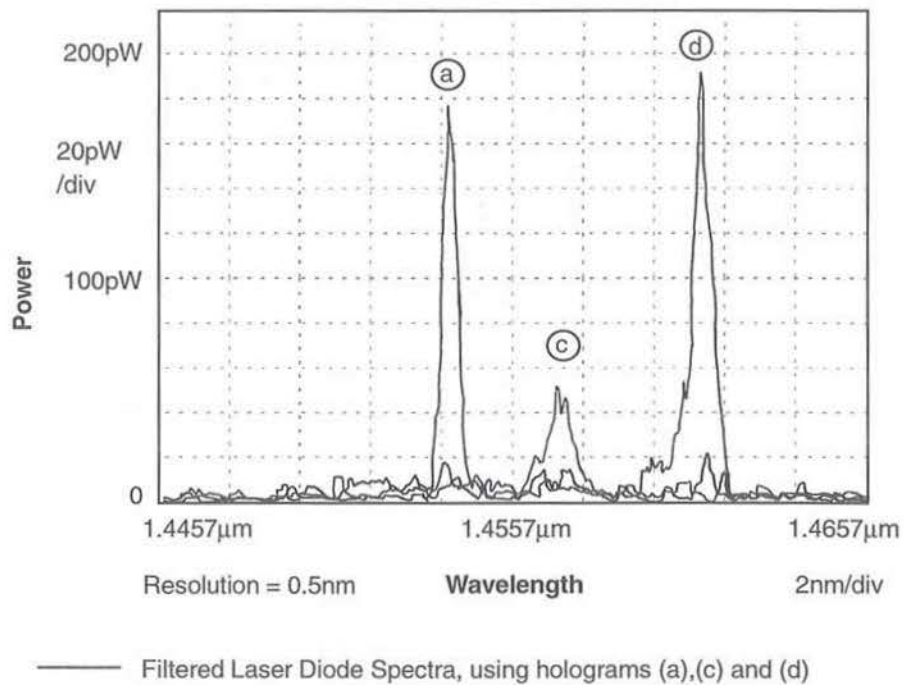
Figure 4.6: Filtered power spectrum using 3 different holograms

SLM Losses	dB
FLC Switching Angle $2\theta = 28°$, (transmission $= \sin^2 2\theta$), 2 passes	13.14
Diffraction Efficiency ($\eta = 36.5\%$), 2 passes	8.76
Fixed Grating Losses	
Diffraction Efficiency ($\eta = 36.5\%$)	4.38
Polarisation Losses	
Polariser Absorption (open transmission $= 18\%$), 2 passes	14.9
loss due to random input polarisation state of light	3.01
Sundry Losses	
18 reflecting surfaces, each contributing 4% loss	3.16
Fibre/Lens coupling efficiency ($\sim 9.2\%$)	10.35

TOTAL	**57.7**

The majority of the loss is accounted for by the polarisation-sensitivity of the filter. Fortunately it was discovered[91] that useful operation of the SLM could also be achieved without the need for polarisers. This had the advantages of making the filter polarisation-insensitive, as well as avoiding all the associated polariser losses. The double pass architecture of the filter also incurred a loss of 10.95dB, since the light was diffracted a second time by the SLM. The large angle made by the emerging light with the optical axis also lay outside the designed numerical aperture of the lens. The lens was designed to be only diffraction-limited up to 2° off-axis, but the light emerging from the filter was over 4° off-axis. This contributed to the low coupling efficiency into the output fibre of about 9.2%. The higher losses experienced by the laser modes using holograms (a) and (c) were due to the centres of the filter passbands not coinciding with the laser modes, as shown in figure (4.5).

4.4 Experimental Linear Architecture

4.4.1 Design

Using the experience gained from the proof-of-principle demonstration, a more optimised design for a holographic wavelength filter was developed. A linear architecture was adopted so as to avoid the additional losses due to a double pass through the SLM. A single pass through the SLM also allowed for finer resolution tuning, since the light was only diffracted through half the angle. A schematic of the adopted design is shown in figure (4.7), and a photograph of it is shown in figure (4.8). The filter was designed to operate at wavelengths encompassing the erbium window, making it relevant for application in a WDM telecommunications environment.

Light from a flat-cleaved single-moded 125/9μm optical telecommunications fibre (with the other end FC/PC connectorised for ease of use) was collimated by an uncoated glass
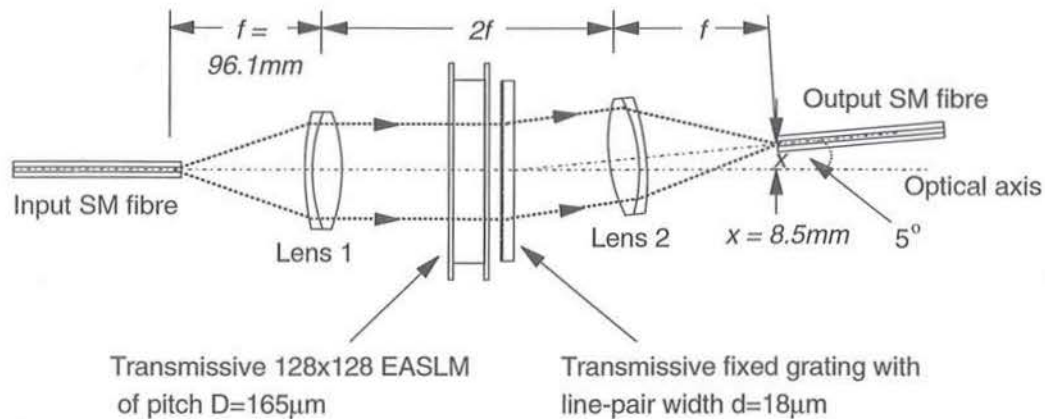
Figure 4.7: Polarisation-insensitive 1.3nm resolution wavelength filter

doublet lens[3], designed for performance in the near-infrared spectrum. It had a focal length of $f = 96.1$mm at a wavelength of $\lambda = 1.55\mu$m, and an aperture diameter $\phi = 30$mm. The electrically addressed SLM optimised for use at a wavelength of $\lambda = 1.55\mu$m was the same as used in the proof-of-principle experiment. It was a 128×128 pixellated device with a pixel pitch of $D = 165\mu$m, creating a square aperture of side $L = 21.12$mm. The diagonal length of the SLM aperture was thus 29.87mm, fitting just within the aperture of the collimating lens. The SLM was operating in its polarisation-insensitive mode[91] by removing the crossed polarisers either side of it, which meant that it operated in a binary-phase mode, but with the 2 possible phase modulations being either $0°$ or $4\theta = 56°$. Since it was not π binary-phase operation, the proportion $\cos^2 2\theta = 78\%$ of the light remained undiffracted[4]. The transmissive binary π-phase fixed grating was custom made. A round optical glass flat[5] of diameter 30mm and thickness 9mm and with a flatness of better than $\lambda/10$ across its surface was used as the grating base[6]. A layer of photoresist was spun onto the glass flat to a depth of $\lambda_o/2(n_1 - n_0) \approx 1295$nm, ($n_0$ is refractive index of air, n_1 is that of the photoresist ≈ 1.6) and then photolithography was used to selectively etch the binary-phase grating from the photoresist. The resulting fixed binary-phase grating had a line-pair width of $d = 18\mu$m, and covered an area of 30mm×30mm. A schematic of the binary-phase grating cross-section is shown in figure (4.9). The second fourier transform lens was identical to the collimating lens, so that they made a pair. It was placed at an angle of $5°$ to the optical axis to maximise the launching efficiency into the output fibre. The

[3]Manufactured by Melles-Griot, product number 06 LAI 011.

[4]See §2.3.3 for theoretical analysis.

[5]Manufactured by Comar, Cambridge.

[6]Such an optically flat (and hence relatively thick) element for the grating base is probably unnecessary, since relatively slow phase changes across the wavefront should not affect the filter performance unduly.
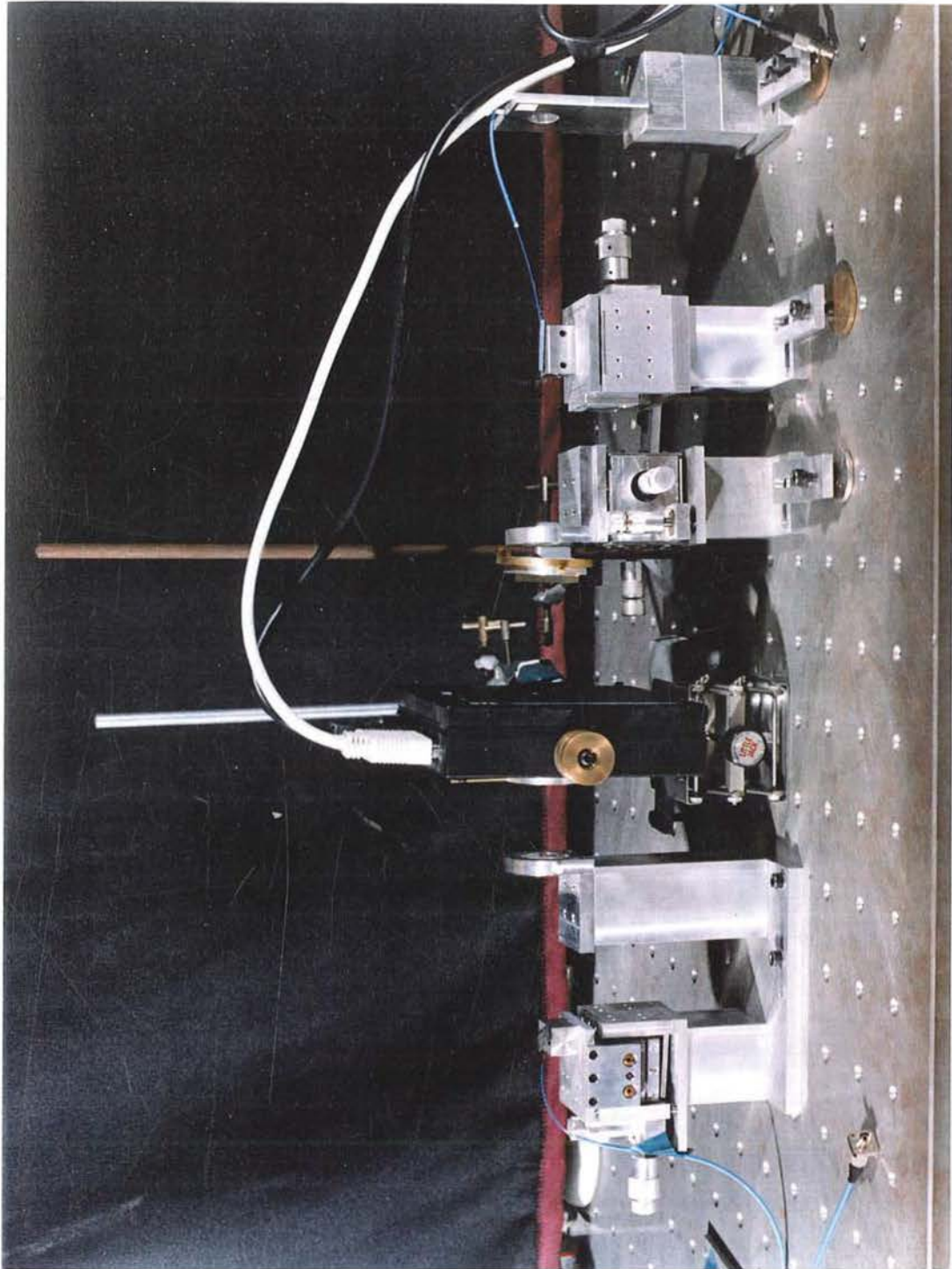
Figure 4.8: Photograph of polarisation-insensitive wavelength filter
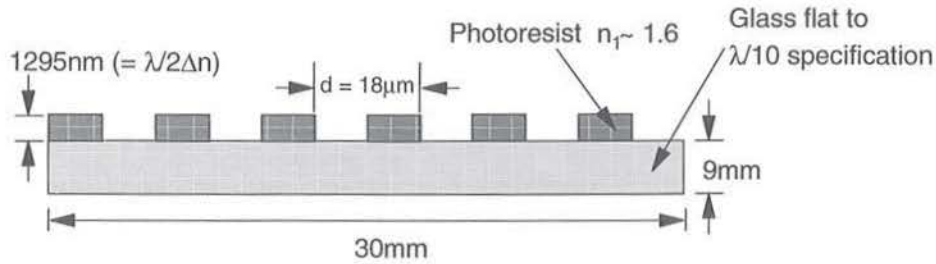
Figure 4.9: Cross-section of transmissive binary-phase fixed grating

lens could have been placed on-axis, but it was only diffraction limited up to 2.5° off-axis, and so the coupling efficiency would have been lower. The output fibre was another flat-cleaved single-moded $125/9\mu$m telecommunications optical fibre with the far end FC/PC connectorised, placed a distance $x = 8.5$mm from the optical axis, so as to spatially filter only one diffracted order.

4.4.2 Theoretical Performance

The polychromatic light from the input fibre was collimated by the first lens and passed through the SLM. A hologram displayed on the SLM diffracted the light through an angle θ given by $\theta \approx \frac{n\lambda}{ND}$ where λ is the wavelength, $D = 165\mu$m is the pixel pitch, $N = 128$ is the number of independent pixels on the hologram, and n is an integer lying between 0 and $N/2 = 64$. The quantity $\frac{ND}{n}$ is the fundamental spatial period of the displayed hologram. The light was further diffracted through an angle ϕ by the fixed grating where $\phi \approx \lambda/d$, and $d = 18\mu$m is the grating line-pair width. The fourier transform lens converted the angular dispersion of the light into a spatial separation x, such that $x \approx f(\theta + \phi)$. Thus the equation governing the central wavelength to be coupled back into the second fibre is given to a close approximation by:

$$\lambda \approx \frac{x}{f\left(\frac{n}{ND} + \frac{1}{d}\right)} \qquad (4.5)$$

The digital holographic filter was theoretically tunable between $\lambda_{n=64} = 1509.7$nm and $\lambda_{n=0} = 1592.1$nm, giving a theoretical range of 82.4nm in average discrete steps of about $\Delta\lambda = 1.29$nm. The change of wavelength step $\Delta\lambda$ with the hologram parameter n is linear to within about $\pm5\%$ over the whole range. The theoretical 3dB-bandpass width $\Delta\lambda_{FWHM}$ of the filter is calculated using the following equation relating the coupling efficiency of light which is an off-axis distance x from the fibre axis. This is derived using the gaussian approximation for fibre wave-guide modes, and free-space light modes[124]:

$$\eta = \frac{4\beta^2}{(1 + \beta^2)^2} e^{-\frac{2x^2}{r^2(1+\beta^2)}} \qquad (4.6)$$
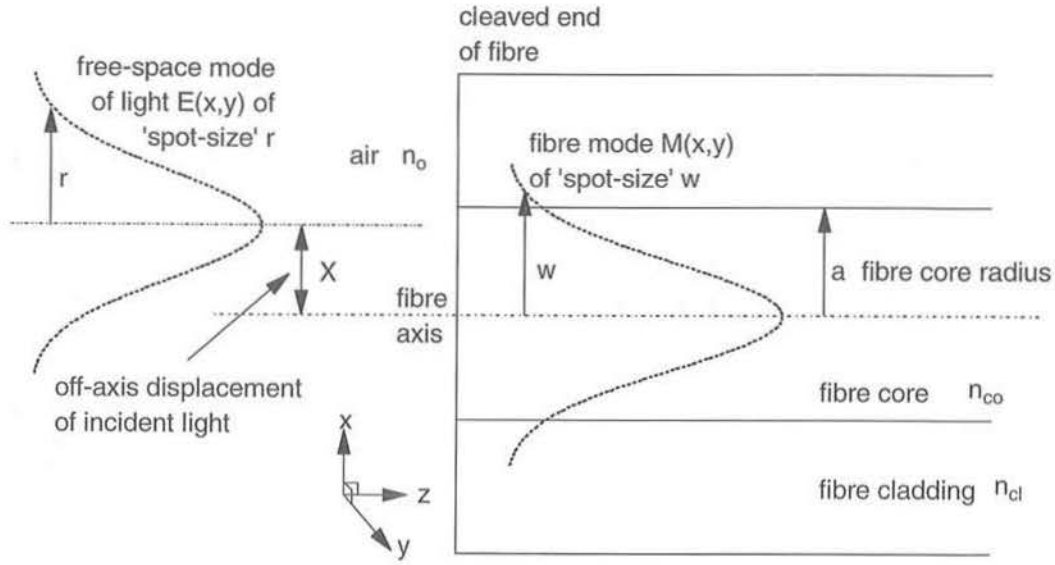
Figure 4.10: Off-axis coupling of light into a glass fibre

where $\beta = w/r$, with w being the spot radius of the fibre mode, and r is the spot radius of the free-space light mode, as shown in figure (4.10). For the $4f$ design of the filter using conjugate lenses, we can assume that $\beta = 1$. The distance for which the coupling efficiency is halved is thus $x_{\eta=50\%} = \sqrt{\ln 2}\,w$. The 3dB-passband of the filter $\Delta\lambda_{FWHM}$ is given by the range of wavelengths coupled in over the distance $2x_{\eta=50\%}$. Using equation (4.5) and assuming that $d \ll D$ we can write:

$$\Delta\lambda \approx \Delta x \frac{\partial \lambda}{\partial x}$$

$$\Delta\lambda_{FWHM} \approx 2x_{\eta=50\%}\frac{1}{f\left(\frac{n}{ND} + \frac{1}{d}\right)}$$

$$\approx \frac{2\sqrt{\ln 2}\,wd}{f} \tag{4.7}$$

Using the Marcuse[125] approximation relating the spot radius of the fibre mode w, with the fibre core radius a and the fibre V number:

$$\frac{w}{a} \approx 0.65 + \frac{1.619}{V^{3/2}} + \frac{2.879}{V^6} \tag{4.8}$$

and assuming that the fibre cut-off wavelength is about $\lambda_c \approx 1260$nm such that at $\lambda = 1.55\mu$m, $V \approx 1.96$, then the relationship between the fibre mode spot-size and core radius is $w/a \approx 1.29$. Assuming the fibre core radius $a = \phi_{core}/2 = 4.5\mu$m, then the 3dB-passband of the filter is given by:

$$\Delta\lambda_{FWHM} \approx \frac{2\sqrt{\ln 2} \times 1.29 ad}{f}$$

$$\approx 1.07\frac{\phi_{core}d}{f}$$

$$\approx 1.80\text{nm} \tag{4.9}$$

4.4.3 Results

The holographic tunable filter was used to filter the broadband amplified spontaneous emission (ASE) from an EDFA. At best, the filter exhibited a loss of 22.8dB which is 34.9dB improvement on the original loss of the first filter. The 3dB-passband width of the filter was found to be 2.0nm, which is slightly higher than the theoretical bandwidth 1.8nm. The filter passband about an arbitrary central wavelength is shown in figures (4.11) and (4.12). The hologram used for this particular filter was a regular grating with a line-pair width of 4 pixels, such that $R = 2$. Figures (4.13) and (4.14) shows 11 successive holograms filtering the spontaneous emission of an EDFA. All filters showed a FWHM of about 2.0nm, but uneven losses. The filter #8 is the same as used to record the transmission of the filter passband in figure (4.11), and so was a regular grating. The other holograms however were not regular gratings, which meant that their diffraction efficiencies were reduced due to the effects of the overlaying sinc envelope, resulting in lower transmissions. From §3.3.5 we can calculate the expected reduction in diffraction efficiencies due to the sinc envelope. Since filter #8 is a regular hologram with $R = 2$ pixels per half-period, then the relative position of its 'spot' in the output plane is $x_p = \frac{f\lambda}{4W}$, or at the midpoint of the first-order. From equation (3.24) the value of the multiplying sinc envelope at this position is $\text{sinc}^2\pi/4 = 0.81$. Thus either side of the filter due to the grating, we should expect to see the transmissions of the hologram filters reduced to about 81%. This is what we observe in figure (4.14), even having taken into account the varying power of the ASE spectrum of the EDFA.

4.4.4 Discussion

From figure (4.12), we see that the transmission profile is very close to gaussian, since on logarithmic scales, it is very close to parabolic in shape. But greater than about 3nm either side of the central wavelength, we depart from gaussian behaviour. This is to be expected, since the actual shape should be a Bessel function, which converges to zero slower than a gaussian, and so has larger 'tails' as illustrated in the diagram. From §3.3.4 the SNR of the filter should be about 28.1dB [7]. The diagram shows that the filter has an SNR > 30dB, since the tails are still falling at −53dB, and have not flattened out. However, the theoretical SNR is only reached for wavelengths greater than 10nm away from the central wavelength, due to the convolution arising from the gaussian coupling efficiency into the fibre end. In WDM systems, wavelength spacing is of the order of 1 to 4nm [126] and for this holographic filter an isolation of about 20dB is achieved about 3nm away from the central wavelength.

---

[7]From equation (3.23) we have $\text{SNR} = \frac{N}{R^2 \sin^2\frac{\pi}{2R} - 4\alpha}$, so that for $R = 2$, $N = 128$ then $\text{SNR} = 28.1\text{dB}$.
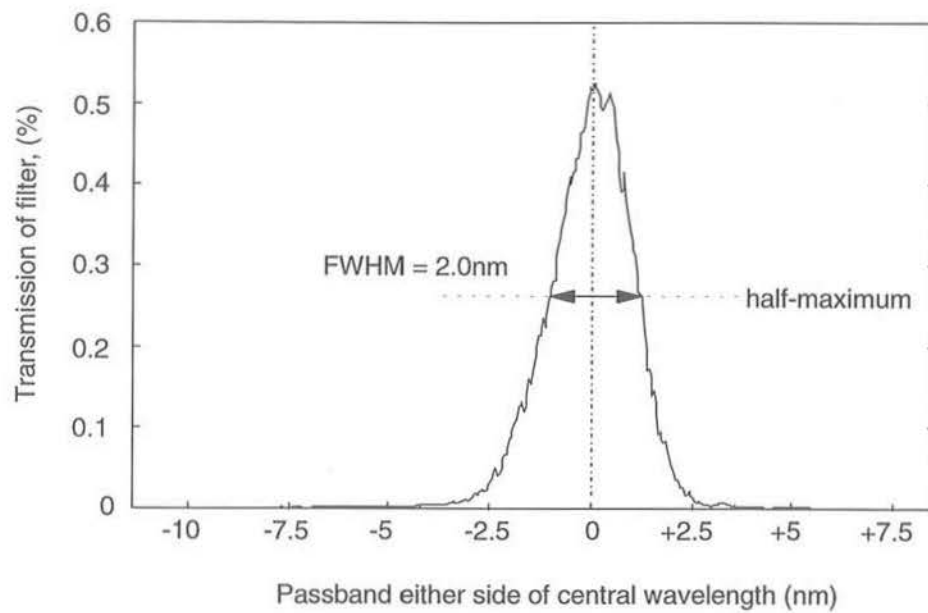
Figure 4.11: Linear plot of filter passband with FWHM=2.0nm
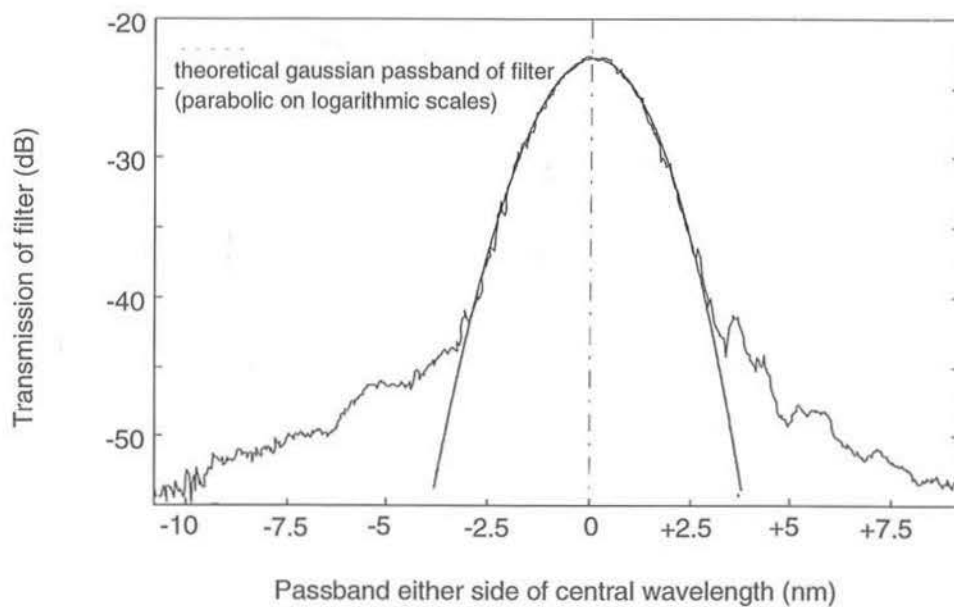
Figure 4.12: Logarithmic plot of filter passband

59
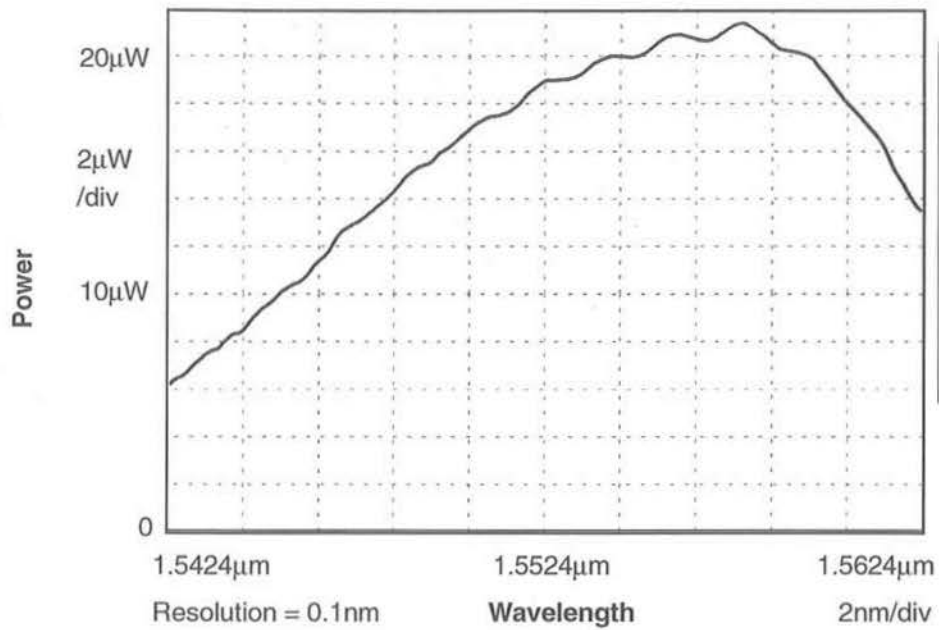
Figure 4.13: Amplified spontaneous emission from EDFA
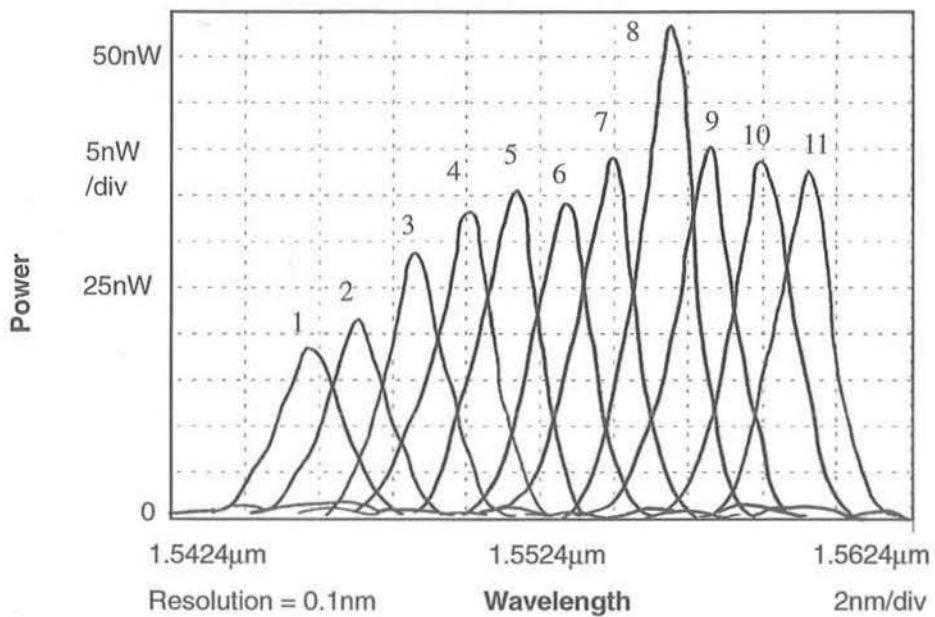
Figure 4.14: Filtered ASE using 11 different holograms

The 22.8dB loss of the filter, which is still high, is accounted for in the following table:

SLM Losses	dB
FLC switching angle $2\theta = 28°$, (transmission = $\sin^2 2\theta$),	6.57
Diffraction efficiency ($\eta = 36.5\%$),	4.38
Aperturing of SLM	0.79
Fixed Grating Losses	
Diffraction efficiency ($\eta = 36.5\%$)	4.38
Phase depth only 168°	0.05
Sundry Losses	
10 reflecting surfaces, each contributing 4% loss	1.77
FC/PC patchcords uniter losses (×2)	1.14
Fibre/lens coupling efficiency ($\sim 42\%$)	3.72
TOTAL	**22.8**

The filter losses can be reduced substantially by using a high tilt angle FLC such that $2\theta = 90°$, an SLM with a larger aperture, a blazed fixed diffraction grating or refractive prism so that the fixed wavelength dispersive element only diffracts the light into one order, anti-reflection coatings on the optical elements and fusion splicings where appropriate. A diffraction efficiency loss of 4.38dB is unavoidable for a SLM using bistable FLC, while a fibre/lens coupling efficiency of $60\% = -2.2$dB should be possible. Thus a total filter loss of the order of 6.5dB should be possible. A continuous phase FLC, such as a nematic FLC or Smectic A* FLC will allow hologram diffraction efficiencies approaching 100%, so reducing filter losses still more, albeit with longer write times.

4.4.5   Temporal Modulation of Filtered Light

Since the FLC used in the SLM was not completely bistable, it required periodic refreshing via the application of a 12kHz a.c. voltage, in order to maintain its state. In addition, the SLM pixels were addressed in an interlaced time-multiplexed manner, so that alternate rows of the SLM were written to. This periodic refreshing of the pixels meant that any signal passing through the holographic filter was amplitude modulated. The effect of this can be seen in §5.3.4 where the FLC SLM caused modulation of the tunable fibre laser output. This modulation of the signal passing though the FLC SLM is obviously undesirable, but will be cured by a totally bistable FLC, which does not require periodic refreshing. In the experiment, the modulation was minimised by rotating the SLM display by 90°, so that when each row of the display was updated, rather than a whole unique line of the hologram being momentarily non-functional (and thus corrupting the whole hologram), only a line *across* the hologram structure became momentarily disabled, leaving most of the diffractive

pattern of the hologram intact, so that it was still mostly effective. The rotated SLM can be seen in the photograph of figure (4.8), where it needed to be held in place by a retort stand and supported on an adjustable jack, rather than be held in place by the designed base.

4.4.6 Multiple Wavelength Filtering

The hologram displayed on the SLM can also be designed so that multiple wavelengths are simultaneously filtered. This is achieved by designing a hologram with multiple spatial periods. This is one of the interesting and significant properties of holographic tuning. Although AOTFs [11] are able to do this in a similarly reconfigurable manner, they suffer from significant crosstalk. A hologram was designed to filter two wavelengths simultaneously at 1555nm and 1561.5nm. The resulting filter dual wavelength passband is shown in figures (4.15) and (4.16). The dip in the transmission at the centre of the second passband band is probably due to the SLM refreshing at the instant in time when the spectrum analyser was measuring the transmission at that wavelength. The hologram was designed to have equal passband transmissions at the two wavelengths, but system imperfections have caused the two passbands to become unequal. At best, holograms would be designed and calculated *in-situ*, so that system irregularities are automatically taken into account and compensated for. The figures demonstrate that the transmissions at the pass wavelengths are reduced by an average of 5dB and the SNR reduced to at best 17dB when 2 wavelengths are filtered. This is as expected from the analysis given in §3.3.4, which predicts that the total diffraction efficiency should decrease by about 3dB[8] and the transmission by a further 3dB since there are 2 passbands into which to divide the light, so as to make a total theoretical reduction of 6dB in the transmission efficiency. The analysis of §3.3.4 also predicts that the SNR should be greater than 13.1dB[9]. Multiple-phase holograms should be able to achieve such multiple wavelength filtering with a greater efficiency and SNR.

4.5 Conclusions

Successful polarisation-insensitive holographic wavelength filtering using a combination of dynamic holograms written onto an SLM in conjunction with a fixed grating has been demonstrated. A high resolution of up to 1.3nm has been achieved, with filtering over a range of about 80nm across the erbium window possible. Signal-to-noise ratios of greater than 30dB have been achieved and simultaneous filtering of multiple wavelengths has also been demonstrated. The results demonstrate that holographic tunable wavelength filtering has the potential to become an important technology in WDM telecommunications systems.

---

[8]From equation(3.18) we find that the transmission should decrease by a factor $pF^2(p) = 0.5$, for $p = 2$.

[9]From equation (3.22) we have SNR $> \frac{4F^2(p)N}{\pi^2 - 16\alpha pF^2(p)}$, so that for $p = 2$, $N = 128$ then SNR> 13.1dB.
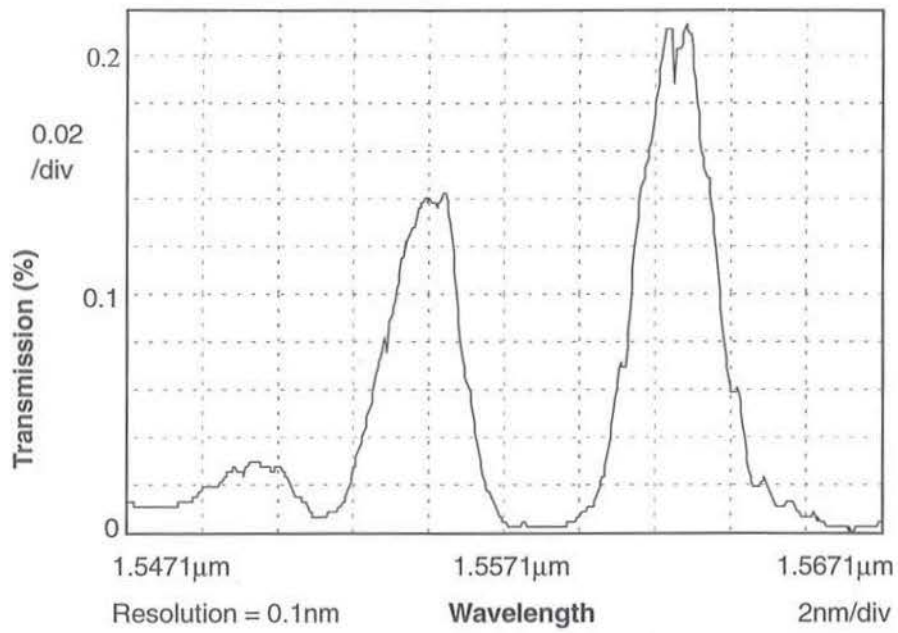
Figure 4.15: Linear plot of dual-wavelength filter passbands
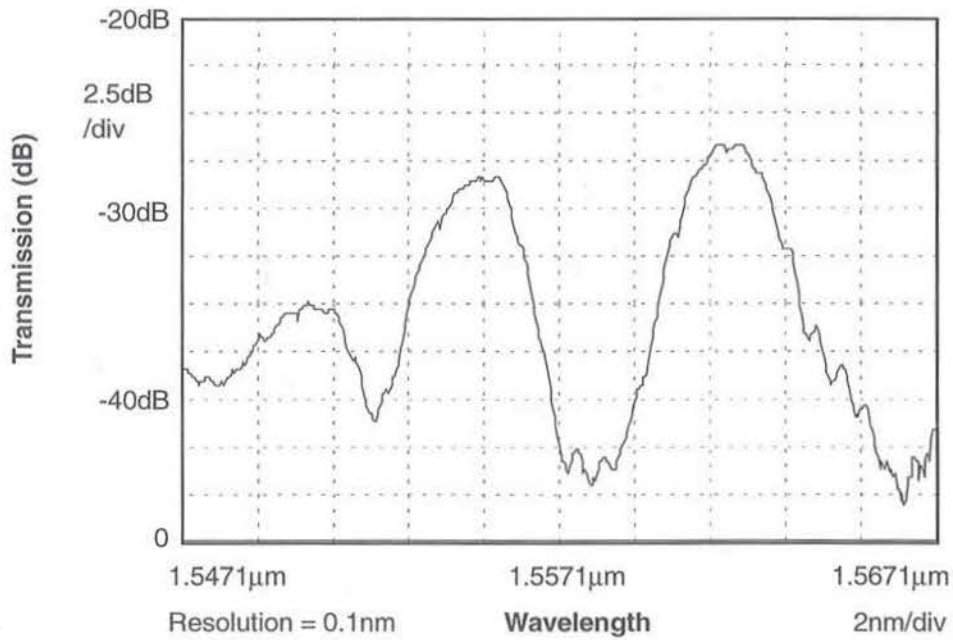
Figure 4.16: Logarithmic plot of multiple wavelength filtering

4.6   Holographic Wavelength Filter Design

4.6.1   Design Specifications

The two holographic wavelength filters described above have been physically relatively large, and with a resolution of at best 1.3nm. A practical, commercial holographic filter will have to be much more compact and also attain a higher resolution. Of interest is to determine the minimum possible size of the holographic wavelength filter, for a given resolution. Reducing the physical size of the filter has the additional advantages of increased portability, stability and will require smaller sized optical elements. There are two generic architectures which need to be considered:

- **Linear 4f architecture** using a transmission SLM and transmissive fixed grating

- **Folded 2f architecture** employing either

    i) a transmissive SLM and reflective fixed grating, in a Littrow configuration

    ii) a reflective SLM (*e.g.* silicon backplane or phase-doubled) and transmissive fixed grating

The proof-of-principle holographic filter of §4.3 is an example of a folded architecture with a transmissive SLM and reflective grating, while the second experimental holographic filter of §4.4 is an example of a linear architecture. There are two fundamental parameters which determine the physical size of the filter: the focal length f of the lens or lenses used, and the aperture dimension ND of the SLM given by the product of the individual pixel pitch D and the number of pixels N along one side of the SLM. A linear architecture filter will have a volume of the order of $4f \times (ND)^2$, whereas a folded architecture will have a volume of $2f \times (ND)^2$, assuming the SLM has a square aperture. For the purposes of the analysis, we shall assume that current specifications[10] for a tunable filter for use in a WDM telecommunications system require:

1. Tuning with a stepping resolution of < 0.8nm

2. Passband-width of filter < 0.8nm

Coherent telecommunications systems will require tighter tolerances than these, but they are sufficient for direct detection schemes. The specification for the passband-width can be relaxed if the filter is being used to tune a laser since the laser linewidth will automatically narrow to a high degree. The analysis shows that there is an inverse relationship between the physical size and resolution of the filter. A filter with a fine resolution has to be physically

---

[10]Current ITU standards recommend WDM channel spacings of 100GHz, which corresponds to about 0.8nm channel spacings across the erbium window.
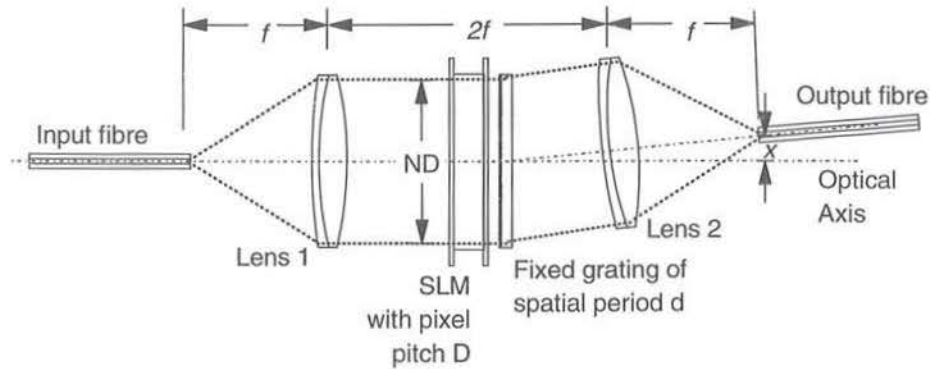
Figure 4.17: Wavelength filter with a linear architecture

larger than a filter with a low resolution. In addition we find that the size of the filter is proportional to the pitch d of the fixed grating used.

All the following calculations are performed at the standard erbium wavelength of $\lambda_o = 1.55\mu$m, and we assume that this wavelength is situated in the middle of the tuning range of the filter. Since the tuning parameter n varies from 0 to $N/2$, then $n = N/4$ for $\lambda = \lambda_o$. The spatial pitch d of the fixed grating has to be greater than λ_o for diffraction to occur effectively and to avoid undesired polarisation effects. As the phasefront is deviated through large angles of diffraction, the spot size of the light is also reduced, which reduces the coupling efficiency into the output SM fibre, according to equation (4.6). As a compromise to these various effects, an arbitrary condition we shall use in the following analyses is that $d > 1.5\lambda_o$, (*i.e.* $d > 2.33\mu$m). The diffraction angle Φ is given by $\sin\Phi = \lambda_o/d$, and the spot-size is reduced by $\cos\Phi$. For this minimum value of $d = 1.5\lambda_o$, the spot-size is reduced to 75% of its optimum value, which limits the maximum output SM fibre coupling efficiency to 92%. The desired resolution $\mathcal{R}$ of the filter is given by $\mathcal{R} = 0.8$nm.

4.6.2 Linear Architecture

A schematic diagram of the generic linear architecture for a wavelength filter is shown in figure (4.17). The equation which describes the central wavelength to couple back into the output fibre can be deduced from the diffraction angles in the system, similar to §4.4.2:

$$\tan^{-1}\left(\frac{x}{f}\right) = \sin^{-1}\left(\frac{\lambda}{d}\right) + \sin^{-1}\left(\frac{n\lambda}{ND}\right) \tag{4.10}$$

A fully linearised and rearranged version of this expression is used in equation (4.5), where the angles can be considered small. Reducing the spatial pitch d of the fixed grating causes the angular diffraction to become larger, and full linearisation is no longer possible. However, the angle deviation $n\lambda/ND$ due to the SLM does stay small, so allowing a simplification

65

to the above equation:

$$\tan^{-1}\left(\frac{x}{f}\right) \simeq \sin^{-1}\left(\frac{\lambda}{d}\right) + \frac{n\lambda}{ND} \tag{4.11}$$

A stepping resolution of $\mathcal{R} < 0.8$nm means that the change $\Delta\lambda$ in tuned wavelength must be < 0.8nm for a change in n of one ($i.e.$ $\Delta n = 1$). Differentiating equation (4.11) with respect to n and evaluating it at $\lambda = \lambda_o$ gives the condition:

$$\frac{\Delta\lambda}{\Delta n} \simeq \left.\frac{\partial\lambda}{\partial n}\right|_{\lambda=\lambda_o} = \frac{\lambda_o}{ND\left\{\frac{1}{d\sqrt{1-\lambda_o^2/d^2}} - \frac{1}{4D}\right\}} < \mathcal{R} \tag{4.12}$$

If we assume that the SLM pixel pitch is much larger than the fixed grating pitch ($i.e.$ $4D >> d$, and d is minimised to $1.5\lambda_o$), we can make a close approximation to equation (4.12) and use it to give us the minimum allowable SLM aperture:

$$ND > \frac{\lambda_o d}{\mathcal{R}}\sqrt{1 - \lambda_o^2/d^2}$$
$$\Rightarrow ND > 3.36\text{mm} \tag{4.13}$$

Of interest to note, is that as $d \to \lambda_o$, then the minimum allowable SLM aperture suddenly becomes vanishingly small. This is because the angular wavelength-dispersion of the light suddenly starts becoming large. However, this is at the expense of a very distorted spot-size.

The filter 3dB-passband width is determined by the output fibre which couples in a range of incident wavelengths across the finite width of its cleaved face. Light is coupled back into the fibre with a gaussian-shaped variation in efficiency. Wavelengths incident on the fibre at the centre of its core are coupled in with a high efficiency, whereas those wavelengths incident at the edge of the core are coupled in with a low efficiency. This defines the pass bandwidth of the wavelength filter. The analysis of §4.4.2 shows that the 3dB-passband width is given to a close approximation by the wavelengths coupled in across the fibre core diameter ϕ_{core}. Using equation (4.11), the spread of coupled wavelengths $\Delta\lambda_{BW}$ (which we want to be less than 0.8nm) due to the spatial filtering of the fibre can be expressed as:

$$\Delta\lambda_{BW} \simeq \Delta x \left.\frac{\partial\lambda}{\partial x}\right|_{\lambda=\lambda_o}$$
$$\Delta\lambda_{BW} \simeq \frac{\Delta x}{f\sec^2\left(\sin^{-1}\frac{\lambda}{d} + \frac{n\lambda}{ND}\right)\left\{\frac{n}{ND} - \frac{1}{d\sqrt{1-\lambda^2/d^2}}\right\}} < \mathcal{R} \tag{4.14}$$

Assuming again that $4D >> d$, where d is again minimised to $1.5\lambda_o$ and that the 3dB-passband width is given by the wavelengths collected across the fibre-core of diameter $\Delta x = \phi_{core} = 9\mu$m, then equation (4.14) can be closely approximated and used to yield the result that the lens focal length f has a minimum value given by:

$$f > \frac{\phi_{core}d}{\mathcal{R}}\left(1 - \frac{\lambda_o^2}{d^2}\right)^{\frac{3}{2}}$$
$$\Rightarrow f > 10.8\text{mm} \tag{4.15}$$
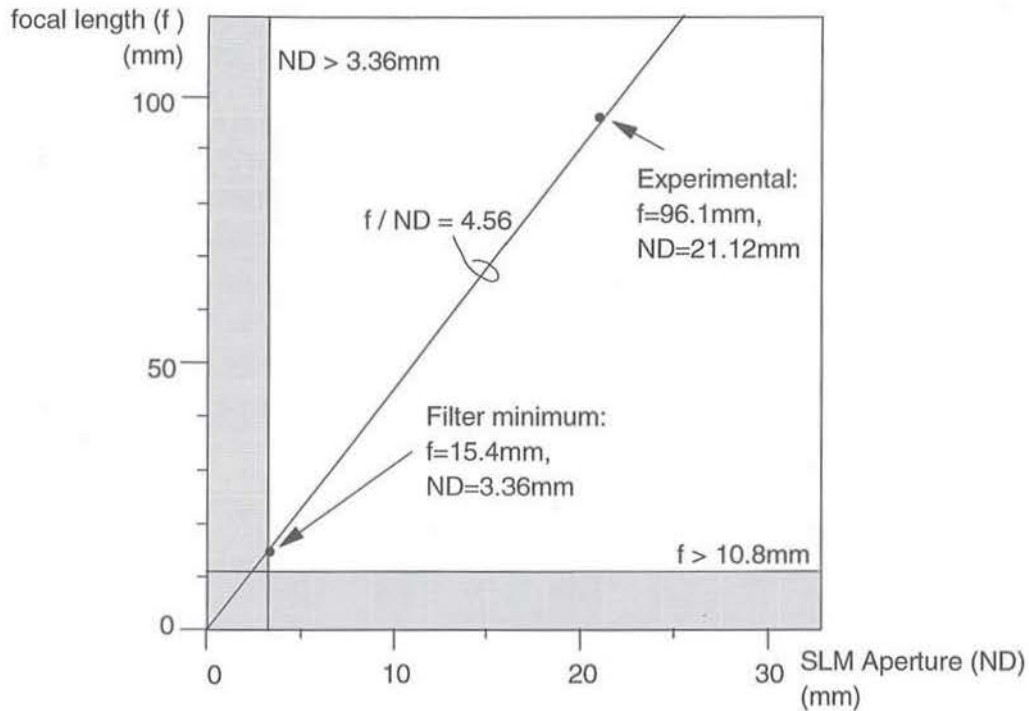
Figure 4.18: Minimum dimensions for a 0.8nm resolution filter with linear architecture

Once again, it is interesting to note that as $d \rightarrow \lambda_o$, then the minimum allowable focal length suddenly becomes vanishingly small.

We want the collimated light passing through the SLM to illuminate the aperture of the SLM as much as possible. The full tuning capability of the SLM with minimum loss is accessed when this is achieved. Since the collimated light is gaussian in intensity distribution, we want the $1/e^2$ width of the beam to coincide with the SLM aperture. From simple consideration of gaussian optics we require:

$$\frac{\lambda_o f}{\pi \phi_{core}/2} = \frac{ND}{2}$$
$$\frac{f}{ND} = \frac{\pi \phi_{core}}{4\lambda_o}$$
$$\Rightarrow \frac{f}{ND} = 4.56 \tag{4.16}$$

The three conditions given by equations (4.13),(4.15) and (4.16) are plotted in figure (4.18), which shows graphically how the dimensions of f and ND may vary with each other.

For use as a WDM demultiplexer all three conditions shown in the figure must be fulfilled, so that the minimum SLM aperture must be $ND = 3.36$mm. For this case, the focal length of the system is $f = 15.4$mm, larger than the minimum, but necessary for efficient use of the available light. The displacement x of the output fibre is $x = 13.8$mm (

67
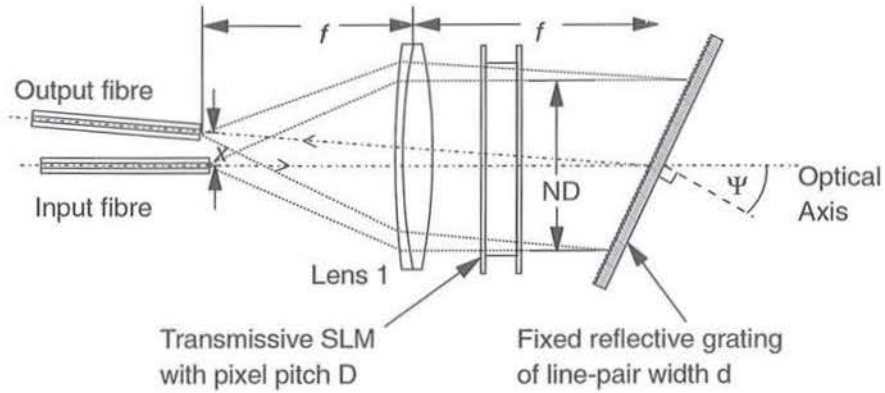
Figure 4.19: Reflective holographic filter in Littrow configuration

i.e. wider than the SLM aperture.) Thus the minimum dimensions of the filter are 61.6mm × 15.5mm ($= x + \frac{ND}{2}$) × 3.36mm.

4.6.3   Folded Architecture

A folded reflective architecture is attractive since it requires fewer components and would appear to have the potential for greater compactness. A reflective architecture can be divided into two distinct classes, as outlined earlier. The first one, similar to a Littrow configuration is shown in figure (4.19). Its main disadvantage is that it requires two passes through the SLM. This increases the loss by at least 4.38dB, for a binary-phase device, and also worsens the stepping resolution by a factor of two, since the light is diffracted thought twice the angle. Thus an SLM of twice the aperture is needed to improve the stepping resolution to the required value. However, it has the advantage of lowering the off-axis angle of the diffracted light through the lens, avoiding potential numerical aperture problems, so enabling closer diffraction-limited performance. A full analysis is unnecessary, but the basic equation describing its wavelength filtering is given below, where Ψ is the angle which the fixed grating makes with the optical axis:

$$\tan^{-1}\left(\frac{x}{f}\right) \simeq \sin^{-1}\left(\frac{\lambda}{d}\right) - \Psi + \frac{2n\lambda}{ND} \qquad (4.17)$$

This yields the result that the SLM aperture has a minimum size given by $ND > 6.76$mm, *i.e.* double the size compared with the linear case. The minimum focal length has the same minimum given by $f > 10.8$mm, but since the ratio of f to ND must be $f/ND = 4.56$, the focal length needs to be $f = 30.8$mm. This means that the minimum dimensions of the filter are 61.6mm × 6.76mm × 6.76mm. This is basically the same as for the linear architecture case.
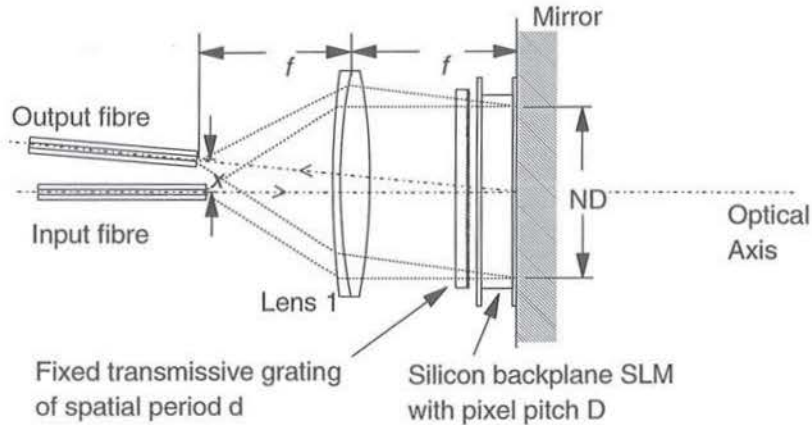
Figure 4.20: Wavelength filter with a folded architecture

The second reflective architecture utilising a reflective SLM and transmissive fixed grating is shown in figure (4.20). Since there is only a single pass through the SLM, it has a lower loss, and higher resolution. But it has the main disadvantage of the high off-axis angle through the lens. The equation which determines the filtered wavelength is approximately given by:

$$\tan^{-1}\left(\frac{x}{f}\right) \simeq 2\sin^{-1}\left(\frac{\lambda}{d}\right) + \frac{n\lambda}{ND} \tag{4.18}$$

A similar analysis as for the linear architecture is applied to place bounds on the minimum size of the system, but with the additional constraint of the numerical aperture (NA) of the lens. The NA of the system is closely given by the angle $\tan^{-1}(x/f)$ and must be less than the lens NA, which we shall assume is limited to 0.5 [127]. From equation (4.18), assuming $8D \gg d$, to a close approximation we can say that:

$$2\sin^{-1}\left(\frac{\lambda}{d}\right) + \frac{n\lambda}{ND} \; < \; 0.5$$
$$d \; > \; \frac{\lambda_o}{\sin 0.25}$$
$$\Rightarrow d \; > \; 6.27\mu\text{m} \tag{4.19}$$

Thus the spatial period of the fixed grating must be greater than for the linear architecture. The minimum SLM aperture ND is also greater since it is roughly proportional to d and is found in the same way as for the linear architecture:

$$ND \; > \; \frac{\lambda_o d}{2\mathcal{R}}\sqrt{1 - \lambda_o^2/d^2}$$
$$\Rightarrow ND \; > \; 5.89\text{mm} \tag{4.20}$$

Likewise, the minimum lens focal length f is calculated from the maximum pass-bandwidth
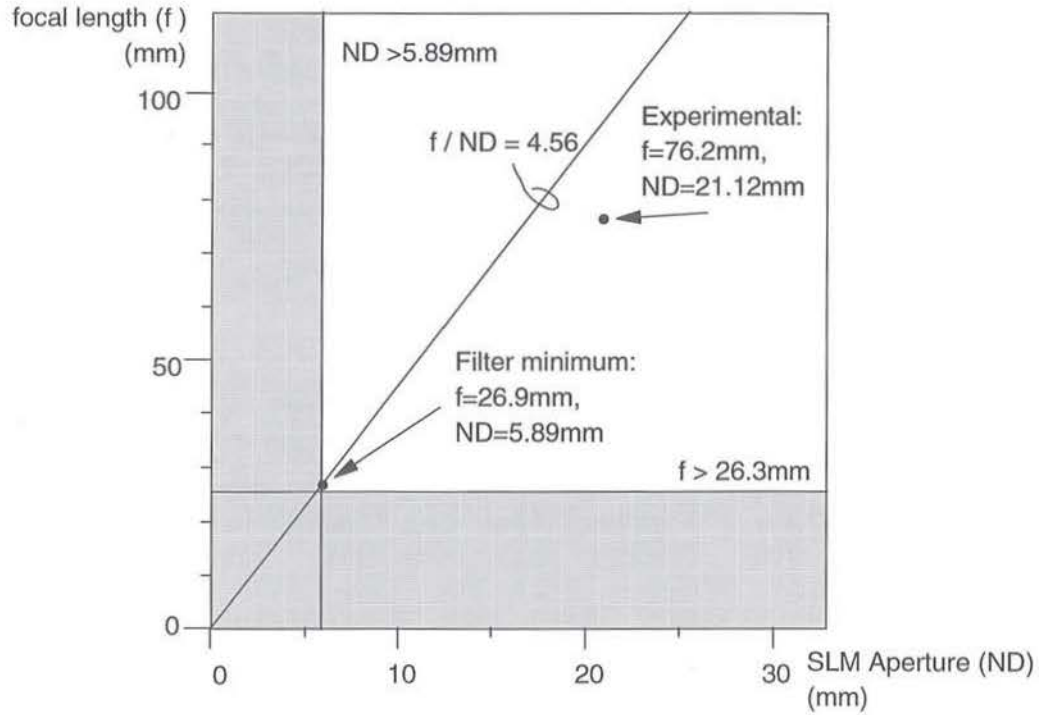
Figure 4.21: Minimum dimensions for a 0.8nm resolution filter with folded architecture

of the filter, and using equation (4.18):

$$\Delta\lambda_{BW} \simeq \Delta x \left.\frac{\partial\lambda}{\partial x}\right|_{\lambda=\lambda_o}$$

$$\Delta\lambda_{BW} \simeq \frac{\Delta x}{f\sec^2\left(2\sin^{-1}\frac{\lambda}{d} + \frac{n\lambda}{ND}\right)\left\{\frac{n}{ND} - \frac{2}{d\sqrt{1-\lambda^2/d^2}}\right\}} < \mathcal{R} \qquad (4.21)$$

This can be approximated by again assuming that $8D >> d$ and putting $\Delta x = \phi_{core}$ to yield:

$$f > \frac{\phi_{core}d}{2\mathcal{R}}\left(1 - 2\frac{\lambda_o^2}{d^2}\right)^2\sqrt{1 - \frac{\lambda_o^2}{d^2}}$$

$$\Rightarrow f > 26.3\text{mm} \qquad (4.22)$$

To illuminate the SLM as much as possible we have the same gaussian optics requirement:

$$\frac{\lambda_o f}{\pi\phi_{core}/2} = \frac{ND}{2}$$

$$\Rightarrow \frac{f}{ND} = 4.56 \qquad (4.23)$$

The three conditions given by equations (4.20), (4.22) and (4.23) are plotted in figure (4.21) which shows graphically how the dimensions of f and ND may vary with each other.

70
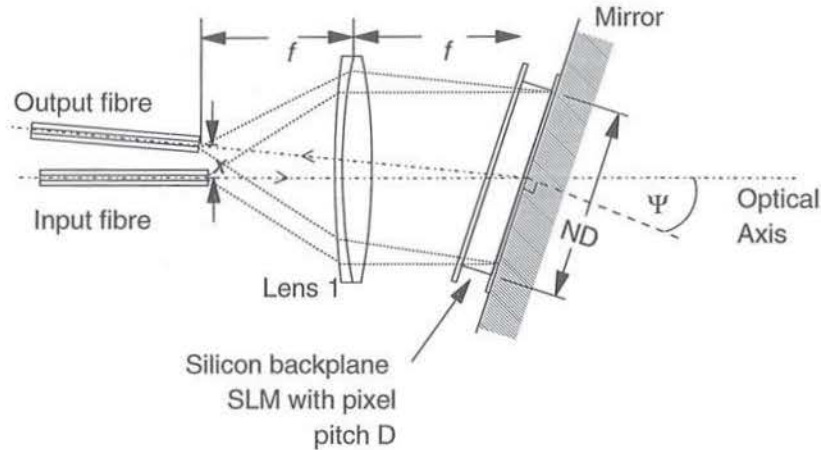
Figure 4.22: Folded architecture wavelength filter without a fixed grating

For use as a WDM demultiplexer, all three conditions must be applied, so that the SLM aperture is minimised to $ND = 5.89$mm, and the focal length of the lens must be at least $f = 26.9$mm, which is slightly longer than the minimum. The displacement of the output fibre is $x = 14.7$mm. Thus the minimum dimensions of the filter are 53.8mm × 17.6mm × 5.89mm. This is smaller than any of the other architectures with a fixed grating.

4.6.4 Architectures Without a Fixed Grating

The technology of SLMs in the future may reach the point where pixels are sufficiently numerous and their size small enough that a fixed grating may be dispensed with altogether in a filter design. An interesting exercise is to calculate the minimum pixel number and pixel pitch, as well as the overall size of such a wavelength filter, if it is to have a resolution of 0.8nm. A folded architecture in the Littrow configuration employing only an SLM to diffract the light is shown in figure (4.22). The governing equation defining the wavelength to be tuned is given by:

$$\tan^{-1}\left(\frac{x}{f}\right) \simeq \sin^{-1}\left(\frac{n\lambda}{ND}\right) - \Psi \tag{4.24}$$

For the previous analyses, we assumed that the centre of the tuning range corresponded with λ_o, so that $n = N/4$ when $\lambda = \lambda_o$. But with only an SLM containing a large number of small pixels in the architecture a huge tuning range is available to us, most of which is unused. We do not necessarily have to operate at the centre of it. Instead we can operate in a section of the tuning range which gives us an optimum filter size. Hence, we now assume that the tuned wavelength $\lambda = \lambda_o$ corresponds to the tuning parameter $n = \alpha N$, where $0 < \alpha < 0.5$, such that:

$$\tan^{-1}\left(\frac{x}{f}\right) \simeq \sin^{-1}\left(\frac{\alpha\lambda_o}{D}\right) - \Psi \tag{4.25}$$

For the architectures with a fixed grating we defined $\alpha = 0.25$, so that the middle of the tuning range corresponded with λ_o, but now α is another filter parameter to be optimised. Using equations (4.24) and (4.25), the filter stepping resolution of 0.8nm is given by:

$$\left.\frac{\partial \lambda}{\partial n}\right|_{\lambda=\lambda_o} = \left.\frac{\lambda}{n}\right|_{\lambda=\lambda_o} \quad < \quad \mathcal{R}$$

$$\frac{\lambda_o}{\alpha N} \quad < \quad \mathcal{R}$$

$$\Rightarrow N \quad > \quad \frac{1938}{\alpha} \qquad (4.26)$$

Hence we need at least 3876 pixels along one side of our SLM to achieve a resolution of 0.8nm. The filter passband width $\Delta\lambda_{BW}$ which we also want to be less than 0.8nm is found by differentiating equation (4.24). We assume that the angle $\Psi \simeq \sin^{-1}(n\lambda/ND)$ such that $x \ll f$, and also that $D \gg \alpha\lambda_o$, to yield:

$$\Delta\lambda_{BW} \simeq \left. \Delta x \frac{\partial \lambda}{\partial x}\right|_{\lambda=\lambda_o}$$

$$\Delta\lambda_{BW} \simeq \Delta x \frac{ND}{fn}\sqrt{1 - \frac{\lambda_o^2\alpha^2}{D^2}} \quad < \quad \mathcal{R}$$

$$f \quad > \quad \frac{\phi_{core}}{\alpha\mathcal{R}}\sqrt{D^2 - \lambda_o^2\alpha^2}$$

$$f \quad > \quad \frac{\phi_{core}D}{\alpha\mathcal{R}}$$

$$\Rightarrow f \quad > \quad \frac{11250D}{\alpha} \qquad (4.27)$$

From the usual considerations of illuminating the SLM as fully as possible and gaussian optics, we also have the requirement:

$$\frac{f}{ND} = 4.56 \qquad (4.28)$$

For the fixed grating we had the requirement that the *line-pair* width d had to be greater than $1.5\lambda_o$, so that $d > 2.33\mu m$. The SLM pixel pitch also has to conform to the same limit, but d is equivalent to $2D$ such that:

$$D > 1.16\mu m \qquad (4.29)$$

Inspection of equations (4.26) and (4.27) tells us that we want the parameter α to be as high as possible, to keep the number of pixels N to a minimum, as well as the focal length f. If we were to design $\alpha = 0.5$, then $\lambda_o = 1550$nm would be the minimum wavelength which we could tune to. But we want to be able to tune down to at least 1520nm, in which case by considering equation (4.25) we require that $\alpha = 0.5 \times \frac{1520}{1550} = 0.49$. From equation (4.26) the minimum number of pixels now required is $N = 3955$. Equation (4.27) gives us a minimum focal length of $f = 26.6$mm and from equation (4.28) the SLM aperture must be $ND = 5.83$mm, which corresponds to a pixel pitch of $D = 1.47\mu m$. Thus the minimum

dimensions for a filter would be 53.2mm × 5.83mm × 5.83mm. Current technology and die sizes would only allow pixel sizes of $D = 15\mu$m, with approximately 1000 pixels[128]. Thus a major advance in SLM technology would be required to make this type of wavelength filter possible.

4.6.5   Summary

A summary of the minimum filter dimensions for all the analysed architectures is given below:

Holographic Wavelength Filter:

Linear Architecture   61.6mm × 15.5mm × 3.36mm = 3.21k mm^3

Folded Architecture (i) 61.6mm × 6.76mm × 6.76mm = 2.81k mm^3

Folded Architecture (ii) 53.8mm × 17.6mm × 5.89mm = 5.58k mm^3

Folded, No Grating   53.2mm × 5.83mm × 5.83mm = 1.81k mm^3

$N=3955$ $D = 1.47\mu$m

As might be expected, the architecture without a fixed grating is ultimately the smallest by volume. However, the surprising conclusion to be drawn from these results is that the addition of a fixed grating not only provides a far higher resolution than could be obtained with existing SLMs, but only marginally increases the physical size of the filter. Another counter-intuitive result is that linear architectures tend to be almost as compact as those architectures based on reflective SLMs. This is due to the numerical aperture of the lens which limits the degree to which the light can be angularly spread and still be efficiently coupled into the output fibre. Lenses with high numerical apertures will make small filters, but the lenses themselves are likely to be large, thus increasing the size of the reflective architecture again. The analysis also shows that as the fixed grating pitch d approaches λ_o, then the required focal length f and SLM aperture ND becomes vanishingly small, even for a given resolution $\mathcal{R}$. However, this is at the expense of polarisation sensitivity and other undesired side-effects, such as spot-size distortion, which may became evident under these operating conditions. But it does offer the possibility of super-small, very high resolution holographic wavelength filter architectures.

For polarisation-insensitive operation, the analysis shows that the size of an architecture is proportional to the pitch of the fixed grating d or the SLM pixel pitch D if the fixed grating is absent. Both of these pitches are limited by and must be greater than the wavelength λ_o at which the filter is operational. Thus the factor which fundamentally limits the size of the filter is the wavelength of operation. Only by operating at shorter wavelengths can these generic wavelength filter designs be further reduced in physical size.
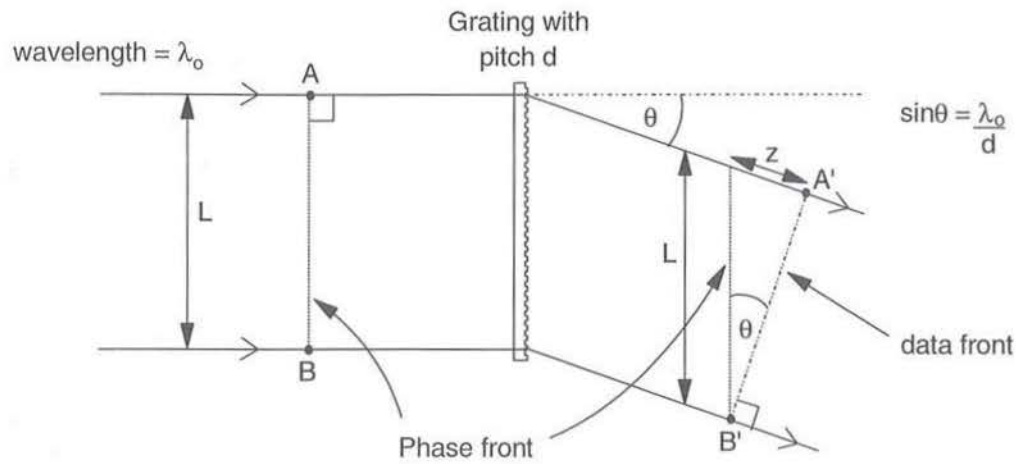
Figure 4.23: Uniform intensity light of width L incident on a grating

4.7 Temporal Dispersion of Data Stream

The fixed grating and SLM cause the direction of propagation of the incident light to be turned through an angle θ, which has the secondary effect of causing the data to become temporally dispersed due to the changed optical path lengths. This effect is equivalent to spectral broadening of the light. At high bit rates this can become a problem, since bits will start overlapping to cause inter-symbol interference, so increasing the bit error rate. A simplified analysis is initially carried out to demonstrate the basic mechanism of temporal dispersion, followed by a more rigorous analysis. The degree of spectral broadening which can be expected owing to the wavelength filter, and how it affects the maximum bit rate is analysed and calculated.

4.7.1 Simplified Analysis

Figure (4.23) shows a uniform beam of light of width L, wavelength λ_o and with a transverse wavefront incident on a grating of pitch d. The light is diffracted through an angle θ, where $\sin\theta = \lambda_o/d$. By considering the path lengths of the two rays travelling from A to A', and B to B', it can be seen that the phase front remains parallel to the grating. Before the grating, the line A-B (transverse to the direction of propagation) is parallel to the phase front. But after the grating, the line A'-B', transverse to the direction of propagation, is now at an angle θ to the phase front. The front A'-B' becomes in effect the data front, since this is the front that is coupled into the output fibre. The path difference z between A' and B' is given by:

$$z = L\sin\theta$$

74

$$= \frac{L\lambda_o}{d} \tag{4.30}$$

If the light is travelling with a velocity c, there is a temporal dispersion Δt between A$'$ and B$'$ of:

$$\Delta t = \frac{z}{c}$$
$$= \frac{L\lambda_o}{dc} \tag{4.31}$$

This means that the maximum frequency f_{max} at which the light can be modulated, before bits start overlapping each other across the data front A$'$-B$'$ is:

$$f_{max} = \frac{1}{\Delta t}$$
$$= \frac{dc}{L\lambda_o} \tag{4.32}$$

If a minimum sized, linear architecture is used for our filter then $d = 1.5\lambda_o$, $L(\equiv ND)$ =3.36mm, λ_o =1.55μm, $c = 3 \times 10^8$m/s giving us a maximum bit rate of $f_{max} = 134$Gb/s. This is not too far above current maximum bit rates, but the expression for f_{max} is due to a simplified analysis and a more rigorous analysis is required.

4.7.2 Rigorous Analysis

A more rigorous analysis to calculate the spectral broadening due to the grating needs to include the gaussian intensity distribution $I(x)$ of the light incident on the grating, and assume a data stream modulation $M(t)$ of the light. This is illustrated in figure (4.24). The gaussian intensity distribution of the light $I(x)$ is defined as:

$$I(x) = I_o e^{-\frac{2x^2}{w^2}} \tag{4.33}$$

At a point x on the data front A-B before the grating, the intensity at a time t is given by $S(x,t) = I(x)M(t)$. But after the grating we need to include the temporal dispersion $\Delta t = z/c$, so that along the data front A$'$-B$'$:

$$S'(x',t) = I'(x')M\left(t - \frac{x'\lambda_o}{\cos\theta dc}\right) \tag{4.34}$$

where x' is zero at the optical axis of the system, and the optical path difference is $z = x'\tan\theta$. The intensity distribution $I'(x')$ of the light along A$'$-B$'$ is also slightly different from $I(x)$. This is because the gaussian beam becomes narrower and more intense at its centre when it is diffracted through an angle θ, so that:

$$I'(x') = \frac{I_o}{\cos\theta}e^{-\frac{2x'^2}{w^2\cos^2\theta}} \tag{4.35}$$

The total signal power $P(t)$ along the wave front A$'$-B$'$ is given by the integration of $S'(x',t)$
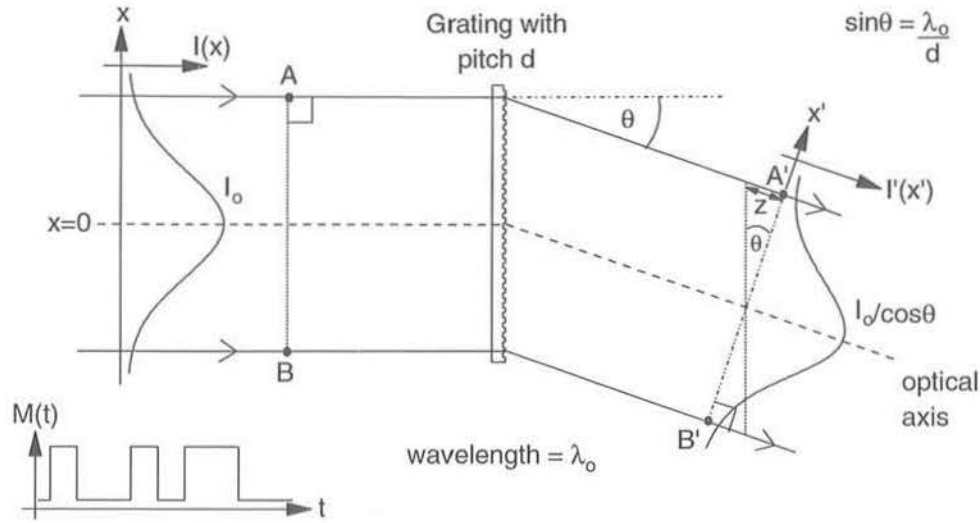
Figure 4.24: Light with a gaussian intensity distribution incident on a grating

along x':

$$P(t) = \int\limits_{-\infty}^{\infty} I'(x')M\left(t - \frac{x'\lambda_o}{\cos\theta dc}\right) dx' \qquad (4.36)$$

If we define a 'dummy' time variable τ such that $\tau = x'\lambda_o/\cos\theta dc$, which by rearranging also gives us $x' = \cos\theta dc\tau/\lambda_o$ and substitute into equation (4.36), then the total signal power becomes a time-domain convolution:

$$
\begin{aligned}
P(t) &= \frac{\cos\theta dc}{\lambda_o} \int\limits_{-\infty}^{\infty} I'(\tau)M(t-\tau)d\tau \\
&= \frac{\cos\theta dc}{\lambda_o} \int\limits_{-\infty}^{\infty} \frac{I_o}{\cos\theta} e^{-\frac{2d^2 c^2}{\lambda_o^2 w^2}\tau^2} M(t-\tau)d\tau \qquad (4.37)
\end{aligned}
$$

A convolution integral is solved easily in the frequency domain, where it simply becomes the product of the frequency spectra. Thus $p(\omega)$ is the frequency spectrum (i.e. fourier transform) of the received time-varying signal $P(t)$, such that $p(\omega) \rightleftharpoons P(t)$. We also define the following fourier transform pairs: $i'(\omega) \rightleftharpoons I'(t)$ and $m(\omega) \rightleftharpoons M(t)$, and note that the fourier transform of a gaussian is:

$$e^{-at^2} \rightleftharpoons \sqrt{\frac{\pi}{a}} e^{-\frac{\omega^2}{4a}} \qquad (4.38)$$

We can rewrite the time-domain convolution equation (4.37) as a frequency-domain product to give:

$$p(\omega) = \frac{\cos\theta dc}{\lambda_o} i'(\omega)m(\omega)$$

76

$$= \frac{dc}{\lambda_o}\sqrt{\frac{\pi}{2}}\frac{\lambda_o w I_o}{dc}e^{-\frac{\lambda_o^2 w^2}{8d^2 c^2}\omega^2}m(\omega)$$

$$= \sqrt{\frac{\pi}{2}}w I_o e^{-\frac{\lambda_o^2 w^2}{8d^2 c^2}\omega^2}m(\omega) \tag{4.39}$$

The original frequency spectrum of the data signal was $m(\omega)$, but that has now been narrowed by the filter / frequency response $i'(\omega)$ to give us a received data signal of $p(\omega)$. The $1/e$ frequency width by which the data frequency spectrum is narrowed is given by:

$$f_{1/e} = \frac{1}{2\pi}\sqrt{\frac{8d^2 c^2}{\lambda_o^2 w^2}}$$

$$= \frac{\sqrt{2}dc}{\pi\lambda_o w} \tag{4.40}$$

If a minimum sized architecture is used for our filter then $d = 1.5\lambda_o$, $w(\equiv \frac{ND}{2})$ =1.68mm, λ_o =1.55μm giving us a frequency broadening of $f_{1/e} = 121$GHz. This corresponds to a maximum allowable bit rate of $2 \times f_{1/e} = 242$Gb/s, before temporal dispersion and inter-symbol interference becomes a problem. Since $w \equiv ND/2$, we can re-write equation (4.40) as:

$$f_{1/e} = \frac{2\sqrt{2}c}{\pi}\frac{d}{\lambda_o ND} \tag{4.41}$$

Using the results of previous analysis, such as equation (4.13) where $ND \geq \frac{\lambda_o d}{\mathcal{R}}\sqrt{1 - \lambda_o^2/d^2}$, we can write:

$$ND \geq \frac{\lambda_o d}{\mathcal{R}}\sqrt{1 - \frac{\lambda_o^2}{d^2}}$$

$$\rightarrow \frac{d}{\lambda_o ND} \leq \frac{\mathcal{R}}{\lambda_o^2}\left(1 - \frac{\lambda_o^2}{d^2}\right)^{-\frac{1}{2}} \tag{4.42}$$

Substituting the inequality (4.42) into equation (4.41), we find that the maximum bit rate is given by:

$$f_{1/e} \leq \frac{2\sqrt{2}c}{\pi}\frac{\mathcal{R}}{\lambda_o^2}\left(1 - \frac{\lambda_o^2}{d^2}\right)^{-\frac{1}{2}}$$

$$\leq 1.21 f_o\frac{\mathcal{R}}{\lambda_o} \tag{4.43}$$

Thus we find that the maximum bit rate is ultimately limited by the desired resolution $\mathcal{R}$ of the filter, and the wavelength λ_o and frequency f_o of the carrier wave. A filter with a high wavelength resolution will be both large and less able to filter high bit rates. For a polarisation-insensitive, low loss filter, the maximum bit rate is also in effect *independent of the geometry of the filter*. The equation does show however, that as the fixed grating pitch d tends towards λ_o, the maximum allowable bit rate increases, albeit at the expense of polarisation sensitivity and distorted spot-size.

The temporal dispersion problem could be solved by inserting an additional fixed grating of the same pitch, since a pair of matched gratings cancel each others spectral broadening

out. But placing an additional grating just before the second lens would also cancel out the wavelength dispersive nature of the filter, and negate its operation. Another possibility may be to couple the filtered (and spectrally broadened) light back into the output fibre, and then couple it back out into a second free-space architecture containing just the additional grating. This would compensate for the temporal dispersion, but would also greatly increase the complexity of the wavelength filter. A suitably chirped fibre grating could also be used to compensate for the filter induced dispersion.

Chapter 5

Digitally Tunable Fibre Laser

5.1 Introduction

Tunable fibre lasers will potentially serve an important function in WDM telecommunications networks, acting as stable and pure laser sources. They have a very narrow linewidth, high output powers and large tuning ranges. This also makes them suitable for use in sensing, spectroscopy and general scientific research applications, so making them an important technology to be developed.

The first fibre lasers were already demonstrated in 1961 [129], but the lack of a supporting technology in glass fibres and pump semiconductor lasers meant that they became a mere scientific curiosity, to be consigned to the graveyard of scientific history. However, the subsequent invention in 1966 of the optical glass fibre[130] and a further 20 years of development to reduce fibre attenuation and dispersion, as well as the development and availability of suitable high-gain semiconductor sources (or optical pumps) all came together in 1985 when interest was suddenly reawakened in fibre lasers and optical fibre amplifiers with the demonstration of the neodymium-doped fibre laser[131], followed by the erbium-doped fibre laser (EDFL) [48] and finally the erbium-doped fibre amplifier (EDFA) [1]. The huge impact these new technologies would have on all levels of optical telecommunications immediately became apparent[4], and they have since been rapidly developed.

The relatively long cavity lengths of fibre lasers (often of the order of tens of metres, although some fibre lasers have cavity lengths of only a few millimetres or centimetres) results in very narrow linewidths and very closely spaced longitudinal cavity modes, which enables almost continuous tuning. High output powers and efficiencies are also possible with fibre lasers, due to the tight optical confinement of the optical fibre and the high gain available from EDFAs acting as the gain medium. Their wavelength tunability, large tuning range (set by the gain medium), stability and very narrow linewidths makes them suitable for WDM telecommunications systems. They can be used as stable tunable sources in direct detection systems, but in the longer term, their narrow linewidths will also make them

ideal for use as tunable local oscillators in coherent detection telecommunications systems. Modelocked fibre lasers have also been developed as efficient optical soliton generators for use in high bit rate OTDM telecommunications systems. Coupled with their tunability, the use of such modelocked fibre lasers in combined WDM/OTDM telecommunications systems is currently being seriously investigated. Fibre lasers have the additional advantages that they can be pumped with efficient and compact laser diodes, and are compatible with fibre optic components, leading to low coupling losses with telecommunications systems. The feature of EDFAs which makes them good travelling wave optical amplifiers is the relative slow relaxation times (milliseconds) of the excited erbium electrons, but this means that an EDFL has slow gain dynamics, making it unsuitable for high speed direct data modulation. However, they can be easily externally-modulated. A review of recent research into tunable fibre lasers is to be found in §1.3.1.

In this chapter, results are presented of a tunable erbium-doped fibre laser, tuned using a holographic wavelength filter in conjunction with a high gain EDFA. Tuning over a range of 38.5nm in steps of 1.3nm has been achieved, with CW output powers of up to -13dBm[102]. The inherent EDFL 3dB lasing linewidth was found to be of the order of 3kHz, and the wavelength stability was about 0.1nm. Multiple lasing has also been demonstrated, albeit with significant mode-competition.

5.2 Experiment

5.2.1 EDFL Architecture

The tunable holographic wavelength filter used within the digitally tunable EDFL is the same as described in §4.4. The filter had a theoretical tuning range of 82nm across the erbium window, a passband full-width half-maximum (FWHM) of 2nm and could be tuned in steps of 1.3nm. A schematic diagram showing the architecture of the experimental setup is shown in figure (5.1), while a photograph of the experimental apparatus is shown in figure (5.2). All fibre used was standard telecommunications $9/125\mu m$ single-moded fibre with polished FC/PC connectors. Each optical element used within the fibre ring was FC/PC compatible. The wavelength filter was placed within the cavity of a fibre ring resonator along with the high gain EDFA. An optical isolator within the EDFA ensured unidirectional travelling-wave operation thus avoiding spatial hole burning and multimode lasing. A 3dB output coupler was inserted in the loop, just after the wavelength filter, for monitoring purposes. The output coupler was placed before the EDFA so as to limit the maximum possible output power. This was to ensure that the measuring equipment used, such as the optical spectrum analyser, would not be damaged by high powers. Placing the 3dB coupler after the EDFA should allow higher output powers.
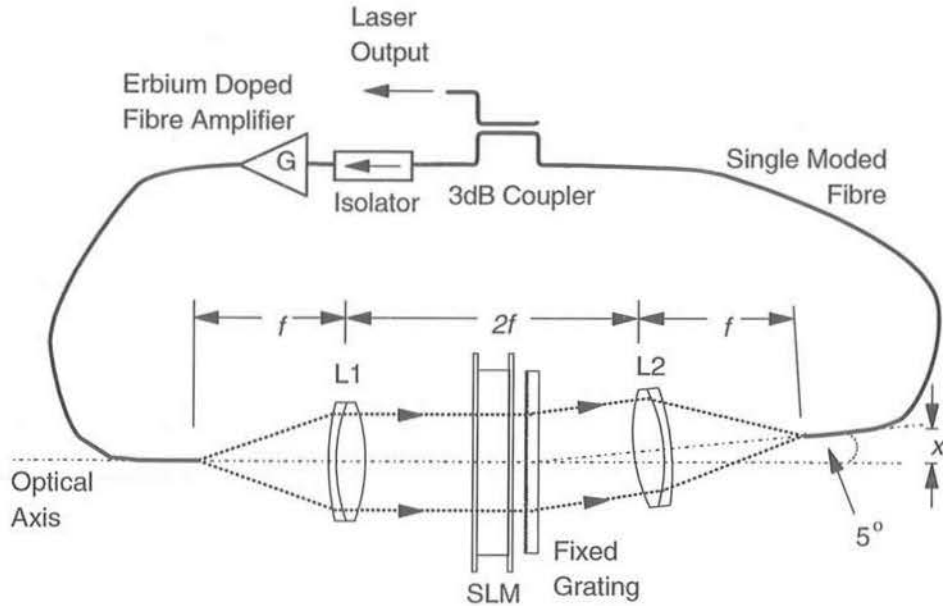
Figure 5.1: Holographic digitally tunable erbium doped fibre laser

5.2.2   Roundtrip Losses

None of the optical components used in the experiment were optimised to reduce reflections at 1.55μm. The total loss through the wavelength filter was calculated as 22.8dB - as described in §4.4.4. The output coupler contributed a further intrinsic loss of 3dB, as well as an extra loss of 0.9dB due to FC/PC connectors being spliced on to the coupler fibre ends. Each FC/PC connection contributed a further loss of about 0.2dB, so that with 5 FC/PC connections required to join the optical component into a ring loop, an additional roundtrip loss of 1.0dB was caused. Losses due to attenuation can be ignored, since the fibre loss is estimated as 0.2dB/km, and the fibre loop is not more than 60m. The total roundtrip loss is estimated at about 27.7dB.

5.2.3   EDFA Specification

The EDFA used in the EDFL experiments was a Hewlett Packard EFA2002, which was bidirectionally pumped with two 1480nm pump laser diodes. The small signal gain was at least 35dB (with -30 dBm input power) providing up to 14dBm output power, and a typical bandwidth of 40nm for a gain of at least 25dB [132]. The measured amplified spontaneous emission (ASE) of the EFA2002, which has the same shape as the gain spectrum is shown in figure (5.3).

Figure 5.2: Photograph of EDFL experimental setup, with tunable filter, EDFA, 3dB coupler, SLM power supply and controlling PC in view
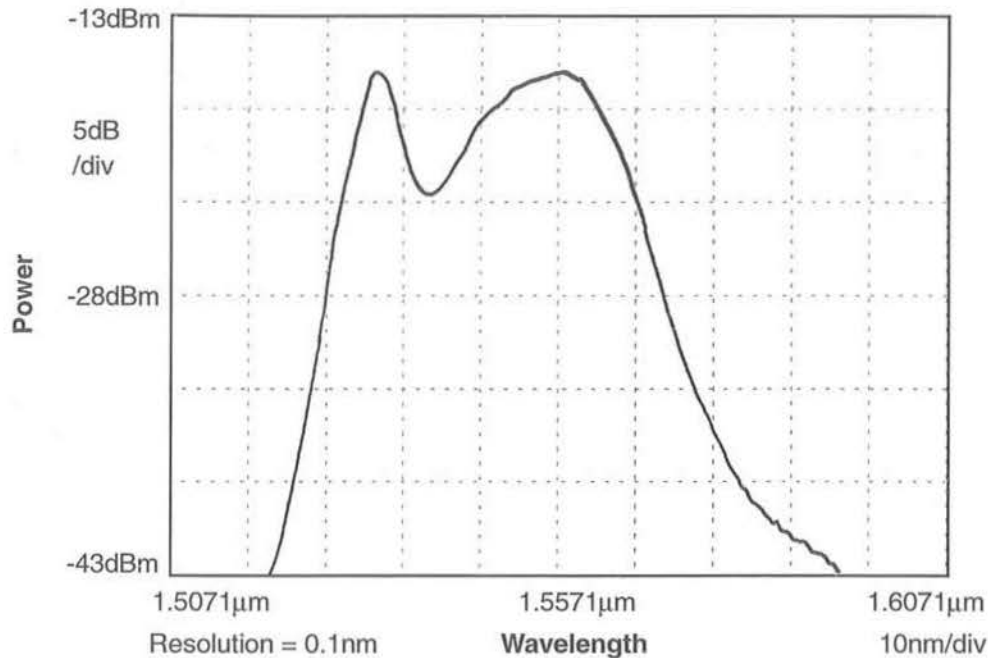
Figure 5.3: ASE spectrum of HP EFA2002 at a pump current of 350mA

5.3   Results

5.3.1   Tuning Range

Single-moded lasing of the EDFL was achieved over the range 1528.6 - 1567.1nm, although with a large variation ($\sim$ 30dB) in output power, corresponding to the characteristic EDFA gain spectrum, such that the extreme lasing wavelengths were barely above threshold. The tuning range of 38.5nm covered the whole of the erbium window, but only used a small section of the available 82nm range of the wavelength filter. An arbitrary group of eleven successively tuned lasing modes[1] is shown in figure (5.4). The figure shows that the lasing modes have at least 30dB side-mode suppression. Each mode is on average 1.3nm distant from its neighbouring mode, which is in line with the expected performance of the wavelength filter. There are variations in the relative distances of the lasing modes from each other, however, which is probably due to the non-uniform gain spectrum, but may also be due to the actual hologram displayed on the SLM. Each mode had on average an output power of about -13dBm, corresponding to about 50μW. More power could be accessed by placing the output coupler after the EDFA. The slightly 'ragged' appearance of some of the lasing peaks is due to mode-hopping, where non-uniformities in the gain spectrum excite

---

[1]The EASLM had a memory capacity for 11 holograms, so that the EDFL could only be tuned to 11 wavelengths at a time.
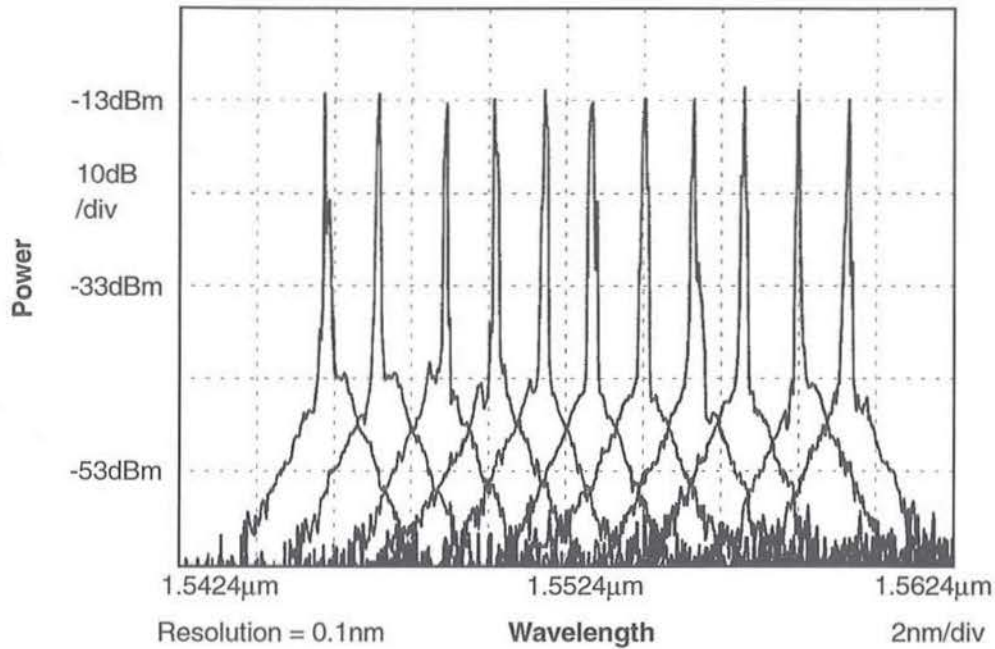
Figure 5.4: Eleven successively tuned lasing wavelengths

other lasing modes lying within the filter pass band.

5.3.2 Wavelength Stability

For telecommunications applications, the wavelength stability of a tunable EDFL is an important characteristic. Due to the free-space architecture of the wavelength filter, vibration of the optical elements with respect to each other causes a slight change in the central filtered wavelength, and hence the lasing frequency. A micron change in the position of the stage supporting the output fibre leads to a change in the lasing wavelength of about 0.1nm. To assess the long term stability of the EDFL, an experiment lasting 3.9 hours was performed. The EDFL was allowed to lase CW with the same hologram displayed on the SLM throughout. Every 1.4s a reading was taken of the lasing wavelength, so that 10,000 readings were taken over the 3.9 hours. A histogram (or frequency of occurrence of each wavelength) with a resolution of 4pm and a temporal plot of the readings are shown in figure (5.5). The histogram of figure (5.5a) shows that the EDFL had two principle modes of lasing at 1548.71nm and 1548.80nm, separated by 90pm, as well as a couple of other modes a further 90pm away on either side. Although the fibre laser has an almost continuous range of longitudinal modes, spaced by about 14fm ($i.e.$ 14×10^{-15}m), the glass flat supporting the fixed grating acts as an additional Fabry-Perot cavity of thickness 9mm. This means that the EDFL can only lase at the superimposed longitudinal modes due to the glass flat,
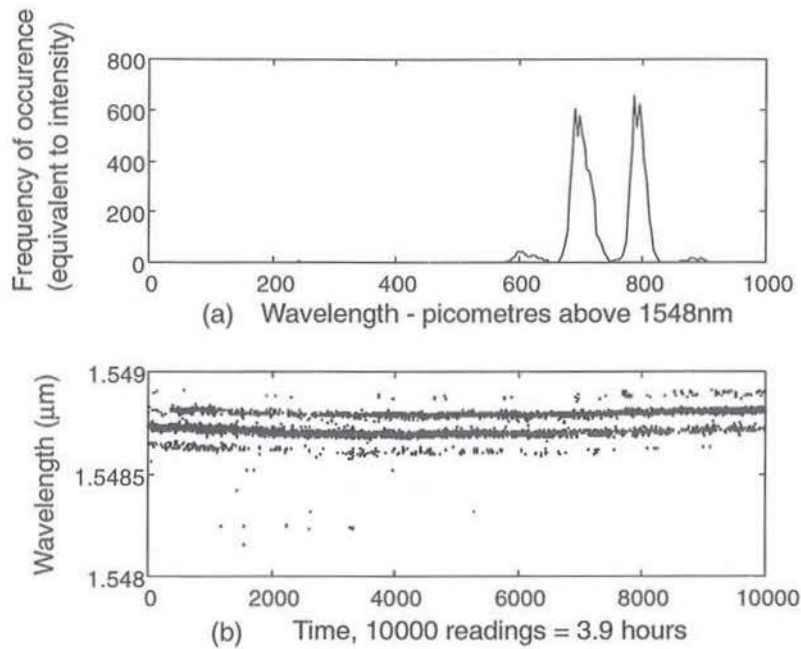
Figure 5.5: Histogram and temporal plot of wavelength stability of EDFL

rather than at the quasi-continuous modes due to the fibre ring. The mode separation $\Delta\lambda$ due to a etalon cavity (such as the glass flat or fibre ring) of length L is given by:

$$\Delta\lambda = \frac{\lambda_o^2}{2nL} \tag{5.1}$$

For the glass flat, we assume a refractive index $n=1.47$, $\lambda_o = 1.55\mu m$ and the cavity length $L = 9$mm which yields a mode separation $\Delta\lambda = 91$pm. This corresponds very closely with the mode spacing as depicted in figures (5.5a) and (5.6a).

To verify that the SLM itself was not contributing further to the wavelength instability in some way, it was removed from the cavity (thus disabling tuning) while still keeping the fixed grating within the ring. A similar long term experiment was performed to measure the stability of the lasing wavelength. The resulting histogram and time-plot are shown in figure (5.6). Many more modes due to the glass flat cavity are now present in this figure, each uniformly spaced approximately 90pm apart. The time plot of the mode hopping shows a downward trend in the lasing wavelength in time. This is probably due to mechanical drift of the stage supporting the output fibre. Mechanical vibration and random thermal fluctuations of the EDFA gain spectrum would account for the spread in lasing wavelength within each longitudinal mode. Figure (5.6a) displays more concurrent lasing modes than in figure (5.5a). Apart from the downward trend of the wavelength with time, this is probably due to the SLM itself acting as another Fabry-Perot cavity of a couple of millimetres width.
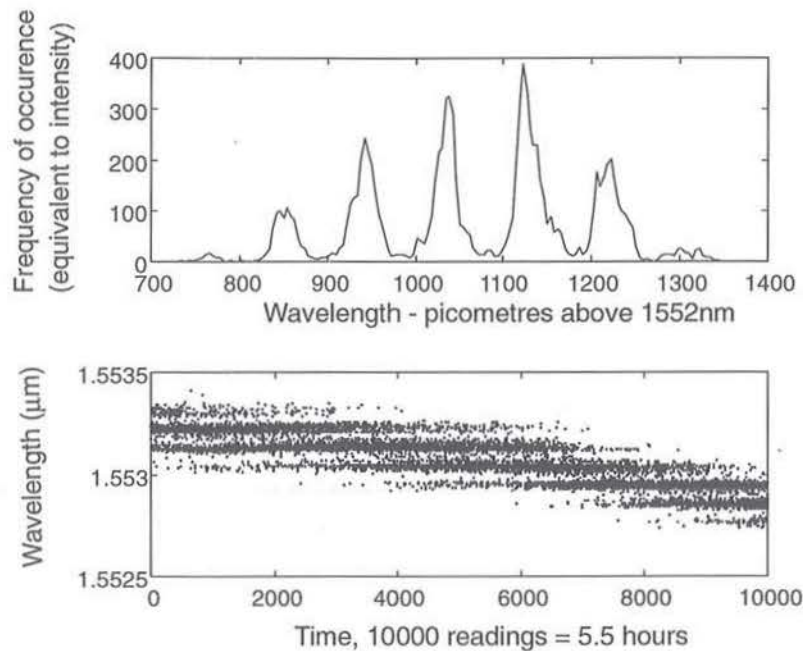
Figure 5.6: Histogram and time plot of wavelength stability of EDFL with no SLM in cavity

Its mode spacing is even larger than for the glass flat, which results in the suppression of many of the glass flat modes. This provides a mechanism to stabilise the lasing wavelength still further, by the insertion of a very thin optical glass flat, so that only one lasing mode is allowed. Mechanical vibrations still need to be minimised however, to reduce the wavelength variation within the mode.

5.3.3 Fine Tuning of EDFL

Fine-tuning of the EDFL is also of interest. Figure (5.4) displays 11 successive lasing modes of the digital tunable EDFL, in which we see that the wavelength differences between the modes are not a uniform 1.3nm. From consideration of the filter operation, we would normally expect there to be a constant wavelength difference between the lasing modes, but the fact that these particular mode spacings are non-uniform leaves open the possibility that these differences may be controlled to enable fine-tuning.

One possible mechanism for fine-tuning is to design holograms which ostensibly tune to the same wavelength. Since a non-deterministic algorithm is used to generate the holograms, there are ultimately many different possible hologram solutions. The hologram for each solution, however, will have a slightly different fundamental spatial period as well as a different phase profile. This theoretically means that for each hologram, a different wavelength should couple most efficiently into the output fibre, causing the EDFL to lase at a
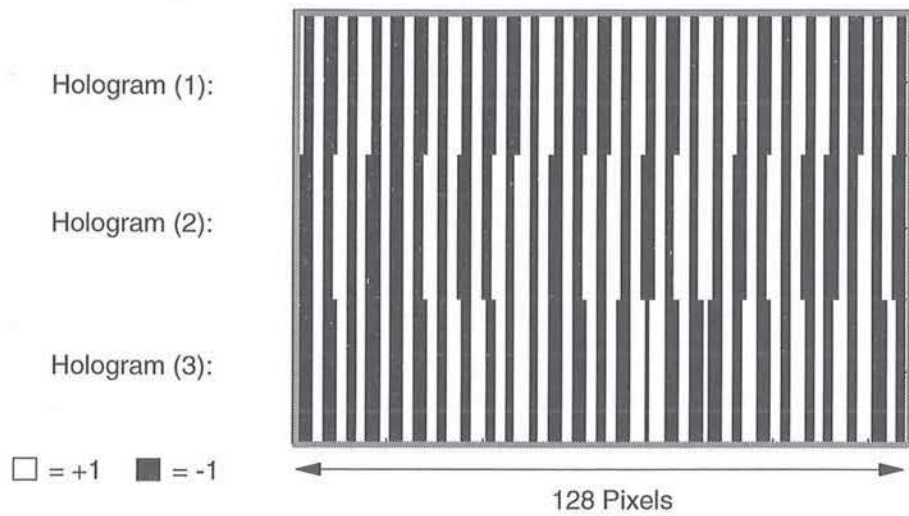
Figure 5.7: Three holograms with a similar fundamental spatial frequency
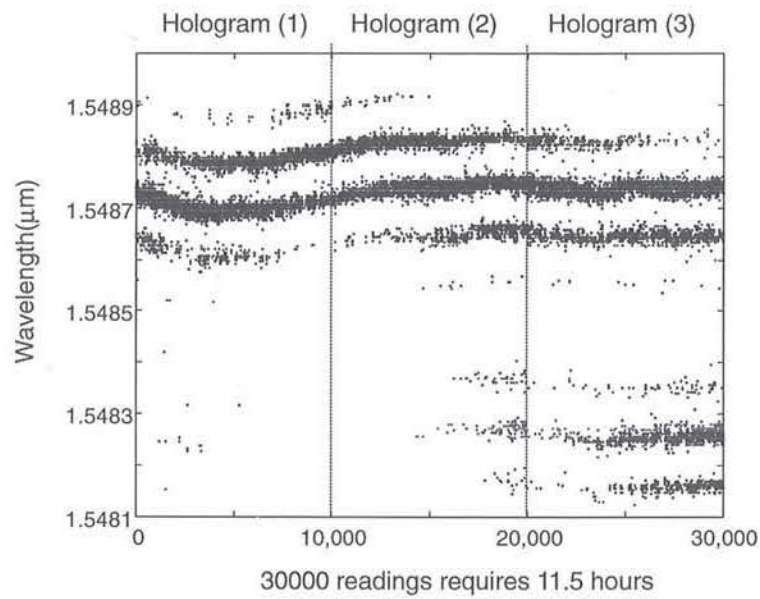
Figure 5.8: Lasing wavelengths of EDFL using the three similar holograms

different wavelength according to the hologram displayed. This was experimentally tested using 3 generated holograms, where each had a slightly different fundamental spatial period. Figure (5.7) depicts the three holograms, alongside each other.

It can be seen that though totally individual, each hologram has a similar spatial period. Each hologram was displayed in turn on the SLM, and the EDFL allowed to lase for almost 4 hours for each hologram, during which 10,000 readings of the lasing wavelength were made. Figure (5.8) shows the resulting plot of the temporal variation in wavelength for each hologram displayed. Unfortunately the results shown in the figure are inconclusive. Too much mode hopping is obscuring any fine tuning which may be taking place. The trend towards a lower wavelength is independent of the three holograms displayed, and again is most likely due to mechanical drift of the supporting stages. In addition, the etalon effects due to the glass flat of the fixed grating and the glass of the SLM force the EDFL to only lase in certain longitudinal modes. If the optimally coupled wavelengths of the three holograms lie outside these allowed modes, then the EDFL cannot lase at these wavelengths. Instead the EDFL will only lase in the nearest allowable mode. Thus it would appear that the use of a thin etalon to ensure wavelength stability of the EDFL would also exclude the the possibility of fine-tuning.

5.3.4 Laser Linewidth

The very narrow linewidth $\Delta\nu$ of the EDFL presents practical difficulties when one tries to measure it. An attempt to measure the linewidth of the tunable EDFL has been made using a heterodyne self-beating technique[133], incorporating a delay line and a 100.6MHz frequency shift using an AOM. The equipment used to perform the experiment was an Anritsu optical linewidth analyser MS9602A and Anritsu RF spectrum analyser MS2601A. The quasi CW output from the EDFL was fed into the apparatus. The SLM required periodic refreshing since the FLC was not completely bistable, so that the frame refresh
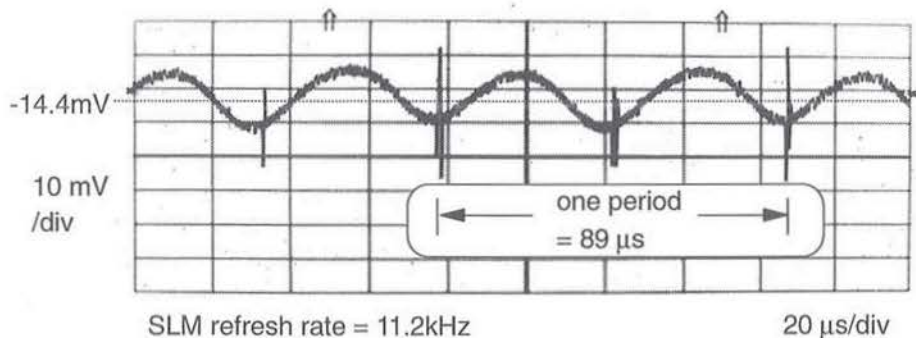
Figure 5.9: Digital oscilloscope trace of EDFL output power
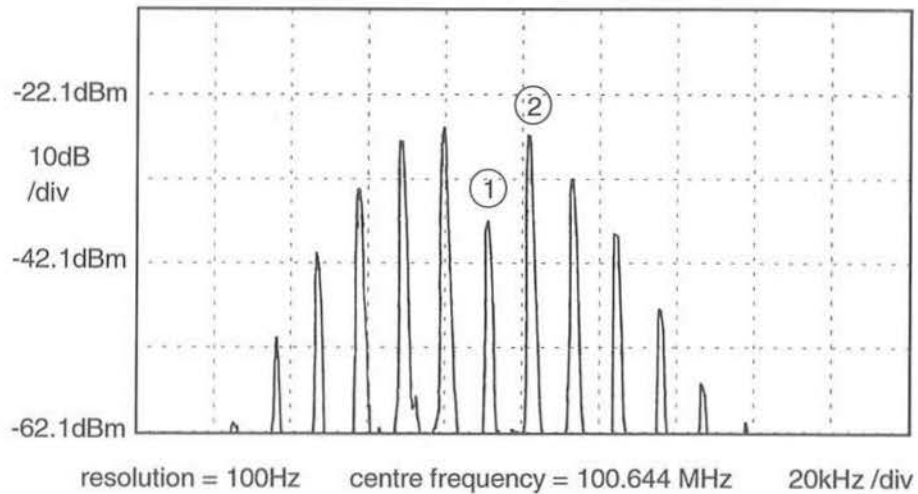
(a) Linewidth of EDFL due to modulation of SLM
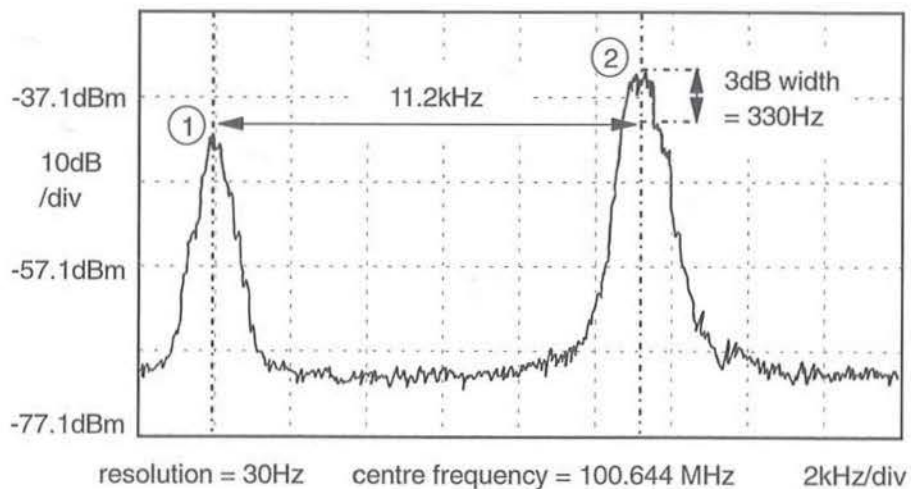
(b) Zoomed-in linewidth of EDFL, concentrating on peaks 1 & 2

Figure 5.10: Heterodyne measurements of the EDFL linewidth with 5km delay line

rate was 11.2kHz. This periodic refreshing is evident in figure (5.9) where the laser output was received by a large area photodiode connected to a digital oscilloscope which displayed the temporal variation of the laser power. It appears that the SLM employs an interlaced addressing scheme to its pixels, so that it requires two sweeps of the display for the SLM to be totally refreshed. Thus the larger spike in the trace corresponds to the end of the full refresh frame, while the smaller spike corresponds only to the end of one interlace. Figure (5.10) shows the radio-frequency plot of the measured beating frequencies and the resulting comb-like array of frequencies in the RF spectrum of the EDFL, each with a separation of 11.2kHz corresponding to the SLM refresh frequency. Thus the SLM chops up the laser linewidth into a series of harmonics. Figure (5.10b) shows a higher resolution plot of two of the harmonics. To confirm that the harmonic comb of frequencies evident in the RF spectrum is due to the SLM modulating the laser output, the linewidth of the EDFL was measured with the SLM removed from the cavity. This made the EDFL non-tunable and also reduced the roundtrip losses, so substantially increasing the output power. The resulting EDFL had a non-modulated CW output, and the linewidth[2] measured using the self-heterodyne technique is shown in figure (5.11). The linewidth measurement shows that only one fundamental lasing mode is present; the neighbouring 'modes' suppressed by > 40dB are an artifact due to reflections in the system. The self-heterodyne technique relies on splitting the light into two, delaying the first signal sufficiently to make it incoherent with respect to the second signal, and frequency shifting the second signal via an AOM. The two signals are then mixed again to give a true reading of the linewidth. Unfortunately, the narrower the linewidth, the greater is the delay line required to make the one signal incoherent with respect to the other. If the first signal is still slightly coherent with respect to the second signal, then the linewidth is measured to be narrower than it really is. In addition, the resolution of the system is proportional to the delay, so that a higher resolution requires a longer delay line. Unfortunately, a sufficiently large delay line was not available to give the resolution required to measure the linewidth completely accurately. However, by extrapolation of the measured linewidths for various delay lengths, and also comparing the results with those measured for broader linewidth laser sources, a good approximation for the linewidth was calculated. The following table shows the measured linewidths (without the SLM in the cavity) for various delay lines:

Delay Line:	5m	5km	14.6km
System Resolution:	20MHz	21.7kHz	6.7kHz
Measured linewidth ($\Delta\nu_m$):	< 30Hz	330Hz	1.7kHz

---

[2]The laser FWHM linewidth $\Delta\nu$ is in fact given by the *half-width half-maximum* of the curve ($\Delta\nu_m$) experimentally measured using the self-heterodyne technique.
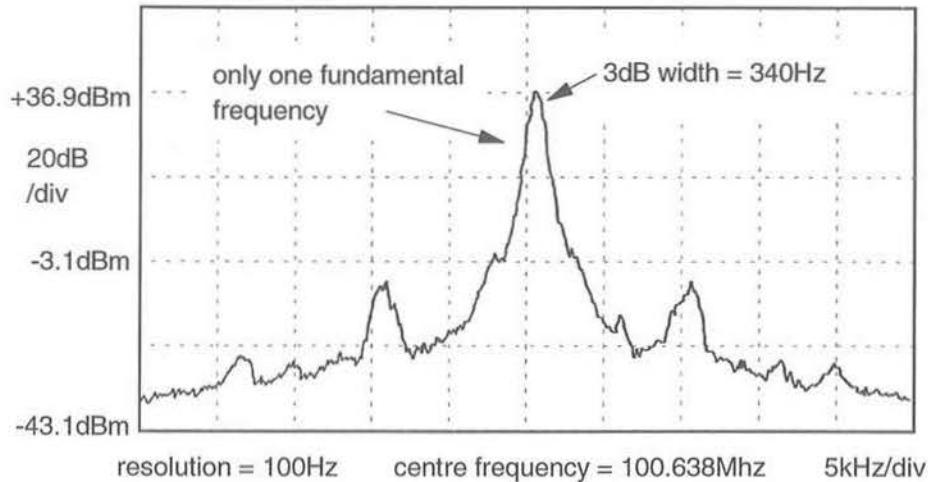
Figure 5.11: Heterodyne measurement of the EDFL linewidth without SLM in cavity, 5km delay line

From the table, we can see that the inherent EDFL linewidth $\Delta\nu$ lies within the limits $1.7\text{kHz} < \Delta\nu < 6.7\text{kHz}$. By extrapolation of the results from the above table we find that the inherent linewidth converges to $\Delta\nu \sim 3\text{kHz}$. Thus the intrinsic linewidth of the EDFL is of the order of 3kHz, but modulation by the SLM produces a comb of frequencies, so that the actual linewidth of the EDFL becomes approximately 100kHz, which is relatively large for a fibre laser.

However, a fully bistable FLC SLM requiring no refreshing used within the cavity of an EDFL should allow a narrow linewidth of about 3kHz.

5.3.5 Characteristic LI-Curve

The characteristic plot for the EDFL operating in CW mode is shown in figure (5.12). The EDFA used in the EDFL did not allow variation of the pump current, so a variable neutral density filter was used to vary the loss in the cavity, while keeping the gain constant. Due to mode-hopping the curve is not as straight as would be expected, but it displays the feature generally seen in a laser 'LI-curve', principally a clear transition between spontaneous emission and lasing behaviour. Threshold occurred for a neutral density filter transmission of about 18%. Since the maximum integrated output power of the EDFA is about 20mW, for a pump current of 350mA, we assume that the pump power must also be of the order of 20mW. The output power slope efficiency is estimated to be about 0.14%. This is a low figure because of the present relatively high loss of the wavelength filter.
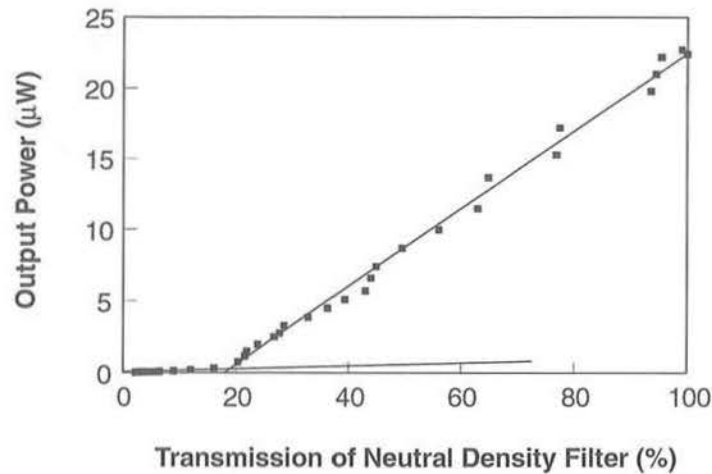
Figure 5.12: Characteristic curve for the EDFL

5.3.6   Simultaneous Multiple-Wavelength Lasing

A hologram with a mixed spatial frequency was designed to allow the EDFL to simultane-
ously lase at 1562.5nm and at 1556nm. The filter passbands for this hologram can be seen in
§4.4.6. The spectral plot is shown in figure (5.13). Unfortunately due to the gain medium
being relatively homogeneous and dependent at the two wavelengths, mode competition
meant that the lasing mode powers fluctuated considerably. Figure (5.13) is a 'snapshot'
of when the two modes were lasing equally for an instant. The power in each mode is also
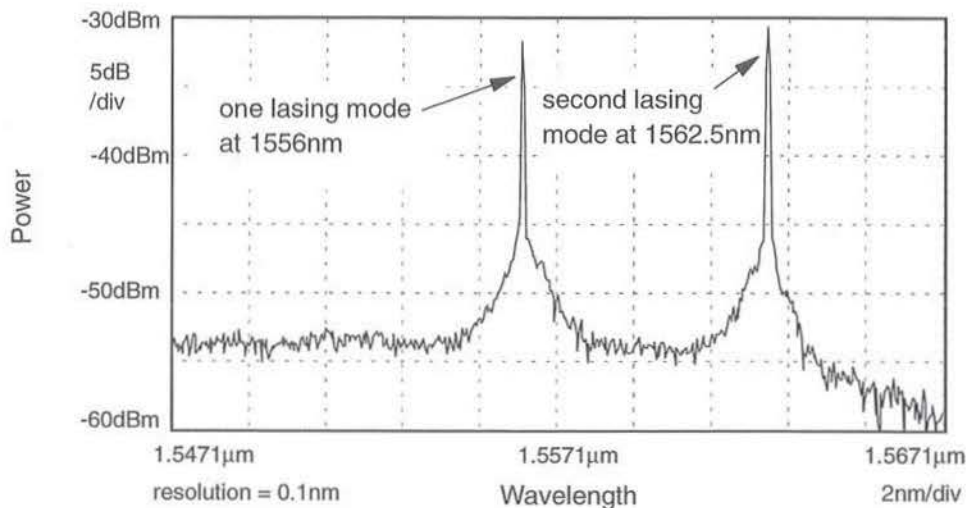
Figure 5.13: Two competing lasing modes at 1556nm and 1562.5nm

considerable lower than usual, since only half the EDFA power is available to each mode, the hologram has less than half the usual diffraction efficiency for each the two wavelengths, and a 10/90 coupler was used to output the lasing power. For successful stable multiple lasing to occur, each wavelength requires an independent gain medium, so as to avoid mode competition. In a totally homogeneous broadband gain medium, mode competition occurs, whereas gains for the various wavelengths in an inhomogeneous medium are relatively independent of each other, so allowing stable co-lasing. The EDFA lies somewhere in between the two extremes, since the gain spectrum is relatively uneven, as shown in figure (5.3), and so only limited co-lasing is possible.

5.3.7   Q-switching

The SLM modulation of the light in the EDFL cavity can cause Q-switching, when the refresh frequency is relatively slow. Whenever the hologram is written to the SLM (rather than just refreshed) the cavity loss is sufficiently high to bring the EDFL below threshold and stop lasing action. The FLC SLM operates in the required manner even when high optical powers are incident upon it, and so it is also suitable as the tuning element in a tunable soliton generating EDFL, where the peak powers are very high. It may be possible for the SLM itself to be also used to modelock the EDFL, and generate ultra short pulses.

5.4   Conclusions

In this chapter we have described the performance of an EDFL which is digitally tunable. Its tuning range of 38.5nm is comparable to the ranges of existing tunable EDFLs as described in §1.3.1, and is tunable in steps of 1.3nm. We have measured an ultra-narrow inherent linewidth of the EDFL of the order of 3kHz. The linewidth was broadened to about 100kHz due to modulation of the SLM as it refreshed the displayed hologram. A truly bistable FLC SLM will not need refreshing, so that optimising the FLC used in the SLM should allow true CW, ultra-narrow linewidth operation of the EDFL to occur. The EDFL exhibited single-moded behaviour due to its unidirectional ring architecture. Uniform output powers of about -13dBm were achieved. By placing the 3dB coupler after the EDFA, rather than directly after the filter, it should be possible to achieve EDFL output powers of the order of 10dBm. The wavelength stability was measured to be of the order of 0.1nm, which was due to mechanical vibrations of the optical components. A compact design incorporating GRIN lenses rigidly attached to the fixed grating and SLM, with no free-space section as such, should greatly increase the wavelength stability. Retuning of the EDFL is estimated at around 5ms, which corresponds to the time taken to write a new hologram to the SLM. Using a suitable direct addressing scheme to the SLM pixels, it should be possible to take advantage of the high speed switching of bistable FLCs, and achieve retuning in the order of

$20\mu s$ [134]. The digital hologram displayed on the SLM can be tailored to tune to multiple wavelengths simultaneously. A suitably inhomogeneous EDFA should allow the EDFL to lase at a comb of stable frequencies, without mode competition causing large fluctuations in the power of each lasing mode.

Chapter 6

Conclusions

In this dissertation a new technique for high resolution wavelength filtering has been presented. Holographic wavelength tuning may find a principal application in WDM telecommunications systems, where tunable sources, filters and receivers are required. It can be used within a holographic space-wavelength switch, allowing arbitrary switching and shuffling of the wavelengths between the fibres. Dynamic gain equalisation is an important issue which can also be addressed using holographic tuning. The holographically tunable erbium-doped fibre laser may also find use as a source in a WDM network or as a local oscillator for coherent detection. The advantages of holographic tuning are:

- optical transparency

- polarisation insensitivity

- digital, fast, fail-safe operation and robustness

- fine resolution over a large wavelength range

- multiple wavelength operation

- low crosstalk

We have demonstrated a wavelength filter with a 3dB passband of 2nm, tunable over 82nm in average steps of 1.3nm, with greater than 30dB sideband suppression a distance of 10nm from the passband centre. Multiple wavelength filtering has also been demonstrated, although with a reduced sideband suppression of up to 17dB and higher loss. The present loss of the filter is 22.8dB, which is still unacceptably high. However, it should be possible for this to be reduced to about 6.5dB. The wavelength stability of the filter due to mechanical vibrations is about 0.1nm. The physical dimensions of the filter were 384.4mm × 150mm × 150mm. It should be possible to build to build a wavelength filter with a resolution of 0.8nm having dimensions of 61.6mm× 6.76mm × 6.76mm. The filter should also be able to carry data at up to 242Gb/s with minimal distortion due to chirp from the fixed grating.
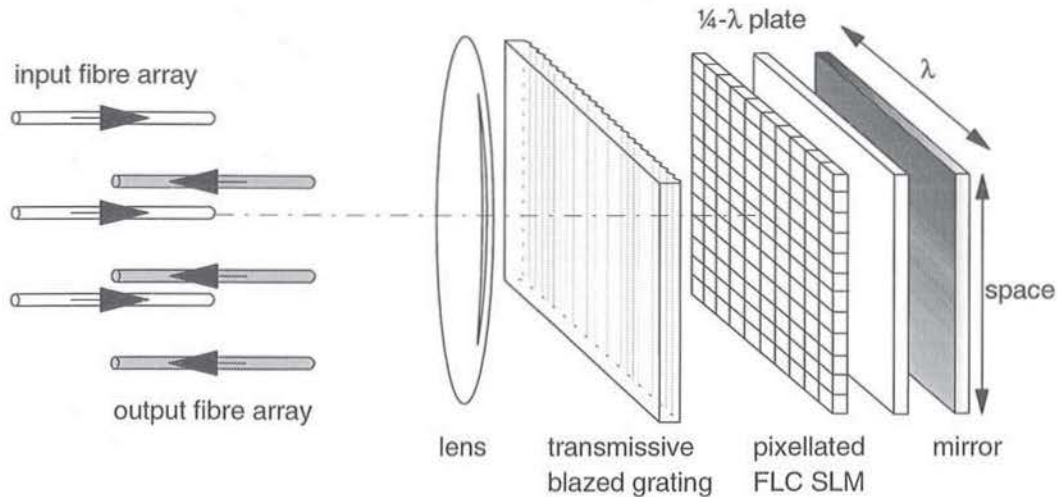
Figure 6.1: Exploded $2f$ compact 3×3 space-wavelength switch

The tunable erbium-doped fibre laser was tunable over a range of 38.5nm across the erbium window in discrete steps of 1.3nm. Output powers of up to -13dBm have been measured, although output powers of 10mW should be possible by using a different EDFL architecture. The inherent 3dB laser linewidth of the EDFL was measured to be of the order of 3kHz. The wavelength stability due to mechanical vibrations was about 0.1nm. Simultaneous multiple wavelength lasing action was also successfully demonstrated.

The theoretical section of this dissertation makes predictions of the expected performance of binary-phase holograms, which have been broadly confirmed by generated holograms used in experimental systems. The theory shows that the maximum diffraction efficiency we can expect from a binary-phase hologram is 36.5%, which is reduced as the hologram is required to fan out the light. The theory also shows that hologram SNR or noise suppression can be arbitrarily increased by using more pixels, and that the SNR of a hologram should be greater than $N/2p$, where N is the total number of pixels, and p is the hologram fan-out into one order.

6.1 Further Work

Although much has been demonstrated in this dissertation, there is still a lot of exciting work to be done in the area of holographic switching and filtering. In addition to the refining of the current devices to achieve better performance, there are still major proof-of-principle experiments to be performed.
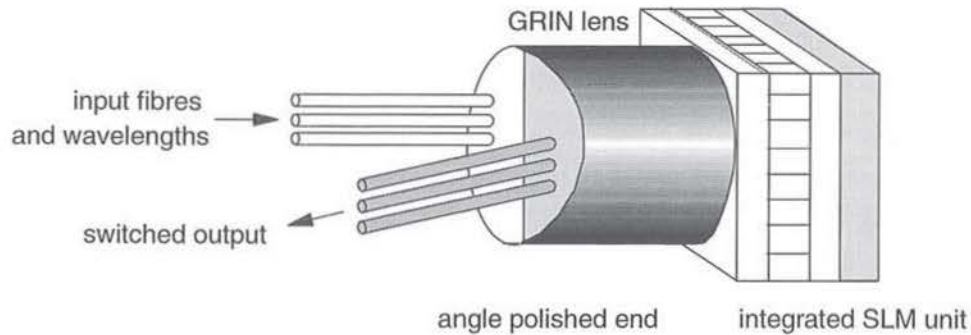
Figure 6.2: Packaged 3×3 space-wavelength switch

6.1.1 Low-loss Compact Space-λ Switch

The wavelength filter presently has a high loss which needs to be reduced substantially before it can be considered for use in a commercial optical telecommunications network. As highlighted in §4.4.4, a loss of only 6-7dB should be possible. This can be achieved by the use of a blazed fixed grating or refractive wavelength dispersive prism instead of the binary-phase diffraction grating. A high tilt angle FLC ($\theta = 90°$) or the use of a phase-doubling architecture such as a quarter-wave plate/mirror combination or polymer cholesteric liquid crystal (PCLC) mirror in conjunction with a FLC with tilt angle $\theta = 45°$ and a double pass through the FLC cell, as described in §2.3.2, would lead to higher diffraction efficiencies. Anti-reflection coatings on all the surfaces, and using large aperture lenses with a large numerical aperture would greatly increase the coupling efficiency between the fibres. The currently unused extra dimension of the SLM can also be used to add functionality to the switch, such as to make it into a space-wavelength switch. This would serve a very important function in dynamic wavelength-routed optical networks as an add-drop node. Figure (6.1) shows an 'exploded' concept for a polarisation-insensitive, optically transparent, compact, low-loss space-wavelength switch, utilising all the ideas developed in chapters 2 and 4. The switch acts as a 3×3 fibre cross-connect, but can also perfectly shuffle wavelengths between the various fibres. It may be possible to use a GRIN lens instead of a bulk refractive lens, but the limited NA and aperture of a GRIN lens will tend to limit the number of fibres possible to interconnect. Figure (6.2) shows how the packaged device might look. The analysis of chapter 3, however, indicates that the diffraction efficiency of binary-phase holograms tends to reduce as it is required to perform ever more fanning out. Thus the transmission loss of the space-wavelength switch will tend to increase as it is required to perform more complicated switching operations. The use of a continuous-phase FLC SLM may permit more efficient switching, although at the expense of polarisation sensitivity.

6.1.2 FLC Technology

A high tilt angle (*i.e.* $\theta = 90°$) FLC is required to improve the hologram diffraction efficiency. Unfortunately this is normally at the expense of switching speed. However, a FLC with a switching angle of 45° in conjunction with a quarter-wave-plate can also be used to increase the diffraction efficiency. A fully bistable FLC is also required so that the pixels on the SLM require no periodic refreshing. Currently, the SLM refresh modulates any signal passing through, leading to large signal degradation. An additional advantage of bistability is fail-safe operation of the device. In the event of a power failure, the SLM will still continue to diffract the light, and the device still operate, albeit without reconfigurability.

6.1.3 Apodisation

A filter for use in WDM networks with a rectangular passband is becoming increasingly desirable[22]. The relatively long 'tails' of the gaussian passband are undesirable, since crosstalk tends to be high. In addition, a flat passband has a greater wavelength misalign-ment tolerance, and better cascadability. Possible means to reduce the long gaussian tails include changing the output fibre end, so as to alter the coupling characteristic. A concave fibre end or a tapered polished fibre end may be sufficient. A suitable phase-plate before the second lens, to filter out the higher angles, may also be a solution. Finally, a lensing system incorporating additional spatial filtering could also be considered.

6.1.4 Continuous Tuning

Continuous tuning of the wavelength filter is desirable. This can most easily be achieved by using a continuous phase hologram. Careful design of the binary-phase hologram and defocussing of the spot on the output fibre may also allow continuous tuning, but this would be at the expense of reduced coupling efficiency, higher cross-talk and a wider passband.

6.1.5 Dynamic Spectral Equalisation

The holographic wavelength filter can also be used for the active management of WDM channels. In WDM telecommunications systems dynamic spectral equalisation is required since individual channel powers will tend to vary over time due to variable path losses, wave-length dependence of passive optical components and most significantly as a result of the non-uniform EDFA gain profile. A proof-of-principal demonstration of active holographic spectral equalisation for WDM has in fact been performed[103] by the Author[1] in collab-oration with A.D.Cohen. A copy of the manuscript, with the results of the experiments,

---

[1]Although the topic falls comfortably within the scope of this dissertation, meriting a chapter of its own, lack of time has meant that full, detailed research into the topic has not been possible within the time constraints of the Ph.D.
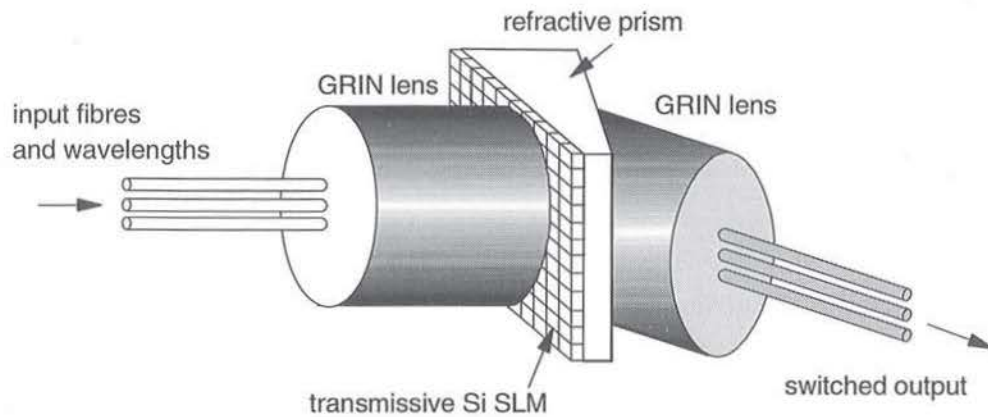
Figure 6.3: Compact space-λ switch using transmissive semiconductor-SLM with refractive prism

submitted for publication in Photonics Technology Letters is to be found in Appendix B. We have managed to control five WDM channels spaced by 4nm to reduce an input power variation of 8.5dB down to 0.3dB, while also providing gain of up to 3.3dB. In addition, an unused wavelength channel was 'knocked' out and the ASE suppressed by at least 18dB. Future work will involve the control of a greater number of more closely spaced channels (reflecting the present ITU standards of 0.8nm channel spacing), to provide greater individual channel gains, and higher suppression of ASE noise.

6.1.6   2-Dimensional Hologram Analysis

Although 2D holograms have been dismissed as finding no practical application (!) [135], a continued theoretical analysis of 2D holograms is required, so that the expected performance of 2D holograms in space-wavelength switches can be used within the design process. An analysis of multilevel phase holograms would also allow comparisons to be made between the performance of binary-phase and higher level phase holograms.

6.1.7   Semiconductor SLM

A semiconductor based SLM may enable very fast space-wavelength switching. Although the switch does not have to switch at the bit rate (*i.e.* of the order of 100ps at 10Gb/s), a switching time measured in microseconds is arguably too slow. Semiconductors, such as silicon (Si) and gallium-arsenide (GaAs), are transparent to infra-red light, and the plasma effect allows the local refractive index in the material to be altered by the injection of charge. A pixellated transmissive semiconductor SLM with different refractive indices means different optical path lengths, and thus variable phases. This electronic effect occurs

over time scales measured in nanoseconds, and so is three orders of magnitude faster than LC effects. As a guide, a change in carrier concentration of about $10^{24}\mathrm{m}^{-3}$ should cause a 1 - 2 % change in the refractive index[136]. A change in the local transmission of the semiconductor is also to be expected, due to the Franz-Keldysh effect, but it should be relatively small. Figure (6.3) depicts a space-wavelength switch using a transmissive Si-SLM to provide phase modulation in conjunction with a refractive prism which provides the high fixed wavelength dispersion. A silicon based SLM is potentially cheaper than GaAs, but it is likely that GaAs has the greater plasma effect, thus requiring substantially lower currents and power.

Bibliography

[1] R.J. Mears, L. Reekie, I.M. Jauncey, and D.N. Payne. Low-noise erbium-doped fibre amplifier at 1.54μm. *Electronics Letters*, 23(19):1026–1028, 1987.

[2] C.A.Brackett. Dense wavelength division multiplexing networks:principles and applications. *IEEE Journal on Selected Areas in Communications*, 8(6):948–964, 1990.

[3] G.R.Hill. A wavelength routing approach to optical communication networks. *Br Telecom Technol J*, 6(3):24–31, 1988.

[4] R.J. Mears and S.R. Baker. Erbium fibre amplifiers and lasers (tutorial review). *Optical and Quantum Electronics*, 24:517–538, 1992.

[5] P. Trischitta, M. Colas, M. Green, G. Wuzniak, and J. Arena. The TAT-12/13 Cable Network. *IEEE Communications Magazine*, 34:24–28, February 1996.

[6] B.J. Flanigan and J.E. Carroll. High speed direct modulation of diode lasers: towards Terabit communications. *IEE Colloquium*, Towards Terabit Transmission:Savoy Place, London, 19th May 1995.

[7] W.S. Lee, D. Garthe, G. Pettitt, and A. Hadjifotiou. Modelling and experimental comparison of a 40 Gb/s OTDM system over a transmission distance of 560km. *IEE Colloquium*, High Speed and Long Distance Optical Transmission:Aston University, Birmingham, 18th April 1996.

[8] A.H. Gnauck et. al. One Terabit/s transmission experiment. *OFC'96*, San Jose, CA:Postdeadline paper PD20, February 1996.

[9] H. Onaka. Terabit/sec WDM Systems Technologies. *Summer Topical Meeting*, Keystone, Colorado:WA1, August, 1996.

[10] E.L. Goldstein, L. Eskildsen, and A.F. Elrefraire. Performance implications of component crosstalk in transparent lightwave networks. *IEEE Photonics Technology Letters*, 6:657–660, 1994.

[11] K.W. Cheung, D.A. Smith, J.E. Baran, and B.L. Heffner. Multiple channel operation of an integrated acousto-optic tunable filter. *Electronics Letters*, 25:375–376, 1989.

[12] F. Heismann, L. Buhl, and R. Alferness. Electro-optically tunable narrowband Ti:LiNbO$_3$ wavelength filter. *Electronics Letters*, 23:572–574, 1987.

[13] B.L. Heffner, D.A. Smith, J.E. Baran, A. Yi-Yan, and K.W. Cheung. Integrated-optic acoustically tunable infra-red optical filter. *Electronics Letters*, 24(25):1562–1563, 1988.

[14] W. Warzanskyj, F. Heismann, and R.C. Alferness. Polarization-independent electro-optically tunable narrow-band wavelength filter. *Applied Physics Letters*, 53(1):13–15, 1988.

[15] D.A. Smith, J.E. Baran, K.W. Cheung, and J.J. Johnson. Polarization-independent acoustically tunable optical filter. *Applied Physics Letters*, 56(3):209–211, 1990.

[16] F. Heismann, M.D. Divino, and L.L. Buhl. Mirror-folded polarization-independent wavelength filter. *IEEE Photonics Technology Letters*, 3(3):219–221, 1991.

[17] A. d'Alessandro, D.A. Smith, and J.E. Baran. Polarisation-independent low-power integrated acousto-optic tunable filter/switch using APE/Ti polarisation splitters on lithium niobate. *Electronics Letters*, 29(20):1767–1769, 1993.

[18] D.A. Smith, J.J. Johnson, B.L. Heffner, K.-W. Cheung, and J.E. Baran. Two-stage integrated-optic acoustically tunable optical filter with enhanced sidelobe suppression. *Electronics Letters*, 25(6):398–399, 1989.

[19] J. Frangen, H. Herrman, R. Ricken, H. Seibert, W. Sohler, and E. Strake. Integrated optical, acoustically tunable wavelength filter. *Electronics Letters*, 25(23):1583–1584, 1989.

[20] H. Herrmann, P. Müller-Reich, V. Reimann, R. Ricken, H. Seibert, and W. Sohler. Integrated optical, TE- and TM-pass, acoustically tunable, double-stage wavelength filters in LiNbO$_3$. *Electronics Letters*, 28(7):642–644, 1992.

[21] J.L Jackel, J.E Baran, A. d'Alessandro, and D.A. Smith. A passband-flattened acousto-optic filter. *IEEE Photonics Technology Letters*, 7(3):318–320, 1995.

[22] D.A. Smith, H. Rashid, R.S. Chakravarthy, A.M. Agboatwalla, A.A. Patil, Z. Bao, N. Imam, S.W. Smith, J.E. Baran, J.L. Jackel, and J. Kallamn. Acousto-optic switch with a near rectangular passband for WDM systems. *Electronics Letters*, 32(6):542–543, 1996.

[23] S.F. Su, R. Olshansky, D.A. Smith, and J.E. Baran. Flattening of erbium-doped fibre amplifer gain spectrum using an acousto-optic tunable filter. *Electronics Letters*, 29(5):477–478, 1993.

[12] F. Heismann, L. Buhl, and R. Alferness. Electro-optically tunable narrowband Ti:LiNbO$_3$ wavelength filter. *Electronics Letters*, 23:572–574, 1987.

[13] B.L. Heffner, D.A. Smith, J.E. Baran, A. Yi-Yan, and K.W. Cheung. Integrated-optic acoustically tunable infra-red optical filter. *Electronics Letters*, 24(25):1562–1563, 1988.

[14] W. Warzanskyj, F. Heismann, and R.C. Alferness. Polarization-independent electro-optically tunable narrow-band wavelength filter. *Applied Physics Letters*, 53(1):13–15, 1988.

[15] D.A. Smith, J.E. Baran, K.W. Cheung, and J.J. Johnson. Polarization-independent acoustically tunable optical filter. *Applied Physics Letters*, 56(3):209–211, 1990.

[16] F. Heismann, M.D. Divino, and L.L. Buhl. Mirror-folded polarization-independent wavelength filter. *IEEE Photonics Technology Letters*, 3(3):219–221, 1991.

[17] A. d'Alessandro, D.A. Smith, and J.E. Baran. Polarisation-independent low-power integrated acousto-optic tunable filter/switch using APE/Ti polarisation splitters on lithium niobate. *Electronics Letters*, 29(20):1767–1769, 1993.

[18] D.A. Smith, J.J. Johnson, B.L. Heffner, K.-W. Cheung, and J.E. Baran. Two-stage integrated-optic acoustically tunable optical filter with enhanced sidelobe suppression. *Electronics Letters*, 25(6):398–399, 1989.

[19] J. Frangen, H. Herrman, R. Ricken, H. Seibert, W. Sohler, and E. Strake. Integrated optical, acoustically tunable wavelength filter. *Electronics Letters*, 25(23):1583–1584, 1989.

[20] H. Herrmann, P. Müller-Reich, V. Reimann, R. Ricken, H. Seibert, and W. Sohler. Integrated optical, TE- and TM-pass, acoustically tunable, double-stage wavelength filters in LiNbO$_3$. *Electronics Letters*, 28(7):642–644, 1992.

[21] J.L Jackel, J.E Baran, A. d'Alessandro, and D.A. Smith. A passband-flattened acousto-optic filter. *IEEE Photonics Technology Letters*, 7(3):318–320, 1995.

[22] D.A. Smith, H. Rashid, R.S. Chakravarthy, A.M. Agboatwalla, A.A. Patil, Z. Bao, N. Imam, S.W. Smith, J.E. Baran, J.L. Jackel, and J. Kallamn. Acousto-optic switch with a near rectangular passband for WDM systems. *Electronics Letters*, 32(6):542–543, 1996.

[23] S.F. Su, R. Olshansky, D.A. Smith, and J.E. Baran. Flattening of erbium-doped fibre amplifer gain spectrum using an acousto-optic tunable filter. *Electronics Letters*, 29(5):477–478, 1993.

[24] R. Brinkmann, M. Dinand, I. Baumann, Ch. Harizi, W. Sohler, and H. Suche. Acoustically tunable wavelength filter with gain. *IEEE Photonics Technology Letters*, 6(4):519–521, 1994.

[25] A. d'Alessandro, D.A. Smith, and J.E Baran. Multichannel operation of an integrated acousto-optic wavelength routing switch for WDM systems. *IEEE Photonics Technology Letters*, 6(3):390–393, 1994.

[26] M. Fukutoku, K. Oda, and H. Toba. Wavelength-division-multiplexing add/drop multiplexer employing a novel polarisation independent acousto-optic tunable filter. *Electronics Letters*, 29(10):905–907, 1993.

[27] J.L. Jackel, M.S. Goodman, J.E. Baran, W.J. Tomlinson, G.-K. Chang, M.Z. Iqbal, G.H. Song, K. Bala, C.A Brackett, D.A. Smith, R.S. Chakravarthy, R.H. Hobbs, D.J. Fritz, R.W. Ade, and K.M. Kissa. Acousto-optic tunable filters (AOTFs) for multiwavelength optical cross-connects: Crosstalk considerations. *IEEE Journal of Lightwave Technology*, 14(6):1056–1066, 1996.

[28] G.-K. Chang, G. Ellinas, J.K. Gamelin, M.Z. Iqbal, and C.A. Brackett. Multiwavelength reconfigurable WDM/ATM/SONET network testbed. *IEEE Journal of Lightwave Technology*, 14(6):1320–1340, 1996.

[29] D.A. Smith, R.S. Chakravarthy, Z. Bao, J.E. Baran, J.L. Jackel, A. d'Alessandro, D.J. Fritz, S.H. Huang, X.Y. Zou, S.-M. Hwang, A.E. Willner, and K.D. Li. Evolution of the acousto-optic wavelength routing switch. *IEEE Journal of Lightwave Technology*, 14(6):1005–1019, 1996.

[30] J.L. Jackel, J.E. Baran, G.-K. Chang, M. Z. Iqbal, G.H. Song, W.J. Tomlinson, D. Fritz, and R. Ade. Multichannel operation of AOTF switches: Reducing channel-to-channel interaction. *IEEE Photonics Technology Letters*, 7(4):370–372, 1995.

[31] D.A. Smith, A. d'Alessandro, and J.E. Baran. Reduction of crosstalk in acousto-optic switch by means of dilation. *Optics Letters*, 19(2):99–101, 1994.

[32] S.J. Madden. Properties of nonblocking single-substrate optical space switching networks constructed from directional couplers. *Applied Optics*, 33(36):8375–8386, 1994.

[33] C.A. Brackett. Multiwavelength Switching and Interconnection Networks. *Photonics in Switching (Editor J. Midwinter)*, Chapter 1, Book II:Academic Press, 1993.

[34] J. Stone and L.W. Stulz. Pigtailed high-finesse tunable fibre Fabry-Perot interferometers with large, medium and small free spectral ranges. *Electronics Letters*, 23(15):781–783, 1987.

[35] J.S. Patel, M.A. Saifi, D.W. Berreman, C. Lin, N. Andreadakis, and S.D. Lee. Electrically tunable optical filter for infrared wavelength using liquid crystals in a Fabry-Perot etalon. *Applied Physics Letters*, 57(17):1718–1720, 1990.

[36] K. Hirabayashi, H. Tsuda, and T. Kurokawa. New structure of tunable wavelength-selective filters with a liquid crystal for FDM systems. *IEEE Photonics Technology Letters*, 3(8):741–743, 1991.

[37] J.S. Patel and M.W. Maeda. Tunable polarization diversity liquid-crystal wavelength filter. *IEEE Photonics Technology Letters*, 3(8):739–730, 1991.

[38] K. Hirabayashi, Y. Ohiso, and T. Kurokawa. Polarization-independent tunable wavelength-selective filter using liquid crystal. *IEEE Photonics Technology Letters*, 3(12):1091–1093, 1991.

[39] A. Sneh and K.M. Johnson. High-speed continuously tunable liquid crystal filter for WDM networks. *IEEE Journal of Lightwave Technology*, 14(6):1067–1080, 1996.

[40] D.A. Smith, M.M. Choy, A. d'Alessandro, J.E. Baran, and A.W. Rajhel. Cascaded acoustooptic/fiber Fabry-Perot filter with a finesse over 2000. *IEEE Photonics Technology Letters*, 5(2):189–191, 1993.

[41] L.L. Buhl, R.C. Alferness, U. Koren, B.I. Miller, M.G. Young, T.L. Koch, C.A. Burrus, and G.Rayborn. Grating assisted vertical coupler/filter for extended tuning range. *Electronics Letters*, 29(1):81–82, 1993.

[42] F. Heismann, L.L. Buhl, B.I. Miller, M. Newkirk, U. Koren, M.G. Young, and R.C. Alferness. Polarization-independent wavelength filter using a grating-assisted vertical directional coupler in InP. *Applied Physics Letters*, 64(18):2335–2337, 1994.

[43] D.C. Griffiths and K.R. Preston. Space and wavelength filter for use in WDM-based optical switching networks. *Electronics Letters*, 28(10):1729–1730, 1992.

[44] Y. Suemura, A. Tajima, N. Henmi, H. Morimura, and H. Takahashi. An adaptive wavelength tunable optical filter employing an angle-tuned interference filter and an intelligent digital controller. *IEEE Journal of Lightwave Technology*, 14(6):1048–1054, 1996.

[45] R. Schiek, Y. Baek, G. Krijnen, and G.I. Stegeman. All-optical switching in lithium niobate directional couplers with cascaded nonlinearity. *Optics Letters*, 21(13):940–942, 1996.

[46] J. Gehler, A. Bräuer, W. Karthe, U. Trutschel, and M.A. Duguay. ARROW-based optical wavelength filter in silica. *Electronics Letters*, 31(7):547–548, 1995.

[47] H. Takahashi, Y. Hibino, and I. Nishi. Polarization-insensitive arrayed-waveguide grating wavelength multiplexer on silicon. *Optics Letters*, 17(7):499–501, 1992.

[48] R.J. Mears, L. Reekie, S.B. Poole, and D.N. Payne. Low-threshold tunable CW and Q-switched fibre laser operating at 1.55μm. *Electronics Letters*, 22(3):159–160, 1986.

[49] R. Wyatt. High-power broadly tunable erbium-doped silica fibre laser. *Electronics Letters*, 25(22):1498–1499, 1989.

[50] C.R. O'Cochlain and R.J.Mears. Broadband tunable single frequency diode-pumped erbium-doped fibre laser. *Electronics Letters*, 28(2):124–126, 1992.

[51] C.R. O'Cochlain. Tunable erbium-doped fibre lasers for lightwave communications systems. *PhD Thesis*, Cambridge University, 1992.

[52] I.N. Dulling III and R.D. Esman. Single-polarisation fibre amplifier. *Electronics Letters*, 28(12):1126–1128, 1992.

[53] Y. Shi, C.V. Poulsen, M. Sejka, M. Ibsen, and O. Poulsen. Tunable Pr^{3+}-doped silica-based fibre laser. *Electronics Letters*, 29(16):1426–1427, 1993.

[54] K. Iwatsuki, H. Okamura, and M. Saruwatari. Wavelength-tunable, single-frequency and single-polarisation Er-doped fibre ring-laser with 1.4kHz linewidth. *Electronics Letters*, 26(24):20332035, 1990.

[55] R.P. Davey, K. Smith, and A. McGuire. High-speed, mode-locked, tunable integrated erbium fibre laser. *Electronics Letters*, 28(5):482–484, 1992.

[56] P.F. Wysocki, M.J.F. Digonnet, and B.Y. Kim. Electronically tunable, 1.55-μm erbium-doped fibre laser. *Optics Letters*, 15(5):273–275, 1990.

[57] D.A. Smith, M.W. Maeda, J.J. Johnson, J.S. Patel, M.A. Saifi, and A. von Lehman. Acoustically tuned erbium-doped fibre ring laser. *Optics Letters*, 16(6):387–389, 1991.

[58] K. Doughty, D.E.L. Vaughan, K. Cameron, and D.M. Bird. Novel acoustically tuned fibre laser. *Electronics Letters*, 29(1):31–32, 1993.

[59] Y.T. Chieng, G.J. Cowle, and R.A. Minasian. Optically amplitude-stabilised tunable erbium-doped fibre laser with $< 20\mu$s tuning speed. *Electronics Letters*, 31(17):1451–1452, 1995.

[60] F. Fontana, N. Ridi, M. Romagnoli, and P. Franco. Fully integrated 30ps modelocked fiber laser electronically tunable over 1530-1560nm. *Optics Communications*, 107:240–244, 1994.

[61] J.L. Zyskind, J.W. Sulhoff, J. Stone, D.J. DiGiovanni, L.W. Stulz, H.M. Presby, A. Piccirilli, and P.E Prayamon. Electrically tunable, diode-pumped erbium-doped fibre ring laser with fibre Fabry-Perot etalon. *Electronics Letters*, 27(21):1950–1951, 1991.

[62] H. Schmuck, Th. Pfeiffer, and G. Veith. Widely tunable narrow linewidth erbium-doped fibre ring laser. *Electronics Letters*, 27(23):2117–2119, 1991.

[63] M.W. Maeda, J.S. Patel, D.A. Smith, C.L. Lin, M.A. Saifi, and A. von Lehman. An electronically tunable fiber laser with a liquid-crystal etalon as the wavelength-tuning element. *IEEE Photonics Technology Letters*, 2(11):787–789, 1990.

[64] P. Mollier, V. Armbruster, H. Porte, and J.P. Goedgebuer. Electrically tunable Nd^{3+}-doped fibre laser using nematic liquid crystals. *Electronics Letters*, 31(15):1248–1250, 1995.

[65] R. Kashyap, J.R. Armitage, R. Wyatt, S.T. Davey, and D.L. Williams. All-fibre narrowband reflection gratings at 1500nm. *Electronics Letters*, 26(11):730–732, 1990.

[66] G.A. Ball, W.W Morey, and J.P. Waters. Nd^{3+} fibre laser utilising intra-core Bragg reflectors. *Electronics Letters*, 26(21):1829–1830, 1990.

[67] G.J. Cowle, D.N. Payne, and D. Reid. Single-frequency travelling-wave erbium-doped fibre loop laser. *Electronics Letters*, 27(3):229–230, 1991.

[68] G.A. Ball and W.W Morey. Continuously tunable single-mode erbium fiber laser. *Optics Letters*, 17(6):420–422, 1992.

[69] G.A. Ball and W.W Morey. Compression-tuned single-frequency Bragg grating fiber laser. *Optics Letters*, 19(23):1979–1981, 1994.

[70] M. Ibsen, B.J. Eggleton, M.G. Sceats, and F. Ouellette. Broadly tunable DBR fibre laser using sampled fibre Bragg gratings. *Electronics Letters*, 31(1):37–38, 1995.

[71] D. Abraham, R. Nagar, M.N. Ruberto, G. Eisenstein, U. Koren, J.L. Zyskind, and D.J. DiGiovanni. Frequency tuning and pulse generation in a fiber laser with an intracavity semiconductor active filter. *IEEE Photonics Technology Letters*, 4(4):377–379, 1993.

[72] S.V. Chernikov, R. Kashyap, P.F. McKee, and J.R. Taylor. Dual frequency all fibre grating laser source. *Electronics Letters*, 29(12):1089–1090, 1993.

[73] J.T. Kringlebotn, J.-L. Archambault, L. Reekie, and D.N. Payne. $Er^{3+}:Yb^{3+}$-codoped fiber distributed feedback laser. *Optics Letters*, 19(24):2101–2103, 1994.

[74] M. Sejka, P. Varming, J. Hübner, and M. Kristensen. Distributed feedback Er^{3+}-doped fibre laser. *Electronics Letters*, 31(17):1445–1446, 1995.

[75] W.H. Loh, P.R. Morkel, and D.N. Payne. Wavelength selection and tuning by optical control in a two-segment erbium-doped fiber laser. *IEEE Photonics Technology Letters*, 6(1):43–46, 1994.

[76] W.H. Loh, A.B. Grundinin, and D.N. Payne. Optically controlled wavelength-adjustable passively modelocked erbium-doped fibre ring laser. *Electronics Letters*, 30(5):413–415, 1994.

[77] P.D. Humphrey and J.E. Bowers. Fiber-birefringence tuning technique for an erbium-doped fiber ring laser. *IEEE Photonics Technology Letters*, 5(1):32–34, 1993.

[78] Y.T. Chieng and R.A. Minasian. Tunable erbium-doped fiber laser with a reflection Mach-Zehnder interferometer. *IEEE Photonics Technology Letters*, 6(2):153–156, 1994.

[79] A. Gloag, N. Langford, K. McCallion, and W. Johnstone. Tunable erbium fiber laser using a novel overlay bandpass filter. *Optics Letters*, 19(11):801–803, 1994.

[80] N. Park, J.W. Dawson, and K.J. Vahala. Multiple wavelength operation of an erbium-doped fiber laser. *IEEE Photonics Technology Letters*, 4(6):540–541, 1992.

[81] A.J. Poustie and N. Finlayson. Multiwavelength fiber laser using a spatial mode beating filter. *Optics Letters*, 19(10):716–718, 1994.

[82] D.V. Eddolls, S.J. Vass, R.M. Ash, and C.A. Park. Two-segment multiquantum well lasers with 7nm tuning range and narrow linewidth. *Electronics Letters*, 28(11):1057–1058, 1992.

[83] C.K. Gardiner, R.G.S. Plumb, P.J. Williams, and T.J. Reid. Three-section sampled-grating DBR lasers: modelling and measurements. *IEE Proc.-Optoelectronics*, 143(1):24–30, 1996.

[84] V. Jayaraman, D.A. Cohen, and L.A. Coldren. Theory, design and performance of extended tuning range semiconductor lasers with sampled gratings. *IEEE J. Quantum Electronics*, 29(6):1824–1834, 1993.

[85] V. Jayaraman, M.E. Heimbuch, L.A. Coldren, and S.P DenBaars. Widely tunable continuous-wave InGaAsP/InP sampled grating lasers. *Electronics Letters*, 30(18):1492–1494, 1994.

[86] Y. Tohmori, F. Kano, H. Ishii, Y. Yoshikuni, and Y. Kondo. Wide tuning with narrow linewidth in DFB lasers with superstructure grating (SSG). *Electronics Letters*, 29(15):1350–1352, 1993.

[87] H. Ishii, F. Kano, Y. Tohmori, Y. Kondo, T. Tamamura, and Y. Yoshikuni. Broad range (34nm) quasi-continuous wavelength tuning in super-structure-grating DBR lasers. *Electronics Letters*, 30(14):1134–1135, 1994.

[88] M. Schilling, W. Idler, D. Baums, K. Dütting, G. Laube, K. Wünstel, and O. Hildebrand. 6 Thz range tunable 2.5 Gb/s frequency conversion by a multiquantum well Y laser. *IEEE J. Quantum Electronics*, 29(6):1835–1843, 1993.

[89] K. Sato, Y. Nakano, and K. Tada. Wavelength tuning characteristics of widely tunable distributed forward-coupling and backward-coupling semiconductor-laser. *IEEE Photonics Technology Letters*, 7(3):257–259, 1995.

[90] M.J. Holmes, F.P. Payne, P. Dainty, T.J. Hall, and W.A. Crossland. Low crosstalk devices for wavelength-routed networks. *IEE Digest No. 95-128*, IEE Colloquium on Guided Wave Optical Signal Processing:Savoy Place, London, 8th June 1995.

[91] S.T. Warr and R.J. Mears. Polarisation-insensitive operation of ferroelectric liquid-crystal devices. *Electronics Letters*, 31:714–716, 1995.

[92] M.A. Handschy, K.M. Johnson, G. Moddel, and L.A. Pagano-Stauffer. Electro-optic applications of ferroelectric liquid crystals to optical computing. *Ferroelectrics*, 85:279–289, 1988.

[93] U. Krackhardt and N. Streibl. Design of Damman gratings for array generation. *Optics Communications*, 74(1,2):31–35, 1989.

[94] M.P.Dames, R.J.Dowling, P.McKee, and D.Wood. Efficient optical elements to generate intensity weighted spot arrays: design and fabrication. *Applied Optics*, 30(19):2685–2691, 1991.

[95] D.C. O'Brien, W.A. Crossland, and R.J. Mears. A holographically routed optical crossbar: theory and simulation. *Optical Computing and Processing*, 1(3):233–243, 1991.

[96] H. Yamazaki and M. Yamaguchi. 4 × 4 free-space optical switching using real-time binary phase-only holograms generated by a liquid-crystal display. *Optics Letters*, 16(18):1415–1417, 1991.

[97] S.E. Broomfield, M.A.A. Neil, E.G.S. Paige, and G.G. Yang. Programmable binary phase-only optical device based on ferroelectric liquid crystal SLM. *Electronics Letters*, 28(1):26–28, 1992.

[98] D.C.O'Brien, T.D.Wilkinson, R.J.Mears, and W.A.Crossland. Generalised dynamic holographic interconnects using spatial light modulators. *IEEE Conference at Palm Springs - Topical meeting on SLM's*, SWC2-4:192–195, 1993.

[99] D.C.O'Brien. Dynamic holograms for optical interconnection. *PhD Dissertation*, 1993.

[100] E. Hecht and A. Zajac. Optics. *2nd Edition*, Adison-Wesley Publishing Company Ltd.:445–447, 1987.

[101] S.T. Warr, M.C. Parker, and R.J. Mears. Optically transparent digitally tunable wavelength filter. *Electronics Letters*, 31:129–130, 1995.

[102] M.C. Parker and R.J. Mears. Digitally tunable filter and laser. *Photonics Technology Letters*, 8(8):1007–1008, 1996.

[103] M.C. Parker, A.D. Cohen, and R.J.Mears. Active holographic spectral equalisation and channel management for WDM. *OFC'97*, Dallas, Texas, February 1997.

[104] F. Mok, J. Diep, H.K. Liu, and D. Psaltis. Real-time computer-generated hologram by means of liquid-crystal television spatial light modulator. *Optics Letters*, 11(11):748–750, 1986.

[105] M.F. Bone, D. Coates, W.A. Crossland, P. Gunn, and P.W. Ross. Ferroelectric liquid crystal display capable of video line address time. *Displays*, pages 115–118, July 1987.

[106] B. Bahadur. Liquid Crystals: Applications and Uses. *World Scientific*, Volume 1, 1990.

[107] D.C. O'Brien and R.J. Mears. Computer generated holograms optimised for illumination with partially coherent light using silicon backplane spatial light modulators as the recording device. *Proc. SPIE*, 1505:32–37, 1991.

[108] W.E Ross, D. Psaltis, and R.H. Anderson. Two-dimensional magneto-optic spatial light modulator for signal processing. *Optical Engineering*, 22(4):485–490, 1983.

[109] D.W. Prather and J.N. Mait. Acousto-optic generation of two-dimensional spot arrays. *Optics Letters*, 16(22):1720–1722, 1991.

[110] D.A. Gregory, R.D. Juday, J. Sampsell, R. Gale, R.W. Cohn, and S.E. Monroe. Optical characteristics of a deformable-mirror spatial light modulator. *Optics Letters*, 13(1):10–12, 1988.

[111] D. Williams, S.G. Latham, C.M.J. Powles, M.A. Powell, R.C. Chittick, A.P. Sparks, and N. Collings. An amorphous silicon/chiral smectic spatial light modulator. *J. Physics D: Applied Physics*, 21:156–159, 1988.

[112] M.O. Freeman, T.A. Brown, and D. M. Walba. Quantized complex ferroelectric liquid crystal spatial light modulators. *Applied Optics*, 31(20):3917–3929, 1992.

[113] M.A.A. Neil and E.G.S. Paige. Improved transmission in a two-level, phase-only, spatial light modulator. *Electronics Letters*, 30(5):445–446, 1994.

[114] J.E. Stockley, G.D. Sharp, S.A. Serati, and K.M. Johnson. Analog optical phase modulator based on chiral smectic and polymer cholesteric liquid crystals. *Optics Letters*, 20(23):2441–2443, 1995.

[115] G.D. Love. Liquid-crystal phase modulator for unpolarized light. *Applied Optics*, 32(13):2222–2223, 1993.

[116] M.Born and E.Wolf. Principles of Optics. *Pergamon Press*, pages 405–406, 1959.

[117] F.Wyrowski. Upper bound of the diffraction efficiency of diffractive phase elements. *Optics Letters*, 16(24):1915–1917, 1991.

[118] Li Song and R.Lessard. Diffraction efficiency of a thin amplitude-phase holographic grating: a convolution approach. *Journal of Modern Optics*, 37(8):1319–1328, 1990.

[119] T.D.Wilkinson, D.C.O'Brien, and R.J.Mears. Dynamic asymmetric binary holograms using a ferroelectric liquid crystal spatial light modulator. *Optics Communications*, 109(3-4), 1994.

[120] R.W. Hamming. Coding and Information Theory. *Prentice-Hall International*, pages 173–177, 1980.

[121] P.A. Cook. Nonlinear Dynamical Systems. *Prentice-Hall International*, pages 11–12, 1994.

[122] E. Kreyszig. Advanced Engineering Mathematics. *John Wiley & Sons*, pages 808–810, 1988.

[123] M.Born and E.Wolf. Principles of Optics. *Pergamon Press*, page 403, 1959.

[124] A.W. Snyder and J.D. Love. Optical Waveguide Theory. *Chapman and Hall*, pages 425–429, 1983.

[125] D. Marcuse. Loss analysis of single-mode fibre splices. *Bell Syst. Tech. Journal*, 56(5), 1977.

[126] C.A. Brackett, A.S. Acampora, J. Sweitzer, G. Tangonan, M.T. Smith, W. Lennon K.-C. Wang, and R.H. Hobbs. A scalable multiwavelength multihop optical network: A proposal for research on all-optical networks. *IEEE Journal of Lightwave Technology*, 11(5/6):736–753, 1993.

[127] The Newport Catalogue. *Diode Laser Objective Lenses*, page 2.93, 1994.

[128] J.R. Collington, M.P. Dames, W.A. Crossland, and R.W.A Scarr. Optically accessed electronic memory. *Proc. of 5th International Conference on FLCs*, 181(4):99–110, 1996.

[129] E. Snitzer. Optical maser action of Nd^{3+} in a barium crown glass. *Physics Review Letters*, 7(12):444–446, 1961.

[130] K.C. Kao and G.A Hockham. Dielectric-fibre surface waveguides for optical frequencies. *IEE Proc. Journal*, 133(7):1151–1158, 1966.

[131] R.J. Mears, L. Reekie, S.B. Poole, and D.N. Payne. Neodymium-doped silica single-mode fibre lasers. *Electronic Letters*, 21:738–740, 1985.

[132] Hewlett Packard. Technical Data for EFA2000 Series. 1995.

[133] T. Okoshi, K. Kikuchi, and A. Nakayama. Novel method for high resolution measurement of laser output spectrum. *Electronics Letters*, 16(16):630–631, 1980.

[134] H.J. White, G.M. Proudley, C. Stace, N.A. Brownjohn, R. Dawkins, A.C. Walker, M.R. Taghizadeh, C.P. Barrett, D.T. Neilson, W.A. Crossland, J.R. Brocklehurst, and M.J. Birch. The OCPM demonstrator system. *OSA Topical Meeting on 'Photonics in Switching'*, Salt Lake City:Paper PPd1, 1995.

[135] M.Born and E.Wolf. Principles of Optics. *Pergamon Press*, page 407, 1959.

[136] G.H.B. Thompson. Physics of Semiconductor Laser Devices. *John Wiley and Sons*, Appendix 4:535–537, 1980.

[137] P.A. Cook. Nonlinear Dynamical Systems. *Prentice-Hall International*, pages 196–199, 1994.

Appendix A

Appendix to Holographic Analysis

A.1   Justification of Basic Assumptions

The basic assumption underlying the mathematical analysis in §3.3 is that the quantity '$\cos\left(\frac{(2k+1)\pi W x_p}{f\lambda}\right)$' can be considered a random variable. If it is a random variable then it will have an associated probability density function (PDF). To simplify, we need only consider the expression $\cos(mX)$ which exhibits the same properties of the original quantity; namely the taking of the cosine of a constant X ($\equiv \frac{\pi W x_p}{f\lambda}$) being multiplied by an integer m ($\equiv 2k+1$) varying from 1 to N. The statistics of our random variable $\cos(mX)$ can also be found by analysing the function $\cos(x)$ for $x = 0$ to 2π. We assume that the system is *ergodic*, such that the statistical properties of an arbitrary sample function $\cos(nX)$ are the same, whether it is considered as

- a function over X-space (with X varying from 0 to 2π) and constant n (where $1 \leq n \leq N$)

- the nth sample function from an *ensemble* of N random variables $\{\cos(mX)\}$ for $m = 1$ to N, and with constant arbitrary X.

The PDF of an explicit function $y = f(x)$ is proportional to the inverse of its derivative:

$$PDF(y) \propto \frac{1}{\left|\frac{dy}{dx}\right|}$$

In our case, the explicit function is $y = \cos(x)$, so that $\frac{dy}{dx} = -\sin(x)$. Hence:

$$PDF(y) \propto \frac{1}{\sqrt{1-y^2}}$$

It can be seen that the curve is asymptotic at -1 and +1. We need to find the constant of proportionality α, so that the total area under the curve is equal to 1:

$$\int_{-1}^{1} \frac{\alpha}{\sqrt{1-y^2}} dy = 1$$

This yields the result that $\alpha = \frac{1}{\pi}$. Hence:

$$PDF(y) = \frac{1}{\pi\sqrt{1-y^2}} \tag{A.1}$$

This equation gives the curve shown in figure (A.1). One further useful quantity we need to have is the expected value of $\cos(x)$ given that $\cos(x) > 0$. Mathematically expressed, we need to calculate $E\{|\cos(x)|\}$. This is found to be $\frac{2}{\pi}$, by solving the following integral:

$$\int_0^1 \frac{1}{\pi\sqrt{1-y^2}} dy = \frac{2}{\pi} \tag{A.2}$$

The validity of our assumption that the system is ergodic can be tested 'experimentally' by finding the *frequency of occurrence* (equivalent to PDF) of values of $\cos(mX)$ for $X = 0.5$ (an arbitrary value in radians) and m increasing in integer steps from 1 to 10,000. Allowing m to increase up to 10,000 corresponds to a very large one-dimensional binary-phase hologram consisting of 10,000 pixels. This results in the frequency distribution (PDF) shown in figure (A.2). It can be seen to match closely with the theoretical PDF of equation (A.1) plotted in figure (A.1); both have a mean of zero, are symmetric about zero and have asymptotes at $+1$ and -1. As we allow m to increase towards infinity (implying ever larger holograms) then the frequency distribution will tend even closer towards the theoretical PDF. The 'experiment' is repeated for X varying from 0 to π radians and m varying from 1 to 10,000 to give the 3D 'valley landscape' result shown in figure (A.3), depicting the PDFs for all values of X. The figure demonstrates that all the PDFs for each value of X possesses the same generic 'U'-shape of figure (A.1), albeit with variations[1]. Hence to a good approximation we can assume that the statistics of the system remain the same for all values of X. The two main results which we will use in our analysis are as follows:

- $E\{\cos(mX)\} = 0$

- $E\{|\cos(mX)|\} = \frac{2}{\pi}$

These two results are essentially independent of m and X, and whether the 'sin' or 'cosine' function is used.

---

[1]Of interest is to note that for certain values of X, the resulting PDF is not smooth, but contains 'teeth'-like irregularities, whose repetition-frequency doubles every time the value of X is halved. Such behaviour is reminiscent of the bifurcating to be found in chaotic systems, such as the 'logistic equation'[137]. This may be an indication as to why the best hologram generation algorithms are often non-deterministic in nature.
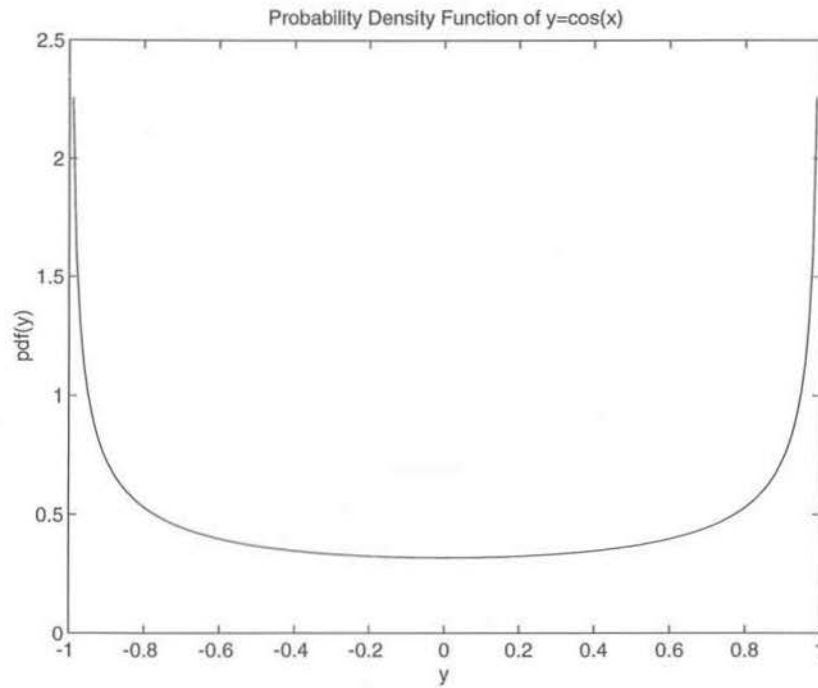
Figure A.1: PDF of the function $y = \cos(x)$
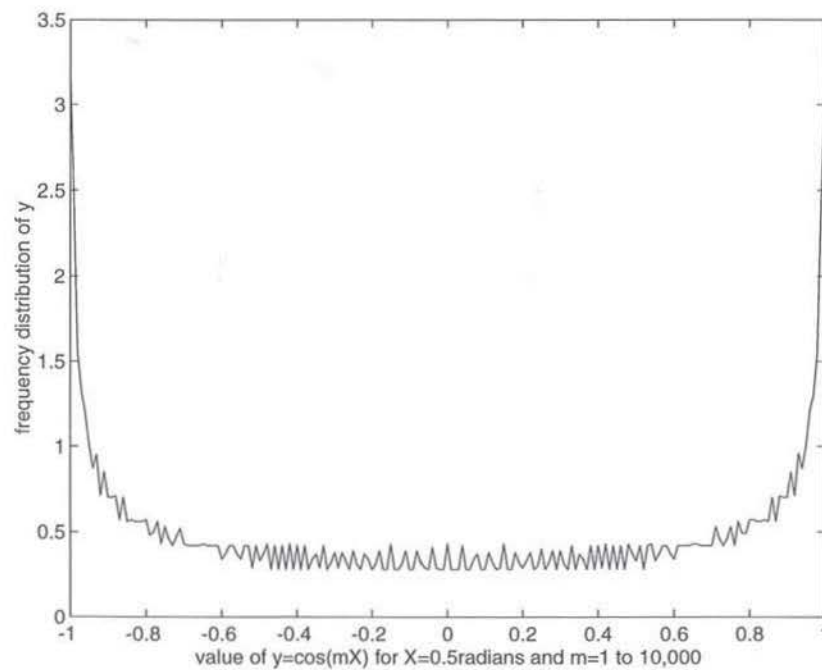
Figure A.2: Frequency distribution of $\cos(mX)$ for $X = 0.5$ and $m = 1 \to 10,000$
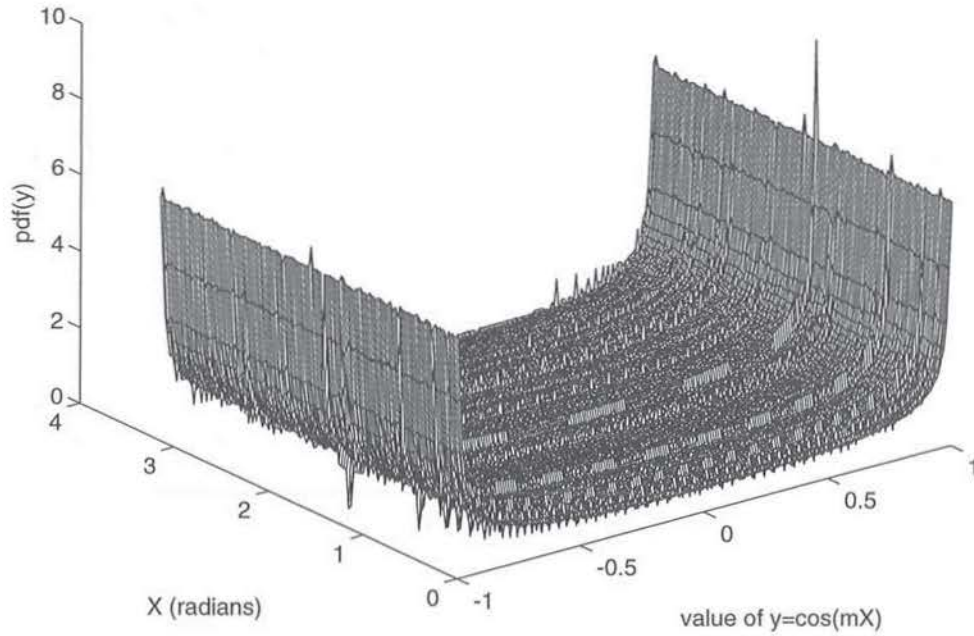
Figure A.3: PDFs over the range 0 to π radians

A.2   Geometric (Binomial) Series Results

The expression $(1 + \beta)^n$ can be expressed in a binomial series expansion as:

$$(1 + \beta)^n = \sum_{q=0}^{n} \frac{\beta^q n!}{q!(n-q)!}$$

hence for $\beta = 1$:

$$2^n = \sum_{q=0}^{n} \frac{n!}{q!(n-q)!}$$

The series is symmetrical about the central element. So for n = even number, we can write:

$$2^n = 2 \sum_{q=0}^{\frac{n}{2}-1} \frac{n!}{q!(n-q)!} + \frac{n!}{\frac{n}{2}!\frac{n}{2}!}$$

Hence by simple algebraic manipulation we get:

$$\sum_{q=0}^{\frac{n}{2}-1} \frac{n!}{q!(n-q)!} = \frac{1}{2}\left(2^n - \frac{n!}{\frac{n}{2}!\frac{n}{2}!}\right) \qquad (A.3)$$

Using the result of equation (A.3) we can find an expression for the series:

$$\sum_{q=0}^{\frac{n}{2}-1} \frac{(n-1)!}{(q-1)!(n-q)!}$$

115

We first need to make the substitutions: $p = n - 1$ and $l = q - 1$. Since n is an even number, then p must be odd and a binomial expansion of 2^p will contain $p + 1$ terms. Thus a summation from 0 to $\frac{p}{2} - \frac{1}{2}$ contains $(\frac{p}{2} + \frac{1}{2})$ terms (*i.e.* half the series.) Thus we can write:

$$\sum_{l=0}^{\frac{p}{2}-\frac{1}{2}} \frac{p!}{l!(p-l)!} = \frac{1}{2} \sum_{l=0}^{p} \frac{p!}{l!(p-l)!}$$

$$= \frac{1}{2} 2^p$$

Substituting $p = n - 1$ back into the expression gives us:

$$\sum_{q=0}^{\frac{n}{2}-1} \frac{(n-1)!}{(q-1)!(n-q)!} = \frac{2^n}{4} \tag{A.4}$$

A.3 Non-Symmetric Holograms

In this Appendix, we demonstrate that the results derived in the main body of the text for the case of an evenly symmetrical hologram are the same as for a hologram with odd symmetry; as well as for a hologram with no overall symmetry. We still assume that we can consider the expressions '$\cos\left(\frac{(2k+1)\pi W x_p}{f\lambda}\right)$' and additionally '$\sin\left(\frac{(2k+1)\pi W x_p}{f\lambda}\right)$' as random variables. We also assume that both random variables have an equal chance of being positive or negative such that:

$$prob\left\{\cos\left(\frac{(2k+1)\pi W x_p}{f\lambda}\right) > 0\right\} = 1/2$$

$$\text{and} \quad prob\left\{\sin\left(\frac{(2k+1)\pi W x_p}{f\lambda}\right) > 0\right\} = 1/2$$

These assumptions are underpinned with the justifications as given in Appendix A.1.

The expression for the amplitude of a single spot of light at x_p due to a general non-symmetric hologram is given from equation (3.1) by

$$h(x_p) = \sqrt{\frac{2\pi}{f\lambda}} W \sqrt{\frac{P_{in}2Z}{NW}} 2 \sum_{k=0}^{\frac{N}{2}-1} a_k \cos\left(\frac{(2k+1)\pi W x_p}{f\lambda}\right) + j b_k \sin\left(\frac{(2k+1)\pi W x_p}{f\lambda}\right)$$

We represent the amplitude expression $\sqrt{\frac{2\pi}{f\lambda}} W \sqrt{\frac{P_{in}2Z}{NW}} 2$ by the symbol A_0 in order to make the algebra clearer. We define the modulus of the expected amplitude of the spot of light as $A_p = |E\{h(x_p)\}|$, which gives us

$$A_p = |E\{h(x_p)\}|$$

$$= \left| E\left\{ A_0 \sum_{k=0}^{\frac{N}{2}-1} a_k \cos\left(\frac{(2k+1)\pi W x_p}{f\lambda}\right) + j b_k \sin\left(\frac{(2k+1)\pi W x_p}{f\lambda}\right) \right\} \right|$$

$$= A_0 \left| \sum_{k=0}^{\frac{N}{2}-1} E\left\{ a_k \cos\left(\frac{(2k+1)\pi W x_p}{f\lambda}\right) + jb_k \sin\left(\frac{(2k+1)\pi W x_p}{f\lambda}\right) \right\} \right|$$

$$= A_0 \sum_{k=0}^{\frac{N}{2}-1} \left| E\left\{ a_k \cos\left(\frac{(2k+1)\pi W x_p}{f\lambda}\right) + jb_k \sin\left(\frac{(2k+1)\pi W x_p}{f\lambda}\right) \right\} \right| \quad (A.5)$$

Since the expectation value within the summation is ultimately a constant independent of k and the summation (with respect to k) is a real function, we are justified in placing both the modulus function and the expectation function within the summation. We now wish to calculate the expected value of the kth component of the summation:

$$\left| E\left\{ a_k \cos\left(\frac{(2k+1)\pi W x_p}{f\lambda}\right) + jb_k \sin\left(\frac{(2k+1)\pi W x_p}{f\lambda}\right) \right\} \right|$$

We know that the set of coefficients $\{a_k, b_k\}$ are chosen so as to maximise the spot intensity, which gives us a starting point to calculate the maximum possible value of the above expression. We can choose our values of a_k and b_k for a particular k by comparing the two results from the functions:

$$(i) \quad \left| \cos\left(\frac{(2k+1)\pi W x_p}{f\lambda}\right) \right| \quad \text{and} \quad (ii) \quad \left| \sin\left(\frac{(2k+1)\pi W x_p}{f\lambda}\right) \right|$$

If the first result is larger than the second result, we let $a_k = \pm 1$ (depending on the sign of the first result) and $b_k = 0$. If $\cos\left(\frac{(2k+1)\pi W x_p}{f\lambda}\right)$ is positive then we put $a_k = +1$, but if it is negative then $a_k = -1$. Conversely, if the second result is greater than the first, then we let $b_k = \pm 1$ (depending similarly on the sign of that second result) and $a_k = 0$. In this way, we are always causing the summation components at the spot position x_p to add up by as much as possible. The coefficients a_k and b_k are orthogonal to each other, such that:

- If $a_k = \pm 1$ then $b_k = 0$

- If $b_k = \pm 1$ then $a_k = 0$

We can calculate analytically the expected value from such an algorithm by substituting the variable $\mathcal{X} = \frac{(2k+1)\pi W x_p}{f\lambda}$ and finding $E\{\max(|\cos(\mathcal{X})|, j|\sin(\mathcal{X})|)\}^2$ for $-\pi < \mathcal{X} \leq \pi$. Figure (A.4) illustrates that by considering $\mathcal{X}$ between the limits of $-\frac{\pi}{4}$ and $+\frac{\pi}{4}$, the average value of $|\cos(\mathcal{X})|$ for the case when $|\cos(\mathcal{X})| > |\sin(\mathcal{X})|$ lies between $\frac{1}{\sqrt{2}}$ and 1. The actual expected value of $|\cos(\mathcal{X})|$ for this case is given by:

$$
E\{|\cos(\mathcal{X})| > |\sin(\mathcal{X})|\} = \frac{\int_{-\frac{\pi}{4}}^{\frac{\pi}{4}} \cos(x)dx}{\frac{\pi}{2}} \quad (A.6)
$$

$$
= \frac{2}{\pi}[sin(x)]_{-\frac{\pi}{4}}^{\frac{\pi}{4}}
$$

$$
= \frac{2\sqrt{2}}{\pi}
$$

---

[2]The function $\max(x,y)$ is defined to evaluate the magnitudes of the two arguments x and y, and then to return the value of whichever of the two is the greatest.
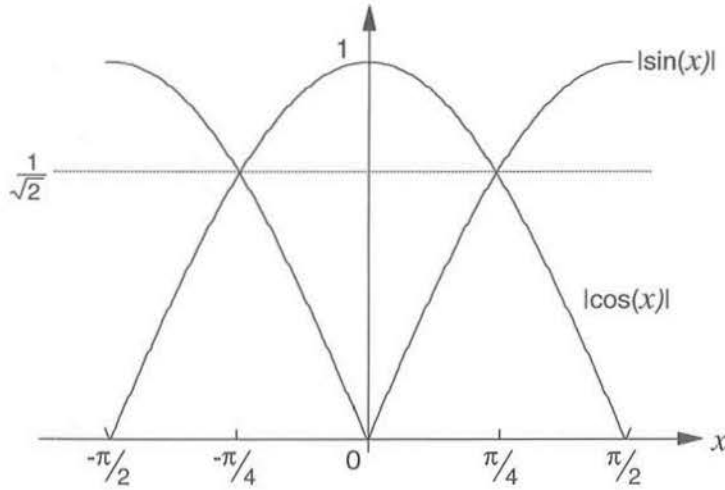
Figure A.4: Plots of $|\cos(\mathcal{X})|$ and $|\sin(\mathcal{X})|$ for $-\frac{\pi}{2} < \mathcal{X} \leq \frac{\pi}{2}$

This result is the same for the converse case $E\{|\sin(\mathcal{X})| > |\cos(\mathcal{X})|\}$, *i.e.* the average value of $|\sin(\mathcal{X})|$ for the case when $|\sin(\mathcal{X})| > |\cos(\mathcal{X})|$. By considering figure (A.4) it is apparent that for half the time $|\cos(\mathcal{X})| > |\sin(\mathcal{X})|$ and for the other half the opposite is true. Thus overall, the expectation is:

$$E\{\max(|\cos(\mathcal{X})|, j|\sin(X)|)\} = \frac{1}{2} \cdot \frac{2\sqrt{2}}{\pi} + j\frac{1}{2} \cdot \frac{2\sqrt{2}}{\pi}$$
$$\Rightarrow |E\{|\max(\cos(\mathcal{X})|, j|\sin(\mathcal{X})|)\}| = \frac{2}{\pi}$$

Thus we know that the absolute value of the expectation for a non-symmetrical hologram is:

$$\left| E \left\{ \max \left(\left| \cos \left(\frac{(2k+1)\pi W x_p}{f\lambda} \right) \right|, j \left| \sin \left(\frac{(2k+1)\pi W x_p}{f\lambda} \right) \right| \right) \right\} \right| = \frac{2}{\pi}$$
$$\Rightarrow \left| E \left\{ a_k \cos \left(\frac{(2k+1)\pi W x_p}{f\lambda} \right) + j b_k \sin \left(\frac{(2k+1)\pi W x_p}{f\lambda} \right) \right\} \right| = \frac{2}{\pi}$$

If the hologram has an odd symmetry then we need only consider $E\{|j\sin(\mathcal{X})|\}$ and ignore the possibility of using $\cos(\mathcal{X})$ to 'increase' our average. We find that the expectation for such a hologram is:

$$E\{|\sin(\mathcal{X})|\} = \frac{\int_0^\pi \sin(x)dx}{\pi}$$
$$= \frac{1}{\pi}[-\cos(x)]_0^\pi$$
$$= \frac{2}{\pi}$$
$$\Rightarrow \left| E \left\{ j b_k \sin \left(\frac{(2k+1)\pi W x_p}{f\lambda} \right) \right\} \right| = \frac{2}{\pi}$$

The expectations for the non-symmetrical and odd-symmetrical cases are the same as for the case of a hologram with even-symmetry, as calculated in equation (3.4a). This tells us that large symmetric or anti-symmetric holograms should have the same performance as holograms which do not have any such symmetry, such as those holograms produced by simulated annealing. Obviously, for smaller sized holograms there is a greater scope for optimisation, since the statistics of the 'random variables' will show greater fluctuations. But as the size of the hologram grows, then these statistical fluctuations are damped down, and we should find that non-symmetric holograms converge to produce the same performance as symmetric holograms.

A.4 Sterling Approximation for $F(p)$

The function $F(p)$ is given by:

$$F(p) = \frac{p!}{2^p \frac{p}{2}! \frac{p}{2}!} \tag{A.7}$$

and is already a small neat expression, but we can simplify it further by use of the Sterling Approximation:

$$p! \approx p^p e^{-p} \sqrt{2\pi p} \tag{A.8}$$

Substituting equation (A.8) into equation (A.7) we get:

$$
\begin{aligned}
F(p) &\approx \frac{1}{2^p} \frac{p^p e^{-p} \sqrt{2\pi p}}{\left\{ \left(\frac{p}{2}\right)^{\frac{p}{2}} e^{-\frac{p}{2}} \sqrt{\pi p} \right\}^2} \\
&\approx \frac{1}{2^p} \frac{p^p e^{-p} \sqrt{2\pi p}}{p^p \left(\frac{1}{2}\right)^p e^{-p} \pi p} \\
&\approx \sqrt{\frac{2}{\pi p}}
\end{aligned} \tag{A.9}
$$

This expression for $F(p)$ is derived using the Sterling Approximation which becomes increasingly accurate for high p, but is still surprisingly accurate for low values of p. Figure (A.5) plots the exact solution to $\frac{p!}{2^p \frac{p}{2}! \frac{p}{2}!}$ against the derived approximation $\sqrt{\frac{2}{\pi p}}$, as p varies from 1 to 20. We see that for $p = 1$ the exact solution is 1, whereas the approximation gives 0.80, but that as p increases the two curves rapidly converge.
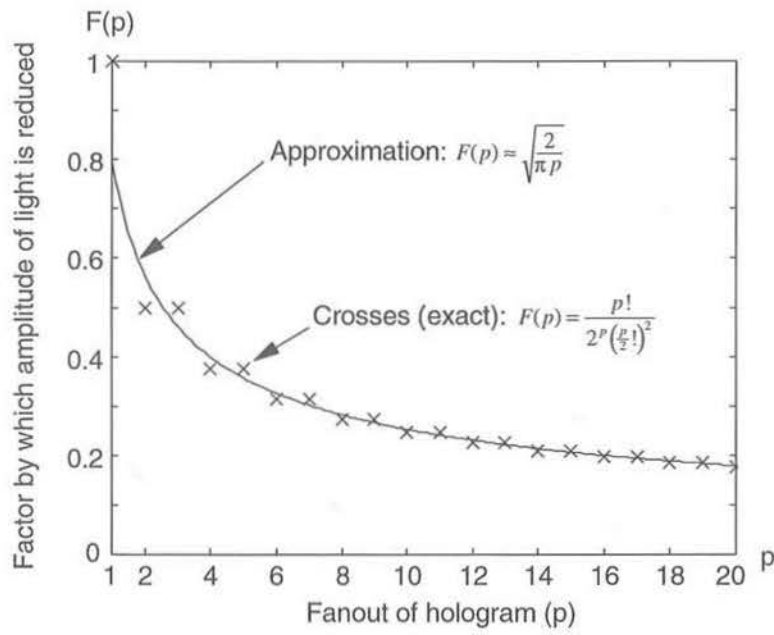
Figure A.5: Plot of $F(p)$ against its approximation

Appendix B

Associated Publications

B.1 Journals

Optically transparent digitally tunable wavelength filter, S.T.Warr, M.C.Parker, R.J.Mears, *Electronics Letters*, Vol.31, No.2, p129-130, January 1995

Digitally tunable wavelength filter and laser, M.C.Parker, R.J.Mears, *IEEE Photonics Technology Letters*, Vol.8, No.8, p1007-1008, August 1996

Telecommunications applications of FLC smart pixels (invited), R.J.Mears, W.A.Crossland, M.P.Dames, J.Collington, M.C.Parker, S.T.Warr, T.D.Wilkinson, A.B.Davey, *IEEE Journal Selected Topics in Quantum Electronics*, to be published.

B.2 Conferences

Tunable holographic wavelength filter, M.C.Parker, S.T.Warr, R.J.Mears, W.A.Crossland, *OSA Spring Topical Meeting, Salt Lake City*, March 1995

Polarisation insensitive ferroelectric liquid crystal devices, R.J.Mears, S.T.Warr, M.C.Parker, W.A.Crossland, A.B.Davey, *FLC '95, Cambridge*, July 1995

Digitally tunable erbium-doped fibre laser, M.C.Parker, R.J.Mears, *FLC '95, Cambridge*, July 1995

Digital holographic tuning mechanism for WDM, M.C.Parker, R.J.Mears, *IEE Colloquium on 'Optical and hybrid access networks', Ipswich*, March 1996

Novel digital tuning mechanism for lasers, M.C.Parker, R.J.Mears,
CLEO/QELS, Anaheim, California, June 1996

Digitally tunable WDM source, M.C.Parker, R.J.Mears,
OSA Summer Topical Meeting, Keystone, Colorado, August 1996

Active Holographic Spectral Equalisation and Channel Management for WDM,
M.C.Parker, A.D.Cohen, R.J.Mears,
OFC'97, Dallas, Texas, February 1997

Digitally Tunable Wavelength Filter and Laser

M. C. Parker, *Student Member, IEEE*, and R. J. Mears

Abstract— A novel nonmechanical, digitally tunable, polarization insensitive and optically transparent wavelength filter using holograms electro-optically written on a ferroelectric liquid crystal (FLC) spatial light modulator (SLM) has been constructed and operated to tune to discrete wavelengths spaced by 1.3 nm. The filter has been incorporated in a ring laser which is tunable over a range of 38.5 nm across the erbium window, giving output powers of 10 mW. Both wavelength filter and tunable laser are suitable for wavelength division multiplexing (WDM) applications.

I. INTRODUCTION

THE high bandwidth offered by optical fibers used in communications networks is currently most easily accessed using wavelength division multiplexing (WDM) schemes. Such schemes may require tunable components such as sources, filters and receivers, which can be tuned precisely and reliably for particular wavelengths within a tight tolerance [1]. Tunable fiber ring lasers have already been demonstrated using a variety of tuning mechanisms [2]. We have previously demonstrated a polarization sensitive tunable filter [3] and more recently polarization insensitive operation of a ferroelectric liquid crystal (FLC) spatial light modulator (SLM) [4]. In this letter, we describe a novel digitally tunable wavelength filter and fiber ring laser. The tuning mechanism comprises a free-space high spatial frequency fixed grating in conjunction with a polarization-insensitive relatively low spatial frequency FLC SLM. The digital, nonmechanical architecture of the laser potentially offers the stability, reliability and repeatability which is necessary for telecommunications system usage.

II. WAVELENGTH FILTER DESIGN

The construction of the filter and laser is shown in Fig. 1. Light from an input single-moded communications fiber ($\phi_c \approx 9~\mu$m) aligned along the optical axis is collimated by a doublet lens optimized for use in the near-infrared and of focal length $f = 96.1$ mm. The beam is passed through the SLM and diffracted by the displayed binary phase hologram, which is effectively a 1-D grating. The diffracted orders are then further diffracted and angularly dispersed by a fixed binary phase grating, which has been optimized to give a π phase change at a wavelength of 1550 nm. The light then passes through a similar doublet lens which spatially separates the angularly-separated diffracted orders. The second lens is also placed at an angle of 5° to the optical axis, so as to optimize
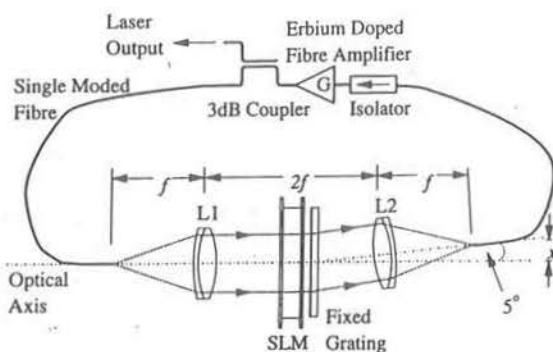
Fig. 1. Digitally tunable filter and fiber laser.

the coupling efficiency of the output fiber placed a distance $x = 8.5$ mm from the optical axis in the focal plane of the second lens, which collects light from only one diffracted order. Thus for a particular hologram displayed on the SLM, only one wavelength will be coupled back into the second fiber. Tuning of the filter is performed by simply changing the spatial frequency of the hologram displayed on the SLM. By placing the filter and an erbium-doped fiber amplifier in a uni-directional fiber ring resonator a digitally tunable fiber ring laser is made. A 3-dB coupler placed after the filter is used as the laser output.

The SLM is a transmissive multiplexed glass cell with 128 × 128 pixels on a 165-μm pitch that has been optimized to act as a half wave plate around the $\lambda_o = 1.55$-μm erbium window and can be reconfigured in under 5 ms. The fixed transmission grating was made with a spatial period of 18 μm and was fabricated by spinning a layer of photoresist on a glass flat to a depth of $\lambda_o/2(n_1 - n_0) \approx 1295$ nm, (n_0 is refractive index of air, n_1 is that of the photoresist ≈ 1.6) and using photolithography to selectively etch a binary phase grating.

The holograms are digital binary phase pixellated images which are generated using an iterative algorithm such as simulated annealing [5]. Holograms may be designed to optimally direct light of a fixed wavelength to a single spot anywhere in the 1st order, or to fanout the light to multiple spots. This idea can be extended so that the hologram can optimally direct a single desired wavelength or multiple wavelengths of light to a fixed point in the output plane. The equation governing the wavelength to be coupled back for the filter in Fig. 1 is given approximately by:

$$\lambda \approx \frac{x}{f\left(\dfrac{n}{ND} + \dfrac{1}{d}\right)} \tag{1}$$

where λ is the wavelength, $x = 8.5$ mm is the distance of the output fiber from the optical axis, $f = 96.1$ mm is the focal length, $N = 128$ is the number of pixels in the SLM, $D =$
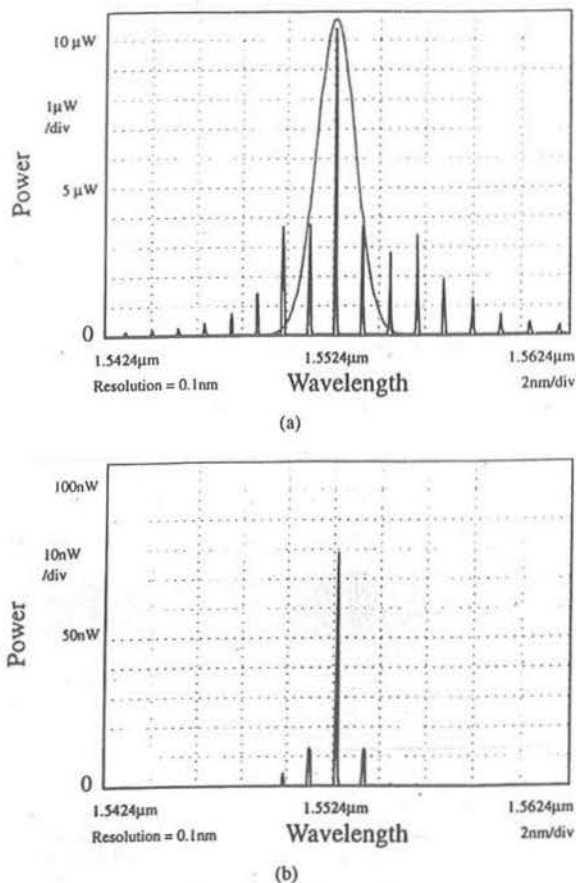
(a)

(b)

Fig. 2. (a) Spectrum of Fabry–Perot laser diode. — Measured spectrum, - - - Wavelength filter envelope. (b) Digitally filtered spectrum.

165 μm is the SLM pixel pitch, $d = 18$ μm is the period of the fixed diffraction grating. The factor n/ND represents the equivalent spatial frequency of the displayed hologram, where n is an integer between 0 and 64.

III. PASSIVE FILTER CHARACTERIZATION

The wavelength filter was characterized using a Fabry–Perot laser diode source with multiple lasing modes, shown in Fig. 2(a), spaced 1.2 nm apart. The filter was successful in isolating the individual modes, albeit with cross-talk from neighboring modes. An arbitrary filter result is shown in Fig. 2(b). The FWHM of the filter was found to be 2 nm, which is almost diffraction limited, and the filter could be tuned in steps of 1.3 nm over a theoretical range of 82 nm. Finer resolution and a smaller FWHM could be achieved by increasing f or the fixed grating resolution, subject to the available SLM clear aperture.

IV. LASER RESULTS

Lasing was achieved over the range 1528.6–1567.1 nm in discrete steps with an average spacing of 1.3 nm. The measurements were recorded using an optical spectrum analyzer and Fig. 3 shows an arbitrary group of eleven successively tuned lasing modes. The output was attenuated by 23 dB to avoid possible damage to the spectrum analyzer. The output power could also be accessed by placing a fiber in the zero order
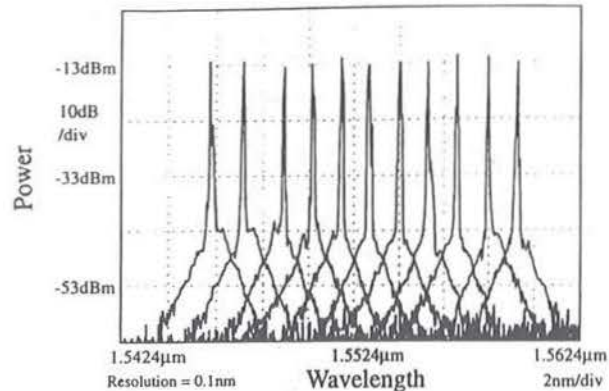

Fig. 3. Selection of lasing wavelengths from fiber laser.

of the SLM and collecting the undiffracted light. This would obviate the need for an additional coupler in the fiber loop. The long term wavelength stability of the laser was of the order of 0.1 nm, due to mechanical drift in the alignment of optical components. Greater compactness and fewer optical elements in the filter architecture will make the system mechanically more reliable and stable. This can be achieved using a folded architecture employing a silicon backplane reflective SLM, similar to the architecture proposed in [4]. The physical dimensions may also be reduced by using GRIN lenses with their shorter focal lengths instead of bulk lenses. Smaller pixel sizes (e.g., 30 μm) on the SLM and a higher fixed grating spatial frequency will also reduce the physical dimensions of the filter, while maintaining its resolution.

V. CONCLUSION

In this letter, we have described a new type of holographically tunable wavelength filter and fiber laser that is digital and nonmechanical in its operation. Such a laser and wavelength filter with its large tuning range and channel spacing of 1.3 nm has important applications in WDM schemes where precisely defined lasing frequencies, reliability, compactness, stability and tunability are required.

ACKNOWLEDGMENT

REFERENCES

[1] C. A. Brackett, A. S. Acampora, J. Sweitzer, G. Tangonan, M. T. Smith, W. Lennon, K.-C. Wang, and R. H. Hobbs, "A scalable multiwavelength multihop optical network: a proposal for research on all-optical networks," J. Lightwave Technol., vol. 11, pp. 736–753, 1993.

[2] M. J. F. Digonnet, Rare Earth Doped Fiber Lasers and Amplifiers. New York: Marcel Dekker, 1993.

[3] S. T. Warr, M. C. Parker, and R. J. Mears, "Optically transparent digitally tunable wavelength filter," Electron. Lett., vol. 31, pp. 129–130, 1995.

[4] S. T. Warr and R. J. Mears, "Polarization-insensitive operation of ferroelectric liquid-crystal devices," Electron. Lett., vol. 31, pp. 714–716, 1995.

[5] S. E. Broomfield, M. A. A. Neil, E. G. S. Paige, and G. G. Yang, "Programmable binary phase-only optical-device based on ferroelectric liquid-crystal SLM," Electron. Lett., vol. 28, no. 1, pp. 26–28, 1992.

namic Holographic Spectral Equalisation
WDM

C. Parker, A.D. Cohen and R.J. Mears.
artment of Engineering, Cambridge University,
mpington Street.
abridge CB1 2PZ, United Kingdom.

tract: We report a new technique for active man-
ment of WDM channels in an optically amplified
ecommunications system, based on a polarisation-
ensitive holographic in-line wavelength filter. Re-
ts are presented for the control, amplification and
alisation of five WDM channels spaced by 4nm.
ut signal power variations of 8.5dB and 2.0dB are
luced to 0.4dB and 0.3dB respectively, with sig-
s experiencing gains of up to 3.3dB while under-
ng equalisation. An unused channel and ampli-
l spontaneous emission noise from the EDFA have
o been suppressed by greater than 18dB. This is
first demonstration of active holographic spectral
alisation for WDM.

I. INTRODUCTION

e EDFA [1] is now well established for telecommunica-
ns. In order to maintain an acceptable spectral band-
lth when many amplifiers are concatenated, the need for
ssive spectral equalisation has long been recognised [2] [3]
However as WDM systems begin to be deployed the need
active management of the spectral gain is increasingly im-
rtant, since individual channel powers may vary over time
l the gain spectrum also varies with dynamic input load .
le such active technique employing acousto-optic tunable
ers (AOTF) was recently reported [5]. The underlying
hnology often requires additional complexity to attain po-
isation insensitivity, however. In this letter we present a
w technique for active management of the gain, based on
olarisation-insensitive, low drive-power, diffractive ferro-
ctric liquid crystal (FLC) in-line filter. The technique is
leable to tens of channels and is potentially low-cost in
lume production.

II. EXPERIMENT

le experimental configuration, employing standard single-
ded telecommunications fibre throughout, is shown in
g.1 . It is designed to provide spectral equalisation and sys-
m management over 5 channels spaced by approximately
m as shown in Fig.2 . In a real WDM system, input chan-
l powers will vary owing to:

- non-uniform gain profiles of the optical amplifiers (e.g.
  6.1dB for the EDFA shown in Fig.2)

- wavelength dependence of passive optical components

- potential variation in injection levels and signal path
  losses (e.g. spanning drop and insert nodes in a wave-
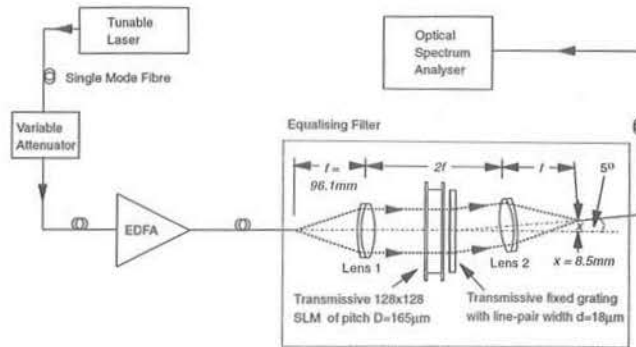 length routed network.)

Figure 1: Experimental configuration

The input channel variation is simulated here by a variable
output power tunable diode laser. It would be desirable to in-
put all signal channels simultaneously, but this was not pos-
sible with the equipment available. Low signal powers were
used in order to obtain the maximum differential gain avail-
able from the EDFA, hence overcoming the present high loss
of the filter and producing a net gain. The spectral equaliser
consists of a reconfigurable holographic filter [6] and EDFA
to provide gain and compensate for the filter losses. The
holographic filter comprises a FLC pixellated spatial light
modulator (SLM) displaying dynamic holograms, in conjunc-
tion with a fixed binary-phase high spatial frequency grating,
both within a $4f$ free-space lensing system (see Fig.1). The
filter passband for each channel had a theoretical FWHM
of 1.8nm. This can be reduced as desired by changing the
filter parameters, in particular by lowering the fixed grat-
ing pitch. Holograms were designed to compensate both for
the input channel power variation and the spectral depen-
dence of the EDFA gain, so that uniform output channel
powers were achieved. We also demonstrate the potential
for "knocking out" a central channel at 1556.1nm, which is
desirable for noise suppression should that channel be tem-
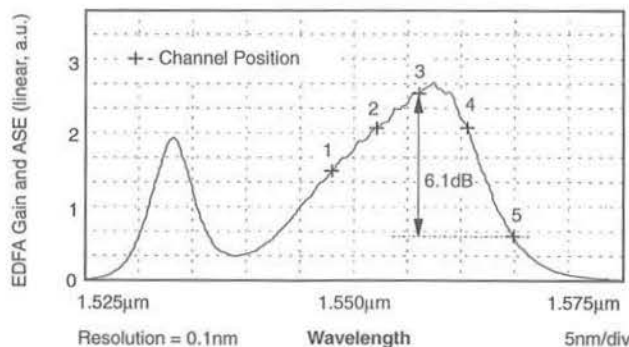porarily unused. The active reconfigurable nature of the

Figure 2: Gain and ASE profile of EDFA

equaliser was demonstrated by using two different sets of input signals. This was achieved by varying both the input power and wavelength of the signal on channel #4, to simulate the signal on that channel coming from a different source in the network. Two different holograms were designed to compensate for these changes, and to equalise the signal on channel #4 to the same level as the other three signals. An optical spectrum analyser was used to record the results.

In a practical device, the holograms required to compensate a set of input conditions, such as individual channel variations and change of use of channels (for network management and restoration), would be pre-calculated. The download time here is 5ms, but with an improved interface it is reasonable to expect reconfiguration in $20\mu s$ [7].

III. HOLOGRAPHIC FILTER DESIGN

The equation relating the filter wavelength associated with a hologram spatial period is given approximately by:

$$\lambda \approx \frac{x}{f\left(\frac{n}{ND} + \frac{1}{d}\right)} \quad (1)$$

where λ is the filter wavelength, $x = 8.5$mm is the distance of the output fibre from the optical axis, $f = 96.1$mm is the focal length, $N = 128$ is the number of pixels in the SLM, $D = 165\mu m$ is the SLM pixel pitch, $d = 18\mu m$ is the period of the fixed grating. The value n is an integer between 0 and 64. The factor n/ND represents one of the spatial frequencies of the displayed hologram which dictate the wavelengths to be filtered. In contrast to earlier work, in which only a single wavelength was filtered (requiring a single value of n for the subsequent hologram design), we have solved the above equation for 5 separate wavelengths, yielding 5 values of n to be fed into a computer-based design process to produce a hologram of mixed spatial frequency. The iterative hologram generation algorithm makes use of simulated annealing, which has been adapted to control the filter transmission spectrum amplitude at multiple wavelengths. This has involved the use of a modified error function that now includes a term comparing the actual transmission amplitude ratios of the filter with the desired ratios at the design wavelengths. (The filter transmission spectrum is directly related to the fourier transform of the hologram.) Initial design amplitudes for the filter transmission spectrum were determined by inverting the ratios of the EDFA amplified spontaneous emission (ASE) levels at the channel wavelengths (see Fig.2.) These design parameters yielded holograms with less than ideal channel equalisation due to system nonuniformities. The resulting systematic errors observed in the output spectrum were measured and corrected design parameters fed back to the algorithm. From many thousands of generated holograms, the best one was selected on the basis of minimum fractional error between desired and actual filter transmission amplitude ratios. Hologram design would be significantly improved by an in-situ feedback loop.
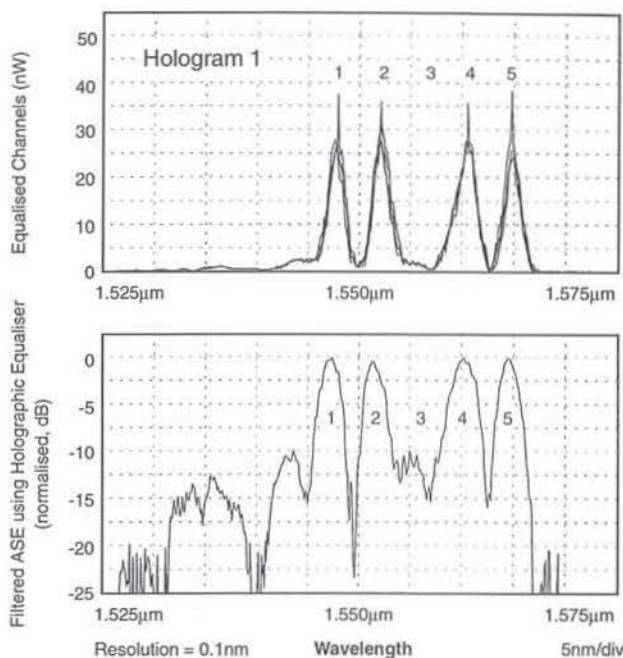
IV. RESULTS

Figure 3: Dynamic channel equalisation (hologram 1)

Figures 3 and 4 show the equalised spectra due to the two sets of different input signals, each requiring a different hologram. For the first case (see Fig.3), the unequalised input signals had a 2.0dB range of powers, which was reduced to less than 0.3dB, with individual signal gains of up to 3.3dB. For the second experiment (see Fig.4), the input signal powers had a range of 8.5dB which was reduced to 0.4dB after equalisation, with gains of up to 2.6dB. Tables 1 and 2 show the input and output powers and gains for the 5 channels, using the 2 holograms respectively to dynamically equalise the 4 signals. The ASE coming through the unused channel #3 was suppressed by greater than 18dB in both cases. The large EDFA ASE present around the wavelength $1.533\mu m$ has also been successfully suppressed by at least 18dB. Noise suppression is measured relative to the transmission of channel #5, which experiences the least gain (see Fig.2). Each channel passband is close to gaussian in shape, with a FWHM of 2nm, which closely approaches the diffraction-limited theoretical value expected from our filter design.

V. CONCLUSIONS

In this letter we have described a new technique for the active management of WDM channels. We have demonstrated the control of 5 channels: amplifying and equalising the powers of 4 input signals, while knocking out the ASE from an unused channel and other unused spectral areas to reduce noise. This technique gives us the ability to provide channel management for power variation due to EDFAs and different source powers in an all-optical network. The dynamic
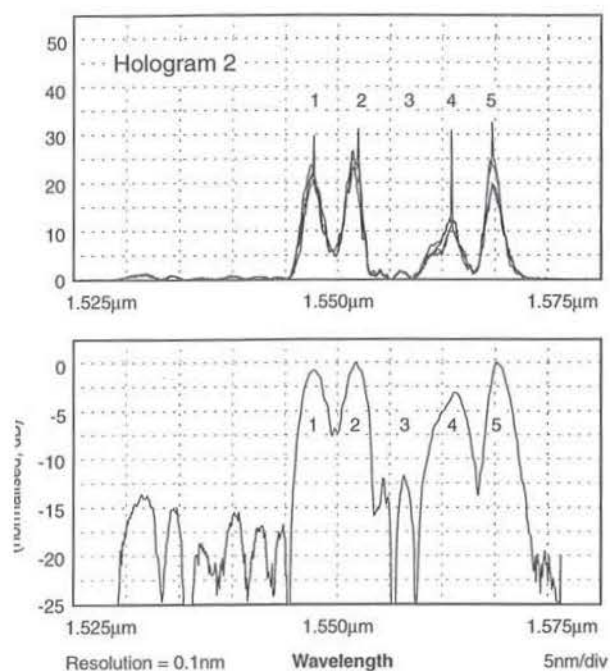
TABLE 1

Channel	λ (nm)	i/p Power (dBm)	o/p Power (dBm)	Gain (dB)
1	1547.6	-45.6	-44.4	1.2
2	1551.8	-46.3	-44.5	1.8
3	1556.1	no signal	n/a	n/a
4	1560.4	-46.3	-44.6	1.7
5	1564.4	-47.6	-44.3	3.3

TABLE 2

Channel	λ (nm)	i/p Power (dBm)	o/p Power (dBm)	Gain (dB)
1	1547.6	-45.6	-45.4	0.2
2	1551.8	-46.3	-45.1	1.2
3	1556.1	no signal	n/a	n/a
4	1560.8	-39.1	-45.3	-6.2
5	1564.4	-47.6	-45.0	2.6

Resolution = 0.1nm   **Wavelength**   5nm/div

Figure 4: Dynamic channel equalisation (hologram 2)

re of the holographic equaliser is compatible with all-*cal* networks potentially comprising multiple cascaded *FA* and holographic equaliser combinations. The present *t* of the holographic equaliser can be substantially in-*sed* by optimisation of the optical components, such as of a high tilt-angle continuous-phase FLC and a blazed *ing* in place of the fixed binary-phase grating. The opti-*design* of the holographic filter can also be simply modi-*to* reflect the latest ITU standard 0.8nm WDM channel *cing*. This new technique is polarisation-insensitive and *entially* high gain, making it suitable for WDM telecom-*nications* application.

erences:

R.J. Mears, L. Reekie, I.M. Jauncey, and D.N. Payne. Low-noise erbium-doped fibre amplifier at 1.54µm. *Electronics Letters*, 23(19):1026–1028, 1987.

M. Tachibana, R.I. Laming, P.R. Morkel, and D.N. Payne. Erbium-doped fiber amplifier with flattened gain spectrum. *Photonics Technology Letters*, 3(2):118–120, 1991.

K. Inoue, T. Kominato, and H. Toba. Tunable gain equalization using a Mach-Zehnder optical filter in multistage fiber amplifiers. *Photonics Technology Letters*, 3:718–720, 1991.

R. Kashyap, R. Wyatt, and R.J. Campbell. Wideband gain flattened erbium fibre amplifier using a photosensi-tive fibre blazed grating. *Electronics Letters*, 29(2):154–156, 1993.

[5] S.H. Huang, X.Y. Zou, S.-M. Hwang, A.E. Willner, Z. Bao, and D.A. Smith. Experimental demonstration of dynamic network equalization of three 2.5-Gb/s WDM channels over 1000km using acoustooptic tunable filters. *Photonics Technology Letters*, 8(9):1243–1245, 1996.

[6] M.C. Parker and R.J. Mears. Digitally tunable wave-length filter and laser. *Photonics Technology Letters*, 8(8):1007–1008, 1996.

[7] H.J. White, G.M. Proudley, C. Stace, N.A. Brownjohn, R. Dawkins, A.C. Walker, M.R. Taghizadeh, C.P. Bar-rett, D.T. Neilson, W.A. Crossland, J.R. Brocklehurst, and M.J. Birch. The OCPM demonstrator system. *OSA Topical Meeting on 'Photonics in Switching'*, Salt Lake City:Paper PPd1, 1995.

GLOSSARY

a.c.	Alternating Current
AOTF	Acousto-Optic Tunable Filter
AOM	Acousto-Optic Modulator
AOSLM	Acousto-Optic Spatial Light Modulator
ARROW	Antiresonant Reflecting Optical Waveguide
ASE	Amplified Spontaneous Emission
CD	Compact Disc
CGH	Computer Generated Hologram
CW	Continuous Wave
DBR	Distributed Bragg Reflector
DBS	Direct Binary Search
DFB	Distributed Feedback
EASLM	Electrically Addressed Spatial Light Modulator
EDFA	Erbium Doped Fibre Amplifier
EDFL	Erbium Doped Fibre Laser
EM	Electro-Magnetic
Er	Erbium
FC/PC	Flat-Cleaved/Physical-Contact
FFP	Fibre Fabry-Perot
FLC	Ferroelectric Liquid Crystal
FWHM	Full-Width at Half-Maximum
GRIN	Graded Index
HF	Hydrogen Fluoride
ITU	International Telecommunications Union
LC	Liquid Crystal
MOSLM	Magneto-Optic Spatial Light Modulator
NA	Numerical Aperture
OASLM	Optically Addressed Spatial Light Modulator
OEIC	Optoelectronic Integrated Circuit
OTDM	Optical Time Domain Multiplexing
PC	Personal Computer
PCLC	Polymer Cholesteric Liquid Crystal
PDF	Probability Density Function
RF	Radio Frequency
SAW	Surface Acoustic Wave
SLM	Spatial Light Modulator
SM	Single Mode
SNR	Signal-to-Noise Ratio
SSG	Superstructure Grating
TAT	Transatlantic Telecommunications
TV	Television
VLSI	Very Large Scale Integration
WDM	Wavelength Division Multiplexing